

NeuralCrop: Combining physics and machine learning for improved crop yield predictions

Yunan Lin^{1,2*}, Sebastian Bathiany^{1,2}, Maha Badri^{1,2},
Maximilian Gelbrecht^{1,2}, Philipp Hess^{1,2}, Brian Groenke²,
Jens Heinke², Christoph Müller², Niklas Boers^{1,2,3*}

¹Munich Climate Center and Earth System Modelling Group,
Department of Aerospace and Geodesy, School of Engineering and
Design, Technical University of Munich, Munich, Germany.

²Potsdam Institute for Climate Impact Research, Potsdam, Germany.

³University of Exeter, Exeter, UK.

*Corresponding author(s). E-mail(s): yunan.lin@tum.de;
n.boers@tum.de;

Abstract

Global gridded crop models (GGCMs) simulate daily crop growth by explicitly representing key biophysical processes and project end-of-season yield time series. They are a primary tool to quantify the impacts of climate change on agricultural productivity and assess associated risks for food security. Despite decades of development, state-of-the-art GGCMs still have substantial uncertainties in simulating complex biophysical processes due to limited process understanding. Recently, machine learning approaches trained on observational data have shown great potential in crop yield predictions. However, these models have not demonstrated improved performance over classical GGCMs and are not suitable for simulating crop yields under changing climate conditions due to problems in generalizing outside their training distributions. Here we introduce NeuralCrop, a hybrid GGCM that combines the strengths of an advanced process-based GGCM, resolving important processes explicitly, with data-driven machine learning components. The model is first trained to emulate a competitive GGCM before it is fine-tuned on observational data. We show that NeuralCrop outperforms state-of-the-art GGCMs across site-level and large-scale cropping regions. Across moisture conditions, NeuralCrop reproduces the interannual yield anomalies in European wheat regions and the US Corn Belt more accurately during the period from 2000 to 2019 with particularly strong improvements under drought extremes. When generalizing to conditions unseen during training, NeuralCrop

continues to make robust projections, while pure machine learning models exhibit substantial performance degradation. Thanks to optimization to graphical processing units (GPUs), NeuralCrop is more than 80 times faster on a single GPU than a state-of-the-art competitor on 128 CPU cores. Our results show that our hybrid crop modelling approach offers overall improved crop modeling and more reliable yield projections under climate change and intensifying extreme weather conditions.

Introduction

Global food systems face intensifying threats from climate change, particularly extreme weather events [1–3]. Accurately assessing the impacts of changing weather and especially extreme event patterns on agricultural productivity is crucial for the development of adaptation strategies to mitigate adverse effects and sustain future food security [4, 5]. Over the past decades, global gridded crop models (GGCMs) have become essential tools for assessing the impacts of climate change on agricultural production [6, 7], and are extensively used in downstream analyses (e.g., food security [8, 9], sustainability [10], or economy [11]). Despite their wide use for climate impact assessments, state-of-the-art GGCMs retain substantial uncertainties in representing complex biophysical processes, varying by crop types and spatial scales [12–15]. For instance, GGCMs were initially developed and parameterized with focus on average climate conditions, leading to limitations in simulating the impacts of climate extremes on crop growth, such as drought and heat stress [16]. Given the projected increases in frequency and magnitude of extreme events in a warming climate [17], and their strong influence on future food security, these limitations are highly problematic. Moreover, parameter calibration for traditional GGCMs remains a time-consuming, manual process constrained by sparse observational data across crops and regions [18]. The difficulty of reducing process and parameter uncertainties in GGCMs presents major challenges for the reliability of crop yield projections and food risk assessments under climate change [19].

Machine learning (ML) approaches have emerged rapidly in agricultural ecosystem modelling [20–22]. These models are capable of learning complex, nonlinear interactions, which are difficult to explicitly resolve in process-based GGCMs, from observational data (e.g., remote sensing, field measurements, and regional agricultural statistics), providing an alternative for crop yield projections. ML approaches have been successfully used to emulate GGCMs to enable sensitivity and uncertainty analyses under input perturbations [23], and to downscale GGCM outputs to finer spatial and temporal resolutions [24]. Once trained, ML approaches typically require considerably lower computational costs and memory demands during inference than traditional GGCMs.

However, ML approaches also have significant limitations. They are mostly trained using root-mean-squared-error loss, a method that rewards averaging over uncertainty, consequently producing overly smoothed or even physically implausible predictions

when applied for long-term crop simulations [25]. As these models are purely data-driven, they capture only statistical correlations rather than realistic representations of biophysical processes, which leads to poor extrapolation performance when applied outside their training distributions (e.g., future climate scenarios) [20]. Furthermore, this lack of physical process representations results in limited interpretability, making it difficult to diagnose crop-climate interactions and to attribute yield responses to underlying mechanisms [26]. Ensuring generalization and physical consistency thus remains a primary barrier to the application of pure ML models in crop modelling. In addition, sparse and heterogeneous observational data further constrain training and evaluation of purely data-driven models [27]. Despite some success in using ML approaches for crop simulations, these models have not yet been shown to outperform state-of-the-art GGCMs [23, 24].

In light of the complementary benefits and limitations of process-based models and ML-based models, hybrid models have been proposed as a promising direction for model development [28, 29]. Processes in a physical model that are not formulated by first principles can be replaced or augmented using ML methods if sufficient observational data are available [30, 31]. This leads to a hybrid model, which leverages information from observational data to improve or replace processes that are poorly represented, while maintaining the physics-based core of the process-based model. Hybrid models have achieved notable success across diverse fields, outperforming pure ML models and traditional process-based models [32–34]. Several studies have recently explored combinations of ML models with process-based crop models [35–38], but ML methods in these models are typically used in a post-processing step to adjust outputs from process-based crop models, or used to emulate those models, rather than being integrated into their internal processes. To enable efficient gradient-based optimization of all parameters jointly and consistently, the hybrid model should support automatic differentiation [30]. However, existing traditional GGCMs are not differentiable. A key technical challenge for traditional GGCMs in this context is that they are typically written in Fortran or C, which struggle to support automatic differentiation and hinder ML integration into traditional GGCMs. This can be solved by using a language that is suitable for both process-based components and ML model training, like Python or Julia.

Here we introduce NeuralCrop, a hybrid GGCM that combines the strengths of the traditional GGCM LPJmL [39] with ML approaches using the Julia programming language. To achieve seamless integration with ML methods, the hybrid components within NeuralCrop are reimplemented in a differentiable form, which enables end-to-end ‘online training’, with ML components optimized in tandem with the model dynamics. Due to sparse observational data available for many agricultural systems, NeuralCrop is first pre-trained on GGCM outputs and further fine-tuned using a global network of site-level observations. Extensive benchmarking shows that, in comparison to LPJmL, NeuralCrop better reproduces the daily dynamics of ecosystem fluxes across diverse crop sites, and the interannual variability in crop yields within large-scale cropping regions. NeuralCrop performs better across a range of moisture conditions, with strongest improvements for extreme drought conditions. NeuralCrop also exhibits robust generalization capabilities when applied to out-of-sample

regions. In addition to detailed comparisons to LPJmL, we further compared the yield simulation ability of NeuralCrop with the ensemble median of five additional state-of-the-art GGCMS, i.e., pDSSAT [40], EPIC-IIASA [41], LDNDC [42], ISAM [43], and PEPIC [44].

NeuralCrop

NeuralCrop is based on the LPJmL ("Lund-Potsdam-Jena managed Land") model, which explicitly simulates carbon, water, energy, and nitrogen flows for both natural vegetation and agricultural crops at $0.5^\circ \times 0.5^\circ$ (latitude \times longitude) spatial and daily temporal resolution [39, 45–47]. LPJmL is a state-of-the-art process-based GGCMS and contributes to the global model intercomparison networks AgMIP and ISMIP [48, 49]. It has been comprehensively evaluated at the global scale [50–53]. In NeuralCrop, neural networks are embedded to replace or augment key biological processes of LPJmL that are uncertain or simplified but directly observable, such as photosynthesis and soil moisture dynamics, or to emulate processes that are heuristic, such as carbon allocation. The considered process-based components within NeuralCrop are fully differentiable to enable a seamless integration with neural networks. These are described in detail in the Supplementary Information B.

Given limited high-quality agricultural observations, we adopt a two-stage strategy to train NeuralCrop, as illustrated in Fig. 1. In the absence of sufficient observational data, pre-training NeuralCrop on extensive LPJmL simulations allows the ML components to learn physically consistent representations, especially for latent variables. This can accelerate and stabilize convergence during subsequent fine-tuning with observational data. End-to-end 'online training' allows NeuralCrop to account for interactions between ML and process-based components in a natural way, ensuring physical consistency in the learned representations [30]. Furthermore, NeuralCrop supports full graphics-processing-unit (GPU) acceleration, which makes global grid-based simulations, and especially large ensembles thereof, computationally much more efficient, in particular above a certain resolution or ensemble size.

We train NeuralCrop models at both the site and regional level for different crops. The training setup details can be found in the Supplementary Information section D. For site-level representations, we evaluate the ability of NeuralCrop to reproduce daily gross primary productivity (GPP), ecosystem respiration (RECO), net ecosystem exchange (NEE), and soil water content (SWC) against flux tower observations (see Supplementary Information section F). For large-scale cropping regions, we evaluate NeuralCrop's performance in reproducing yield against reported yield statistics across two representative and highly relevant large-scale cropping regions, i.e., European wheat regions and the US Corn Belt (see Supplementary Information section G).

Results

Long-term yield projections

Our evaluation setup focuses on the ability of NeuralCrop to capture the long-term interannual yield variability, which is a key requirement for GGCMS. After

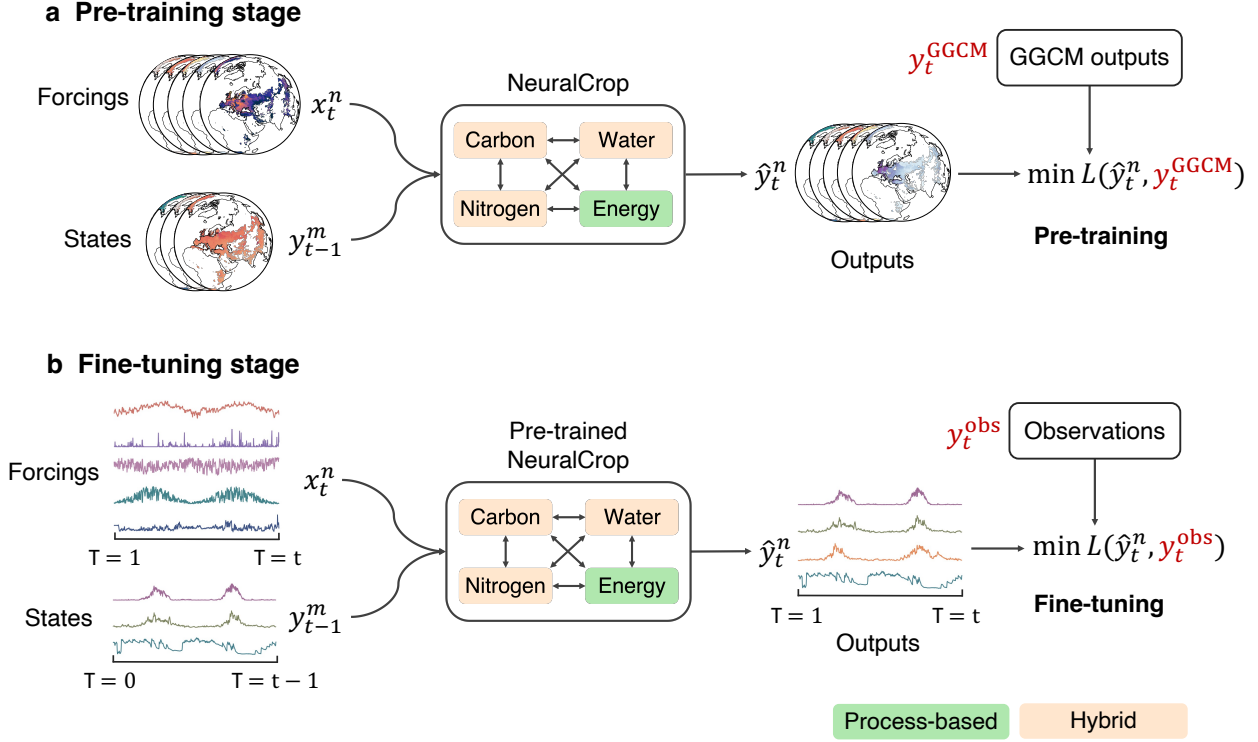


Fig. 1 Schematic of the NeuralCrop two-stage training framework. It shows how forcings x_t^n , including weather, soil properties, land use, and field management (e.g., crop calendar, tillage, residue, and fertilizer), and previous time-step model states y_{t-1}^m are fed into NeuralCrop at each time step t , where n denotes the number of forcing variables and m denotes the number of model states. These model states y_{t-1}^m are fed into the corresponding neural networks of hybrid components, which advance the evolution of model states over time. The new model states y_t^m are then fed back into the model to compute next time step. **a**, In the pre-training stage, NeuralCrop is trained to emulate the behavior of the process-based GGCM LPJmL by minimizing the discrepancies $L(\hat{y}_t^n, y_t^n)$ between NeuralCrop output \hat{y}_t^n and LPJmL output y_t^n , given identical weather, soil property, land use, and field management inputs. **b**, In the fine-tuning stage, the pre-trained NeuralCrop is further trained using observational data from eddy-covariance observation networks, which serve as ground truth.

pre-training, NeuralCrop and LPJmL exhibit a strong agreement in their simulated wheat and corn yields at the subnational level (Supplementary Information Figs. S10 and S13), indicating the feasibility of the hybrid approach. We compare simulated wheat yields from NeuralCrop and state-of-the-art GGCMs with the harmonized EU subnational crop statistics dataset [54] and corn yields with USDA statistics at the subnational level over the period 2000-2019. The simulated yields are aggregated using an area-weighted averaging method to the administrative units of yield statistics (see Methods and Supplementary Information G.3). Prior to comparison, all yield time series are detrended using a smoothing spline (Methods and Supplementary Information G.4). We focus on temporal correlations to evaluate model performance.

European wheat

The temporal correlations between simulated and statistical yields for each region over 2000-2019 are shown in Figures 2a-b. LPJmL simulations exhibit strong spatial heterogeneity, with high correlations in eastern Europe, but weak or even negative values in parts of Western and Southern Europe and especially most France, while NeuralCrop results present a more spatially consistent pattern of positive correlations. Figure 2c illustrates the spatial distribution of correlation difference between NeuralCrop and LPJmL (also see Supplementary Information Fig. S15). Among 775 subnational regions, NeuralCrop achieves higher correlation in 479 regions, accounting for 61.8%, with 149 regions (19.2%) showing notable improvements where the correlation increases more than 0.2, and only 29 regions (3.7%) exhibit a decrease in correlation exceeding 0.2. NeuralCrop shows pronounced improvement in Western Europe, particularly in France and its neighboring regions. These regions are consistent with the spatial distribution of eddy-covariance flux observations (see Supplementary Information Fig. S11), indicating that more comprehensive observational data is expected to further enhance NeuralCrop’s performance to capture interannual yield variability. At the country level, NeuralCrop achieves higher mean correlation in 20 out of 26 countries, as shown in Fig. 2d. For example, in France, the largest wheat producer in the EU [55], NeuralCrop shows strong improvements, where median correlation increases substantially (from 0.03 to 0.37), with more consistent performance across subnational regions. When compared against the ensemble median of five other GGCMs from AgMIP over the period 2000-2016, NeuralCrop also demonstrates strong performance in capturing interannual yield variability, achieving higher mean correlations across the majority of regions, as shown in Extended Data Fig. 6 (also see Supplementary Information Fig. S16). It is noted that the other AgMIP GGCMs also perform weakly in France, suggesting a common challenge for current GGCMs in this region. This further indicates that NeuralCrop provides a promising alternative to reduce biases in existing GGCMs.

US Corn Belt

For the US Corn Belt, we focus on a region including nine states (Supplementary Information Fig. S12), which accounts for about two-thirds of total US corn production [56]. Figures 3a,b show temporal correlations between simulated corn yields with statistical corn yields for each US county over the period 2000-2019, for LPJmL and NeuralCrop, respectively. Both models demonstrate comparable performance in capturing yield variability, exhibiting a similar spatial pattern of correlation across the US Corn Belt. Figure 3c illustrates the spatial distribution of correlation difference between NeuralCrop and LPJmL (also see Supplementary Information Fig. S17). Among 680 counties, NeuralCrop yields higher correlation in 361 counties, accounting for 53.1%, with 100 counties (14.7%) showing remarkable improvements where correlation increases more than 0.2, and 53 counties (7.8%) exhibit a decrease in correlation exceeding 0.2. NeuralCrop shows better performance in the northern and southern Corn Belt, consistent with the spatial distribution of eddy-covariance flux observations (see Supplementary Information Fig. S14), while LPJmL performs relatively well

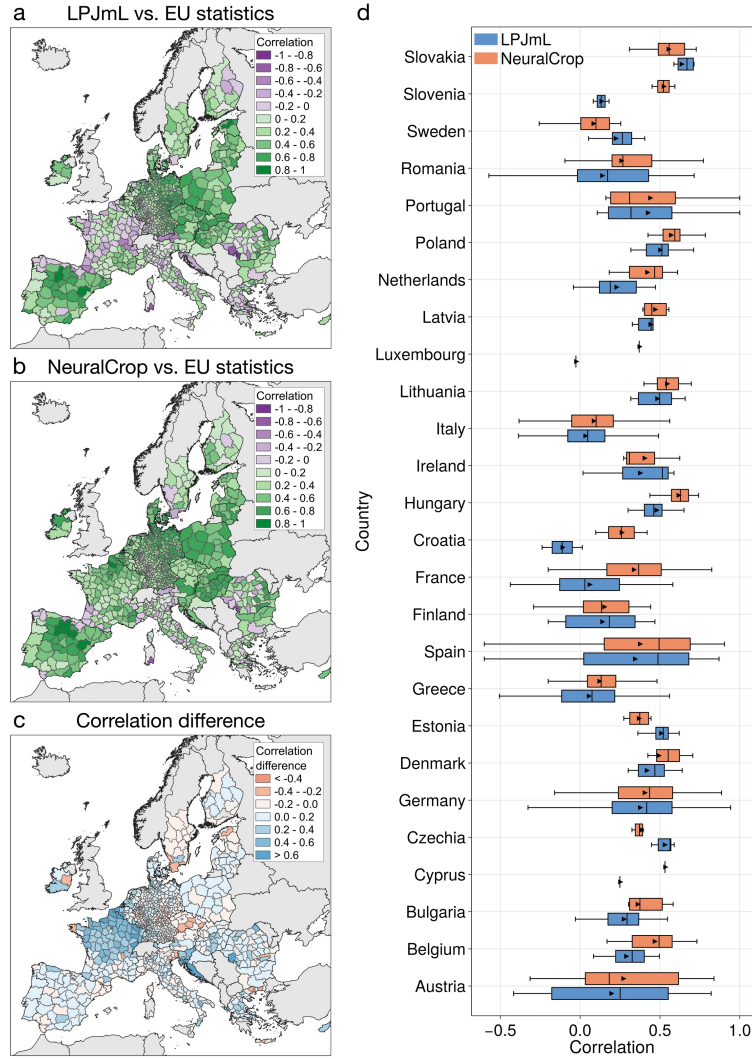


Fig. 2 Comparison of simulated European wheat yields from NeuralCrop and LPJmL with EU statistics in European wheat regions. **a**, Time series correlation coefficient between LPJmL simulated wheat yield and EU statistics at the subnational level for the period 2000–2019 (range from -1 to 1 , darker green areas indicate stronger positive correlations, and darker purple areas indicate stronger negative correlations). **b**, Same as (a) but for NeuralCrop. **c**, The difference of correlation coefficient (i.e., panel b – panel a), where blue areas indicate regions where NeuralCrop outperforms LPJmL in simulating interannual yield variability, and red areas indicate regions where LPJmL performs better. NeuralCrop performs better (worse) than LPJmL in 61.8% (38.2%) of all subnational regions. **d**, Boxplots of time series correlation coefficients between simulated wheat yield and EU statistics at the subnational level, aggregated by country for the period 2000–2019, with countries ordered alphabetically by their country code (A–Z). Blue boxes denote LPJmL, and orange boxes denote NeuralCrop. The box boundaries represent the interquartile range (IQR), defined by the first quartile, the median, and the third quartile. The upper and lower whiskers represent the maximum and minimum that are within 1.5 times the interquartile range of the box. The black triangles are the mean values.

in parts of the central Corn Belt. NeuralCrop achieves higher median correlation in seven out of nine states, i.e., Illinois, Indiana, Michigan, Minnesota, Missouri, South Dakota, and Wisconsin, while LPJmL performs better in Iowa and Ohio, as shown in Fig. 3d. NeuralCrop also shows competitive skill when compared to the ensemble median of other five GGCMs over the period 2000-2016, as shown in Extended Data Fig. 7 (also see Supplementary Information Fig. S18).

Out-of-sample generalization

Pure ML models typically exhibit poor performance in out-of-sample conditions, and even produce physically inconsistent predictions. We anticipate that NeuralCrop may generalize well in unseen conditions because of its hybrid modelling approach, where neural networks are used only to replace or augment selected sub-processes while simultaneously being constrained by other, explicitly resolved processes. To validate this hypothesis, we compared NeuralCrop with pure ML models (i.e., neural networks in the form of multi-layer perceptrons) that were trained on the European wheat cropping regions and used to simulate the US wheat cropping regions, respectively (Supplementary Information Fig. S19), a scenario entirely unseen during training. Results demonstrate that NeuralCrop presents robust spatial generalization capabilities, even outperforming the fully process-based LPJmL model in six out of eight states, with comparable performance in the remaining two (see Supplementary Information Fig. S20). In contrast, the pure ML model shows significantly weaker predictive skills across all states. This indicates that our hybrid NeuralCrop model provides a promising approach for accurate simulation of large-scale agricultural systems where observational data is scarce.

Accuracy across moisture conditions

We evaluate the ability of NeuralCrop to reproduce yield anomalies (Supplementary Information G.5) for European wheat and US Corn Belt across moisture conditions classified by the Standardized Precipitation Evapotranspiration Index (SPEI) of key growth, over the period 2000-2019. The SPEI is a drought index used to characterize drought intensity, duration, and frequency across different timescales [57] (Supplementary Information G.6). We use April–June SPEI for wheat and May–July SPEI for corn [58–60]. We further investigate the improved performance of NeuralCrop relative to LPJmL under extreme drought years, specifically the 2018 European drought and the 2012 US drought.

Yield anomalies across years

The statistics show that wheat yield anomalies become more negative under both drier and wetter conditions, suggesting increasing yield losses as dryness or wetness intensifies (Fig. 4a). In comparison, corn yield anomalies also decline with increasing dryness, but are considerably less sensitive to changes in wetness (Fig. 4b). NeuralCrop and LPJmL exhibit a consistent yield response pattern across moisture conditions. Under dry conditions, both NeuralCrop and LPJmL capture the overall trend of increasing yield losses as dryness intensifies for wheat and corn. However, NeuralCrop matches

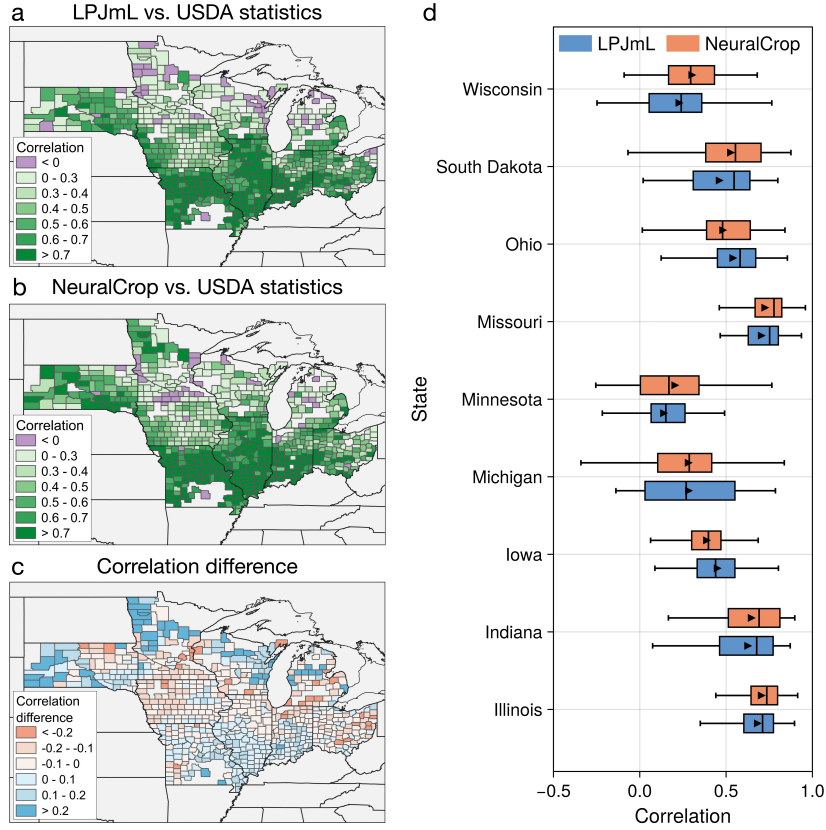


Fig. 3 Comparison of simulated corn yields from NeuralCrop and LPJmL with USDA statistics in the US Corn Belt, including nine states (i.e., South Dakota, Minnesota, Iowa, Missouri, Wisconsin, Illinois, Michigan, Indiana, and Ohio). **a**, Time series correlation coefficient between LPJmL simulated corn yield and USDA statistics at the country level for the period 2000–2019 (range from -1 to 1 , darker green areas indicate stronger positive correlations, and darker purple areas indicate stronger negative correlations). **b**, Same as (a) but for NeuralCrop. **c**, The difference of correlation coefficient (i.e., panel b – panel a), where blue areas indicate regions where NeuralCrop outperforms LPJmL in simulating interannual yield variability, and red areas indicate regions where LPJmL performs better. NeuralCrop performs better (worse) than LPJmL in 53.1% (46.9%) of all subnational regions. **d**, Boxplots of time series correlation coefficients between simulated corn yield and USDA statistics at the country level, aggregated by states for the period 2000–2019. Blue boxes represent LPJmL simulations vs. USDA statistics, and orange boxes represent NeuralCrop simulations vs. USDA statistics. The box boundaries represent the interquartile range (IQR), defined by the first quartile, the median, and the third quartile. The upper and lower whiskers represent the maximum and minimum that are within 1.5 times the interquartile range of the box. The black triangles are the mean values.

statistics in terms of root mean squared error (RMSE) more closely across all dryness classes, while LPJmL shows greater deviation with higher negative medians, a discrepancy that is more pronounced for corn. Notably, the ensemble median of AgMIP GCMs fails to capture wheat yield losses as dryness intensifies but rather simulates yield increases. For corn yield anomalies, AgMIP ensemble is less drought sensitive

than NeuralCrop (see Extended Data Fig. 8). Under wet conditions, LPJmL shows an increasing trend of yield gains for wheat and corn as wetness intensifies, inconsistent with observed yield anomalies. This likely stems from the fact that LPJmL does not explicitly simulate the impacts of water excess on crops, which limits its ability to reproduce yield anomalies across wetness gradients. While NeuralCrop exhibits a slightly increasing trend, it significantly mitigates the spurious yield gains shown by LPJmL. The ensemble median of AgMIP GGCMs shows broadly similar behavior to NeuralCrop under wet conditions. Across all moisture conditions, however, NeuralCrop consistently achieves lower root mean square error (RMSE) of yield anomalies than LPJmL. AgMIP GGCMs only show better simulations for corn under wet conditions. Corresponding yield anomaly bias patterns are illustrated in Supplementary Information Fig. S21 and Fig. S22. These results suggest that NeuralCrop provides a more consistent representation of yield responses across moisture conditions, particularly under extreme droughts where existing GGCMs show systematic limitations.

European wheat anomalies for the 2018 drought

In 2018, Northern, Central, and Eastern Europe were exposed to extreme droughts during the crucial growing stage of wheat, with extensive areas across these regions experiencing very dry and extremely dry conditions as diagnosed by April–June SPEI, whereas most of western France, Portugal, Spain, and the northern Mediterranean regions experienced normal to moderately dry conditions (Fig. 5a). These water deficits align with widespread negative wheat yield anomalies in 2018 (Fig. 5b). Almost all regions in Central and Northern Europe show particularly negative yield anomalies. Yield losses in these regions primarily range between 10% and 30%, with a substantial portion of areas suffering reductions exceeding 30%. In contrast, regions with normal and moderate dryness, particularly Portugal, Spain, and Romania, had yield increases ranging between 10% and 30% and some areas in Spain experienced increases exceeding 30%.

The yield responses to drought in both NeuralCrop and LPJmL are generally consistent with the findings over 2000–2019 (see Supplementary Information Fig. S23). LPJmL’s bias is more pronounced under the very dry conditions, while NeuralCrop maintains consistently lower bias across all dryness classes, as illustrated in Fig. 5e. We examine the coupling between simulated root-zone SWC and SPEI (Supplementary Information Fig. S24). We find that LPJmL shows increasing decoupling (weaker correlations) as dryness intensifies, while NeuralCrop maintains stronger and more stable coupling across dryness classes. Consistent with this, NeuralCrop shows a positive relationship between yield anomaly and simulated SWC, while LPJmL exhibits nearly no relationship between yield anomaly and SWC (Supplementary Information Fig. S25). Due to drought and heat typically occurring together, we further investigate their compound impacts on yield anomalies. We find that the maximum temperature during the growing season intensified the impact of drought on yield anomalies (Supplementary Information Fig. S27). Both LPJmL and NeuralCrop capture this compound effect, but NeuralCrop shows considerably lower biases (Supplementary Information Fig. S28). Moreover, we examine the water use efficiency (WUE, see Supplementary Information section G.7) from NeuralCrop and LPJmL under compound

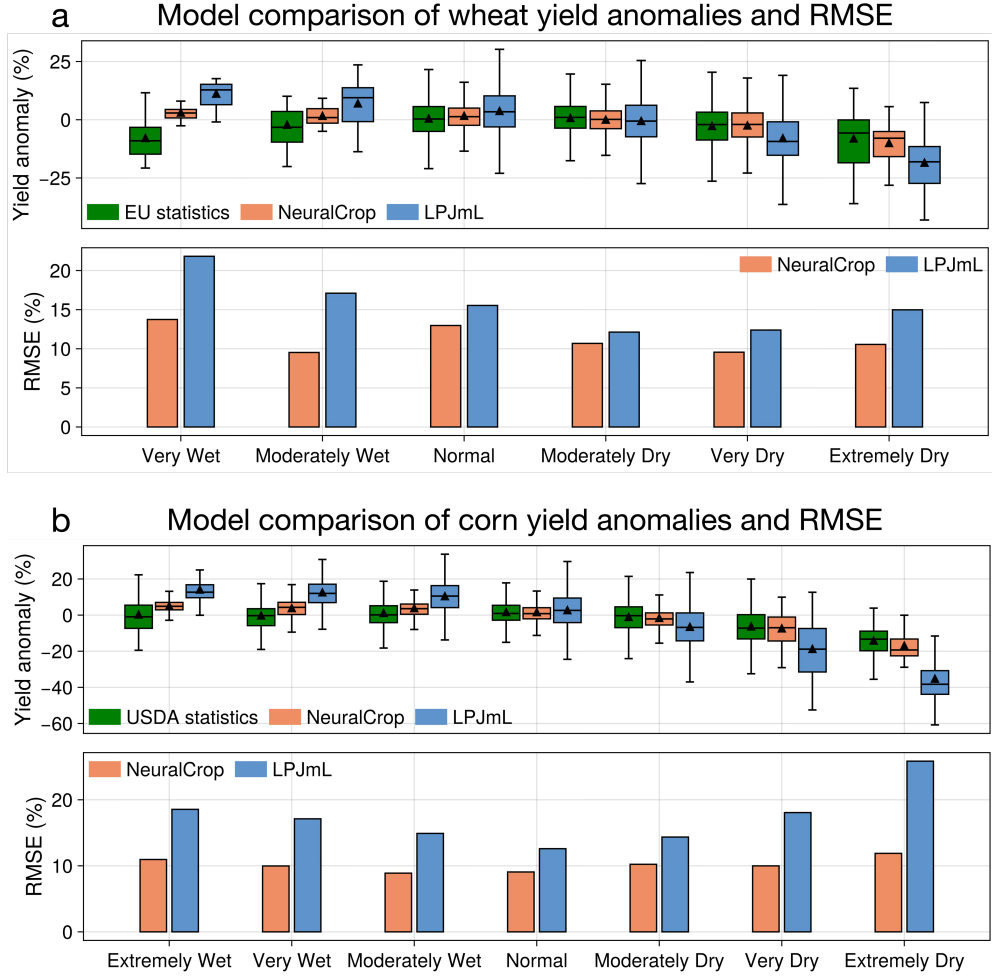


Fig. 4 Comparison of simulated yields from NeuralCrop and LPJmL with statistics for European wheat and US Corn Belt across moisture conditions at the subnational level during 2000–2019. **a**, The boxplots represent the wheat yield anomalies in EU over the period 2000–2019, grouped by the April–June Standardized Precipitation Evapotranspiration Index (SPEI) (Extremely Wet: $1.5 \leq \text{SPEI}$; Very Wet: $1.0 \leq \text{SPEI} < 1.5$; Moderately Wet: $0.5 \leq \text{SPEI} < 1.0$; Normal: $-0.5 \leq \text{SPEI} < 0.5$; Moderately Dry: $-1.0 \leq \text{SPEI} < -0.5$; Very Dry: $-1.5 \leq \text{SPEI} < -1.0$; Extremely Dry: $\text{SPEI} < -1.5$). Green boxes denote EU statistics, orange boxes denote NeuralCrop, and blue boxes denote LPJmL. The box boundaries represent the interquartile range (IQR), defined by the first quartile, the median, and the third quartile. The upper and lower whiskers represent the maximum and minimum that are within 1.5 times the interquartile range of the box. The black triangles are the mean values. The bars in the lower panel represent the root mean square error (RMSE) for NeuralCrop and LPJmL within each SPEI class. Orange bars denote NeuralCrop, and blue bars denote LPJmL. **b**, Same as panel a, but for corn yields evaluated against USDA statistics.

drought–heat conditions, NeuralCrop showing a stronger increase in WUE with intensifying drought and heat (Supplementary Information Fig. S29). These results suggest that NeuralCrop provides a more consistent representation of carbon–water coupling during droughts.

US corn anomalies for the 2012 drought

Most parts of the US Corn Belt experienced severe droughts during May–July in 2012 as diagnosed by SPEI (Fig. 5c), which previous studies have identified as the most relevant period for yield production [59, 60]. Central and southern regions (e.g., Iowa, Missouri, Illinois, and Indiana) were exposed to very dry and extremely dry conditions, and only a few northern regions experienced normal conditions. Yield anomalies present spatial patterns broadly consistent with dryness classes (Fig. 5d), which is similar to the European wheat case. Under these very dry and extremely dry conditions, with yield losses typically exceeding 20% in many counties, such as Missouri, Illinois, and Indiana, even exceeding 30%. Regions experiencing normal and moderately dry conditions show around 0%-10% yield increases, with some counties in Minnesota exceeding 10%.

As dryness intensified, LPJmL’s bias becomes more pronounced while NeuralCrop shows better agreement with USDA statistics with consistently lower bias (Fig. 5f and Supplementary Information Fig. S30). For the coupling between simulated root-zone SWC and SPEI (Supplementary Information Fig. S31), NeuralCrop exhibits higher correlations than LPJmL across dryness classes. We also investigate the compound drought–heat impacts on yield anomalies. Same to wheat, the maximum temperature during the growing season exacerbated the impact of drought on corn yield anomalies (Supplementary Information Fig. S33). Both LPJmL and NeuralCrop also capture this compound effect, but NeuralCrop shows lower biases (Supplementary Information Fig. S34). Furthermore, NeuralCrop shows a stronger increase in WUE with decreasing SPEI (drier conditions) and increasing growing season maximum temperature than LPJmL (Supplementary Information Fig. S35). These results further suggest that NeuralCrop can enhance the skill of process-based crop models in simulating carbon–water coupling.

Discussion

NeuralCrop can more accurately reproduce the daily and seasonal dynamics of carbon and water fluxes across diverse crop in-situ observation stations (Supplementary Information F). Interannual instability of crop yields is a critical determinant of food security under climate change [61], which is a key indicator for evaluating the performance of GGCMs. NeuralCrop exhibits more robust and spatially consistent predictions of interannual yield variability at large-scale cropping regions, here European wheat regions and the US Corn Belt. Traditional GGCMs can typically detect the sign of yield anomalies under climate extremes [62], but their capability to reproduce the magnitude and spatial patterns of such anomalies remains limited. Our results show that NeuralCrop is better at capturing yield anomalies under various moisture

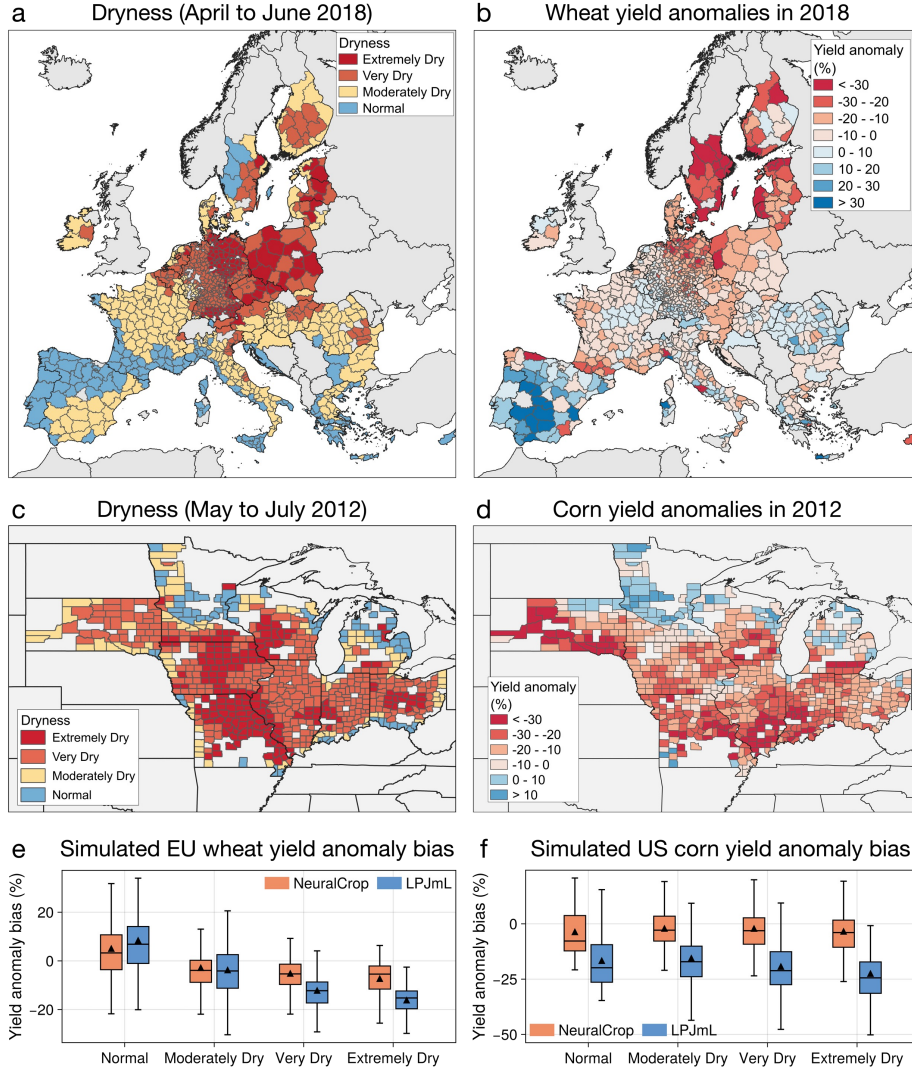


Fig. 5 Yield anomalies and model performance for NeuralCrop and LPJmL under the extreme drought years. **a**, April–June dryness category at the subnational level in the EU in 2018, classified by the April–June Standardized Precipitation Evapotranspiration Index (SPEI) (Normal: $-0.5 \leq \text{SPEI} < 0.5$; Moderately Dry: $-1.0 \leq \text{SPEI} < -0.5$; Very Dry: $-1.5 \leq \text{SPEI} < -1.0$; Extremely Dry: $\text{SPEI} < -1.5$). **b**, Wheat yield anomalies in 2018 at the subnational level from EU statistics. **c**, May–July dryness category at the county level in US Corn Belt in 2012, classified by the May–July SPEI (Normal: $-0.5 \leq \text{SPEI} < 0.5$; Moderately Dry: $-1.0 \leq \text{SPEI} < -0.5$; Very Dry: $-1.5 \leq \text{SPEI} < -1.0$; Extremely Dry: $\text{SPEI} < -1.5$). **d**, Corn yield anomalies in 2012 at the county level from USDA statistics. **e**, Boxplots of simulated wheat yield anomaly bias (i.e., the difference between simulated wheat yield anomalies and statistical yield anomalies) grouped by the dryness classes. Orange boxes denote NeuralCrop and blue boxes denote LPJmL. The box boundaries represent the interquartile range (IQR), defined by the first quartile, the median, and the third quartile. The upper and lower whiskers represent the maximum and minimum that are within 1.5 times the interquartile range of the box. The black triangles are the mean values. **f**, Same as panel e, but for simulated corn yield anomaly bias (%).

conditions with higher fidelity, especially under drought extremes. Overall, NeuralCrop shows that incorporating ML is a promising approach for reducing uncertainty in process representations and parameterizations within GGCMs.

NeuralCrop is, to our knowledge, the first hybrid, end-to-end 'online' trainable GGCM that combines the strengths of state-of-the-art GGCMs with ML approaches. Compared with 'offline' training, where the ML component is trained to learn processes independently of the evolving model states, end-to-end 'online' training enables ML components within NeuralCrop to continuously learn from and adjust the evolving model states. This co-evolution ensures that NeuralCrop maintains numerical stability over long-term simulations, preventing error accumulation [33], and also improves physical consistency. It is also the first hybrid crop model that achieves competitive and even improved model performance compared to traditional GGCMs.

As an abstract representation of a complex real-world system, many physical processes are represented simplistically or omitted in GGCMs [63]. For instance, the representation of soil waterlogging remains in its infancy in advanced GGCMs, and many GGCMs including LPJmL do not account for soil waterlogging mechanisms [64], consistent with our findings that LPJmL exhibits unrealistic yield gains with increasing wetness. Similarly, processes like the impacts of compound climate events and pest/disease stress are only partially simulated or not included in traditional GGCMs [12]. These gaps limit the ability of GGCMs to simulate the individual and combined effects of these stresses. As an example, LPJmL failed to detect the yield losses driven by heavy rainfall in combination with soil anoxia and diseases in central and northern France in 2016, and instead projected a yield increase (Supplementary Information Fig. S36) [58, 65]. While NeuralCrop inherits the same process limitations, it captures part of the negative but smaller yield anomalies in northern France after fine-tuning (Supplementary Information Figs. S36c-e). This suggests that, despite without an explicit representation of these processes in the model, the ML components can still learn from observational data to partially capture their indirect impacts. Furthermore, NeuralCrop is computationally efficient. For example, running NeuralCrop on a single GPU and LPJmL on 128 central-processing-unit (CPU) cores at 0.5° spatial resolution with daily time steps over 20 years, respectively, NeuralCrop achieved up to an $82.3\times$ speedup as the number of grid cells increased to 14,157 (Supplementary Information Table. S4). This can be used for previously highly time-consuming tasks such as large ensemble projections.

NeuralCrop is flexible to incorporate new process knowledge as our understanding of crop biophysical processes advances or with more ML components as higher-quality observational data becomes available. It also provides a powerful means to diagnose what processes are not well represented in the original GGCMs. Until now, the high-quality observational data suitable for the NeuralCrop training comes from eddy-covariance observation networks, but is very limited for crop types and locations (mainly located in Europe and US). In regions where more data is available like in France, results showed that NeuralCrop most strongly outperforms LPJmL. We hence expect that end-to-end 'online training', with observational data covering broader areas and longer time periods, will enable more realistic crop simulations. Current ML approaches for crop simulations face the common challenge of generalizing

to unseen data [20]. NeuralCrop has demonstrated robust out-of-sample generalization capabilities. We expect that it can be used to accurately simulate data-sparse, climate-vulnerable, and under-studied cropping regions, for example in Africa, South America, and Asia. Given ongoing climate change, more advanced and climate-robust GGCMS are needed to quantify the impacts of climate change and especially intensifying extreme weather events on agricultural productivity. We believe the hybrid modelling approach of NeuralCrop offers a promising avenue to advance GGCMS.

Methods

Pre-training data generation

We use LPJmL to generate data to pre-train NeuralCrop. The process-based LPJmL model simulates global carbon, water, and nitrogen fluxes and stocks, and surface energy balance for both natural vegetation and agricultural crops [39, 45–47]. As a contributing model to the global model intercomparison networks AgMIP and ISIMIP, LPJmL has been comprehensively evaluated at the global scale [48, 49, 51, 53]. For cropland, driven by climate forcing, soil properties, land use, and field management (e.g., crop calendar, tillage, residue, and fertilizer), LPJmL simulates key biophysical processes such as photosynthesis, carbon allocation, evapotranspiration, and soil moisture dynamics, as well as bioclimatic impacts on crop growth, development, yield formation across different crop functional types [45].

We ran LPJmL (version 5) on a global grid at $0.5^\circ \times 0.5^\circ$ (latitude \times longitude) spatial and daily temporal resolution [46]. An initial 5000-year spin-up simulation under potential natural vegetation (i.e., without land use) was performed to bring soil carbon, nitrogen, and water pools into dynamic equilibrium. Starting from these equilibrium states, a second 390-year spin-up simulation was conducted to introduce the impacts of historical land-use change on these pools. Both spin-up simulations used the first 30-year climate data cycled repeatedly to force LPJmL. The resulting model states ensure biophysically consistent initial conditions for subsequent transient simulations of crop growth. The detailed description can be found in the Supplementary Information section C.

NeuralCrop architecture

NeuralCrop explicitly resolved key processes, following their representation in the LPJmL model, but re-written to support automatic differentiation and GPU optimization, using the Julia programming language. NeuralCrop embeds ML components, here fully-connected neural networks, into the process-based crop model to replace or augment components that are uncertain or simplified (Supplementary Information B). Neural networks can theoretically be used to parameterize any biased or simplified process-based components within GGCMS [28]. In practice, however, their applicability is constrained by the availability of observational data for training. It is only feasible to combine neural networks with process-based components whose prognostic variables are observable. In agricultural ecosystems, high-quality observational data

remain scarce. While numerous remote sensing data are now available, their spatiotemporal resolutions are heterogeneous, making it difficult to use these data to train hybrid models [12]. Currently, global eddy-covariance observation networks (e.g., FLUXNET [66] and AmeriFlux [67]) provide continuous, high-quality daily observations of crop carbon and water fluxes. Training on these data allows neural networks to improve the representation of carbon and soil water-related processes in GGCMS. We described in detail in Supplementary Information B how key process-based components, i.e., photosynthesis, carbon allocation, soil carbon and nitrogen decomposition, and soil water dynamics, are combined with neural networks.

The considered process-based components of NeuralCrop are implemented in a fully differentiable manner to enable the end-to-end ‘online training’, which requires all processes along the backpropagation path to be differentiable by automatic differentiation (AD) [68]. Differentiability allows ML components to be optimized by taking into account interactions with their associated process-based components at each training iteration. We use neural ordinary differential equations (NODE) [69] in NeuralCrop to emulate daily carbon allocation (described in Supplementary Information B.2). Through ‘online training’, the NODE parameters are updated while accounting for interactions with internal prognostic states. Another big advantage of differentiability is that unobservable latent variables parameterized by neural networks can be implicitly optimized through backpropagation using target prognostic observations. For example, in NeuralCrop, we use two fully-connected neural networks to parameterize two latent variables in photosynthesis (i.e., λ , a key variable related to photosynthetic electron transport capacity, and maximum photosynthetic carboxylation rate V_{cmax}), respectively (described in Supplementary Information B.1). This approach enables NeuralCrop to capture the spatiotemporal variability of both λ and V_{cmax} using target GPP data, thereby reducing uncertainty in the representation of photosynthesis.

NeuralCrop is implemented in Julia [70], a high-performance and mature programming language for numerical and scientific computing, and its differentiability is supported by the automatic differentiation package Zygote.jl [71]. NeuralCrop is initialized using equilibrium states of soil carbon, nitrogen, and water pools generated from LPJmL simulations. All climate inputs to neural networks are standardized to a normal distribution with zero mean and unit variance, while prognostic variable inputs are linearly scaled to the range $[0, 1]$ using their physical limits. NeuralCrop is optimized for GPUs, which is computationally efficient due to its neural-network components and grid-based simulations.

Two-stage training approach

Due to the limited high-quality observational data, we adopt a two-stage training approach to train NeuralCrop at $0.5^\circ \times 0.5^\circ$ (latitude \times longitude) spatial and daily temporal resolution (Fig. 1). During the pre-training stage, we train NeuralCrop on LPJmL outputs using a loss function composed of two terms (Supplementary Information D.3, Eq. 24). The first loss term promotes predictive accuracy by minimizing discrepancies between NeuralCrop predictions and LPJmL outputs, while the second loss term imposes physical constraints to obey carbon mass balance. We then fine-tune

the pre-trained model using real-world observations, specifically the carbon and water flux data from eddy-covariance observation networks, using the accuracy loss function (Supplementary Information D.3, Eq. 25). The processing of flux data is described in detail in Supplementary Information C.4. The fine-tuning adjusts the model to better match observed carbon and water dynamics by correcting biases inherited from LPJmL. All model outputs used for training are normalized by their respective maximum value computed prior to model initialization, and all loss terms are defined using the standard mean squared error (MSE) (Supplementary Information D.3, Eq. 23).

We use a rollout length that covers the entire crop growing period (from sowing to harvest) to both pre-train and fine-tune NeuralCrop, which we find enables stable and robust model training (Supplementary Information D.5). Although shorter rollouts offer higher training efficiency, they often lead to loss oscillation and convergence failures. This instability becomes more pronounced as the rollout length decreases, highlighting the importance of incorporating the entire crop growing period into each training rollout. We set a 365-day rollout as the default to train all NeuralCrop models in our study.

Yield evaluation

We select European wheat regions and the US Corn Belt over the period 2000-2019 to evaluate the performance of NeuralCrop under both normal and extreme climate conditions. These two large-scale cropping regions are selected because of their long-term, high-quality eddy-covariance observations for fine-tuning, as well as annual subnational crop yield statistics for evaluation. Yield data used for evaluation are publicly available from the harmonized European Union subnational crop statistics dataset [54] and the USDA-NASS database, as described in Supplementary Information G.1.1 and G.2.1. The objective is to assess whether NeuralCrop can reproduce not only interannual yield variability but also yield anomalies under various climate conditions. The yield simulations from the other five GGCs (i.e., pDSSAT, EPIC-IIASA, LDNDC, ISAM, and PEPIC) are accessible from AgMIP GGCMI Phase 3, which provides historical yield simulations up to 2016.

To compare with observed yields, we aggregate simulated yields of NeuralCrop, LPJmL, and other five GGCs to the minimum administrative unit (primarily NUTS-3 level in EU countries, and county level in the US) using an area-weighted averaging method respectively, as described in Supplementary Information G.3. In European wheat regions, spring and winter wheat are simulated under rain-fed and irrigated management conditions, which are jointly evaluated against observed total wheat yields, including soft and durum wheat. In the US Corn Belt, corn is simulated under rain-fed and irrigated management conditions to compare with observed yields, using the same spatial aggregation method. When conducting out-of-sample validation in US wheat regions, the yield processing method is identical to that used in European wheat regions. Prior to comparison, both simulated and observed yield time series are detrended using a smoothing spline to remove the effects of long-term crop breeding advances and management improvements, thereby isolating the interannual variability primarily driven by climate change, described in Supplementary Information G.4.

Further analyses focus on the capability of NeuralCrop to capture yield anomalies across moisture conditions over 2000-2019. We then select the European 2018 drought and the US 2012 drought as case studies to conduct an in-depth investigation into the improved performance of NeuralCrop relative to LPJmL under extreme drought years. In 2018, the severe summer drought in combination with heatwaves in Northern, Central, and Eastern Europe resulted in a substantial drop in wheat production [72]. In the US, the 2012 drought resulted in a 13% decrease in corn production in the Corn Belt compared to 2011 [73].

For interannual yield variability, we use the Pearson correlation coefficient (Supplementary Information section E.1) or the Spearman correlation coefficient (Supplementary Information section E.2) as a metric to evaluate the performance of NeuralCrop. For yield anomalies, we use root mean square error (RMSE) (Supplementary Information section E.3) as the evaluation metric.

Data availability

For running LPJmL and training NeuralCrop, we used the bias-corrected climate inputs from ISIMIP3a GSWP3-W5E5 datasets for the period 1901–2019, which are publicly available for download at <https://www.isimip.org/>. The data for cultivated area fraction (850-2015) and annual fertilizer rates (1900-2015) were obtained from the LUH2v2 dataset [74]. The crop residue data for the period 1850-2015 were accessed from ref. [75]. The crop tillage management data covering 1973–2010 were obtained from ref. [76]. Soil properties (e.g., soil textures and pH) and crop sowing dates were accessed from Agricultural Model Intercomparison and Improvement Project (AgMIP) [51].

The flux data used to finetune NeuralCrop were obtained from the global flux network FLUXNET2015 (<https://fluxnet.org/data/fluxnet2015-dataset/>) and FLUXNET-CH4 (<https://fluxnet.org/data/fluxnet-ch4-community-product/>), the American flux network AmeriFlux (<https://ameriflux.lbl.gov/data/flux-data-products/>), and the European Integrated Carbon Observation System (ICOS) (<https://www.icos-cp.eu/data-products/>).

The subnational wheat statistics of the European Union were downloaded from <https://data.jrc.ec.europa.eu/dataset/685949ff-56de-4646-a8df-844b5bb5f835>, which provides annual wheat (including soft and durum wheat) statistics on area, production, and average yield across three levels of the Nomenclature of Territorial Units for Statistics (NUTS). The subnational corn statistics of the US Corn Belt were obtained from <https://quickstats.nass.usda.gov/>. The yield simulations from the other five GGCMS are available at <https://www.isimip.org/>.

Code availability

The NeuralCrop Julia code will be available on GitHub when this work gets published.

Supplementary information

The manuscript is accompanied by Supplementary Information that describes in detail how to develop, train, and validate NeuralCrop, as well as additional results.

Author contribution

Y.L., S.B., M.B., M.G., P.H. and N.B. conceived and designed the study. Y.L. wrote the model code, processed the data, trained the models and analysed the results. J.H. provided the yield comparison code. All authors discussed the results. Y.L. wrote the manuscript with contributions from all authors.

Acknowledgements

Y.L. acknowledges funding from the program of the China Scholarship Council (no.202303250017). N.B. and S.B. acknowledge funding from the Volkswagen Foundation. This is ClimTip contribution #X; the ClimTip project has received funding from the European Union’s Horizon Europe research and innovation programme under grant agreement no.101137601. The authors gratefully acknowledge the Ministry of Research, Science and Culture (MWFK) of Land Brandenburg for supporting this project by providing resources on the high performance computer system at the Potsdam Institute for Climate Impact Research.

References

- [1] Yang, Y., Tilman, D., Jin, Z., Smith, P., Barrett, C.B., Zhu, Y.-G., Burney, J., D’Odorico, P., Fantke, P., Fargione, J., *et al.*: Climate change exacerbates the environmental impacts of agriculture. *Science* **385**(6713), 3747 (2024)
- [2] Rezaei, E.E., Webber, H., Asseng, S., Boote, K., Durand, J.L., Ewert, F., Martre, P., MacCarthy, D.S.: Climate change impacts on crop yields. *nature reviews earth & environment* **4**(12), 831–846 (2023)
- [3] Hasegawa, T., Sakurai, G., Fujimori, S., Takahashi, K., Hijioka, Y., Masui, T.: Extreme climate events increase risk of global food insecurity and adaptation needs. *Nature Food* **2**(8), 587–595 (2021)
- [4] Hultgren, A., Carleton, T., Delgado, M., Gergel, D.R., Greenstone, M., Houser, T., Hsiang, S., Jina, A., Kopp, R.E., Malevich, S.B., *et al.*: Impacts of climate change on global agriculture accounting for adaptation. *Nature* **642**(8068), 644–652 (2025)
- [5] Lesk, C., Rowhani, P., Ramankutty, N.: Influence of extreme weather disasters on global crop production. *Nature* **529**(7584), 84–87 (2016)
- [6] Jägermeyr, J., Müller, C., Ruane, A.C., Elliott, J., Balkovic, J., Castillo, O., Faye, B., Foster, I., Folberth, C., Franke, J.A., *et al.*: Climate impacts on global agriculture emerge earlier in new generation of climate and crop models. *Nature Food* **2**(11), 873–885 (2021)
- [7] Adrian, R., Craig, M., Degvold, F., Ebi, K.L., Frieler, K., Jamshed, A., McMillan, J., Mechler, R., New, M., Simpson, N., *et al.*: Climate change 2022-impacts, adaption and vulnerability. summary for policymakers (2022)
- [8] Beier, F.D., Dietrich, J.P., Heinke, J., Abrahao, G., Jeetze, P., Bodirsky, B.L., *et al.*: Planetary boundaries under a land-based climate change mitigation scenario with a food demand transformation: a modelling study. *The Lancet Planetary Health* **9**(10), 101249 (2025) [https://doi.org/10.1016/S2542-5196\(25\)00087-7](https://doi.org/10.1016/S2542-5196(25)00087-7)
- [9] Luchtenbelt, H., Doelman, J., Bos, A., Daioglou, V., Jägermeyr, J., Müller, C., Stehfest, E., Vuuren, D.: Quantifying food security and mitigation risks consequential to climate change impacts on crop yields. *Environmental Research Letters* **20**(1), 014001 (2024)
- [10] Kahiluoto, H., Sakieh, Y., Kaseva, J., Kersebaum, K.-C., Minoli, S., Franke, J., Rötter, R.P., Müller, C.: Redistribution of nitrogen to feed the people on a safer planet. *PNAS nexus* **3**(5), 170 (2024)
- [11] Orlov, A., Jägermeyr, J., Müller, C., Daloz, A.S., Zabel, F., Minoli, S., Liu, W., Lin, T.-S., Jain, A.K., Folberth, C., *et al.*: Human heat stress could offset potential

economic benefits of co2 fertilization in crop production under a high-emissions scenario. *One Earth* **7**(7), 1250–1265 (2024)

- [12] Wang, B., Jägermeyr, J., O’Leary, G.J., Wallach, D., Ruane, A.C., Feng, P., Li, L., Liu, D.L., Waters, C., Yu, Q., *et al.*: Pathways to identify and reduce uncertainties in agricultural climate impact assessments. *Nature Food* **5**(7), 550–556 (2024)
- [13] Xiong, W., Asseng, S., Hoogenboom, G., Hernandez-Ochoa, I., Robertson, R., Sonder, K., Pequeno, D., Reynolds, M., Gerard, B.: Different uncertainty distribution between high and low latitudes in modelling warming impacts on wheat. *Nature Food* **1**(1), 63–69 (2020)
- [14] Asseng, S., Ewert, F., Rosenzweig, C., Jones, J.W., Hatfield, J.L., Ruane, A.C., Boote, K.J., Thorburn, P.J., Rötter, R.P., Cammarano, D., *et al.*: Uncertainty in simulating wheat yields under climate change. *Nature climate change* **3**(9), 827–832 (2013)
- [15] Müller, C., Jägermeyr, J., Franke, J.A., Ruane, A.C., Balkovic, J., Ciais, P., Dury, M., Falloon, P., Folberth, C., Hank, T., Hoffmann, M., Izaurralde, R.C., Jacquemin, I., Khabarov, N., Liu, W., Olin, S., Pugh, T.A.M., Wang, X., Williams, K., Zabel, F., Elliott, J.W.: Substantial Differences in Crop Yield Sensitivities Between Models Call for Functionality-Based Model Evaluation. *Earth’s Future* **12**(3), 2023–003773 (2024) <https://doi.org/10.1029/2023EF003773>
- [16] Minoli, S., Jägermeyr, J., Asseng, S., Urfels, A., Müller, C.: Global crop yields can be lifted by timely adaptation of growing periods to climate change. *Nature Communications* **13**(1), 7079 (2022)
- [17] Lee, H., Calvin, K., Dasgupta, D., Krinner, G., Mukherji, A., Thorne, P., Trisos, C., Romero, J., Aldunce, P., Barrett, K., *et al.*: IPCC, 2023: Climate Change 2023: Synthesis Report. Contribution of Working Groups I, II and III to the Sixth Assessment Report of the Intergovernmental Panel on Climate Change, (2023)
- [18] Gao, Y., Wallach, D., Liu, B., Dingkuhn, M., Boote, K.J., Singh, U., Asseng, S., Kahveci, T., He, J., Zhang, R., *et al.*: Comparison of three calibration methods for modeling rice phenology. *Agricultural and Forest Meteorology* **280**, 107785 (2020)
- [19] Koehler, A.-K.: Uncertainties in global crop modelling. *Nature Food* **1**(1), 19–20 (2020)
- [20] Sweet, L.-b., Athanasiadis, I.N., Bree, R., Castellano, A., Martre, P., Paudel, D., Ruane, A.C., Zscheischler, J.: Transdisciplinary coordination is essential for advancing agricultural modeling with machine learning. *One Earth* **8**(4) (2025)
- [21] Liu, L., Zhou, W., Guan, K., Peng, B., Xu, S., Tang, J., Zhu, Q., Till, J., Jia, X., Jiang, C., *et al.*: Knowledge-guided machine learning can improve carbon cycle

- quantification in agroecosystems. *Nature communications* **15**(1), 357 (2024)
- [22] Van Klompenburg, T., Kassahun, A., Catal, C.: Crop yield prediction using machine learning: A systematic literature review. *Computers and electronics in agriculture* **177**, 105709 (2020)
 - [23] Liu, W., Ye, T., Müller, C., Jägermeyr, J., Franke, J.A., Stephens, H., Chen, S.: The statistical emulators of ggcmi phase 2: responses of year-to-year variation of crop yield to co₂, temperature, water, and nitrogen perturbations. *Geoscientific Model Development* **16**(23), 7203–7221 (2023)
 - [24] Folberth, C., Baklanov, A., Balkovič, J., Skalský, R., Khabarov, N., Obersteiner, M.: Spatio-temporal downscaling of gridded crop model yield estimates based on machine learning. *Agricultural and forest meteorology* **264**, 1–15 (2019)
 - [25] Terven, J., Cordova-Esparza, D.-M., Romero-González, J.-A., Ramírez-Pedraza, A., Chávez-Urbiola, E.: A comprehensive survey of loss functions and metrics in deep learning. *Artificial Intelligence Review* **58**(7), 195 (2025)
 - [26] Paudel, D., De Wit, A., Boogaard, H., Marcos, D., Osinga, S., Athanasiadis, I.N.: Interpretability of deep learning models for crop yield forecasting. *Computers and Electronics in Agriculture* **206**, 107663 (2023)
 - [27] Tseng, G., Kerner, H., Nakalembe, C., Becker-Reshef, I.: Learning to predict crop type from heterogeneous sparse labels using meta-learning. In: *Proceedings of the IEEE/CVF Conference on Computer Vision and Pattern Recognition*, pp. 1111–1120 (2021)
 - [28] Reichstein, M., Camps-Valls, G., Stevens, B., Jung, M., Denzler, J., Carvalhais, N., Prabhat, F.: Deep learning and process understanding for data-driven earth system science. *Nature* **566**(7743), 195–204 (2019)
 - [29] Irrgang, C., Boers, N., Sonnewald, M., Barnes, E.A., Kadow, C., Staneva, J., Saynisch-Wagner, J.: Towards neural earth system modelling by integrating artificial intelligence in earth system science. *Nature Machine Intelligence* **3**(8), 667–674 (2021)
 - [30] Gelbrecht, M., White, A., Bathiany, S., Boers, N.: Differentiable programming for earth system modeling. *Geoscientific Model Development* **16**(11), 3123–3135 (2023)
 - [31] Shen, C., Appling, A.P., Gentine, P., Bandai, T., Gupta, H., Tartakovsky, A., Baity-Jesi, M., Fenicia, F., Kifer, D., Li, L., *et al.*: Differentiable modelling to unify machine learning and physical models for geosciences. *Nature Reviews Earth & Environment* **4**(8), 552–567 (2023)
 - [32] Liu, Y., Huang, H., Wang, S.-C., Zhang, T., Xu, D., Chen, Y.: Elm2. 1-xgbfire1.

- 0: improving wildfire prediction by integrating a machine learning fire model in a land surface model. *Geoscientific Model Development* **18**(13), 4103–4117 (2025)
- [33] Kochkov, D., Yuval, J., Langmore, I., Norgaard, P., Smith, J., Mooers, G., Klöwer, M., Lottes, J., Rasp, S., Düben, P., *et al.*: Neural general circulation models for weather and climate. *Nature* **632**(8027), 1060–1066 (2024)
 - [34] Zhang, C., Perezhogin, P., Gultekin, C., Adcroft, A., Fernandez-Granda, C., Zanna, L.: Implementation and evaluation of a machine learned mesoscale eddy parameterization into a numerical ocean circulation model. *Journal of Advances in Modeling Earth Systems* **15**(10), 2023–003697 (2023)
 - [35] Bloh, M., Lobell, D., Asseng, S.: Knowledge informed hybrid machine learning in agricultural yield prediction. *Computers and Electronics in Agriculture* **227**, 109606 (2024)
 - [36] Droutsas, I., Challinor, A.J., Deva, C.R., Wang, E.: Integration of machine learning into process-based modelling to improve simulation of complex crop responses. *in silico Plants* **4**(2), 017 (2022)
 - [37] Maestrini, B., Mimić, G., Oort, P.A., Jindo, K., Brdar, S., Athanasiadis, I.N., Evert, F.K.: Mixing process-based and data-driven approaches in yield prediction. *European Journal of Agronomy* **139**, 126569 (2022)
 - [38] Shahhosseini, M., Hu, G., Huber, I., Archontoulis, S.V.: Coupling machine learning and crop modeling improves crop yield prediction in the us corn belt. *Scientific reports* **11**(1), 1606 (2021)
 - [39] Schaphoff, S., Bloh, W., Rammig, A., Thonicke, K., Biemans, H., Forkel, M., Gerten, D., Heinke, J., Jägermeyr, J., Knauer, J., *et al.*: LPJmL4—a dynamic global vegetation model with managed land—part 1: Model description. *Geoscientific Model Development* **11**(4), 1343–1375 (2018)
 - [40] Jones, J.W., Hoogenboom, G., Porter, C.H., Boote, K.J., Batchelor, W.D., Hunt, L.A., Wilkens, P.W., Singh, U., Gijsman, A.J., Ritchie, J.T.: The dssat cropping system model. *European journal of agronomy* **18**(3-4), 235–265 (2003)
 - [41] Balkovič, J., Velde, M., Skalský, R., Xiong, W., Folberth, C., Khabarov, N., Smirnov, A., Mueller, N.D., Obersteiner, M.: Global wheat production potentials and management flexibility under the representative concentration pathways. *Global and Planetary Change* **122**, 107–121 (2014)
 - [42] Haas, E., Klatt, S., Fröhlich, A., Kraft, P., Werner, C., Kiese, R., Grote, R., Breuer, L., Butterbach-Bahl, K.: Landscapedndc: a process model for simulation of biosphere–atmosphere–hydrosphere exchange processes at site and regional scale. *Landscape ecology* **28**(4), 615–636 (2013)

- [43] Song, Y., Jain, A., McIsaac, G.: Implementation of dynamic crop growth processes into a land surface model: evaluation of energy, water and carbon fluxes under corn and soybean rotation. *Biogeosciences* **10**(12), 8039–8066 (2013)
- [44] Williams, J., Jones, C., Kiniry, J., Spanel, D.A.: The epic crop growth model. *Transactions of the ASAE* **32**(2), 497–0511 (1989)
- [45] Bondeau, A., Smith, P.C., Zaehle, S., Schaphoff, S., Lucht, W., Cramer, W., Gerten, D., LOTZE-CAMPEN, H., Müller, C., Reichstein, M., *et al.*: Modelling the role of agriculture for the 20th century global terrestrial carbon balance. *Global Change Biology* **13**(3), 679–706 (2007)
- [46] Bloh, W., Schaphoff, S., Müller, C., Rolinski, S., Waha, K., Zaehle, S.: Implementing the nitrogen cycle into the dynamic global vegetation, hydrology, and crop growth model lpjml (version 5.0). *Geoscientific Model Development* **11**(7), 2789–2812 (2018)
- [47] Lutz, F., Herzfeld, T., Heinke, J., Rolinski, S., Schaphoff, S., Von Bloh, W., Stoorvogel, J.J., Müller, C.: Simulating the effect of tillage practices with the global ecosystem model lpjml (version 5.0-tillage). *Geoscientific Model Development* **12**(6), 2419–2440 (2019)
- [48] Franke, J.A., Müller, C., Elliott, J., Ruane, A.C., Jägermeyr, J., Balkovic, J., Ciais, P., Dury, M., Falloon, P.D., Folberth, C., *et al.*: The gcmi phase 2 experiment: global gridded crop model simulations under uniform changes in co₂, temperature, water, and nitrogen levels (protocol version 1.0). *Geoscientific Model Development* **13**(5), 2315–2336 (2020)
- [49] Frieler, K., Volkholz, J., Lange, S., Schewe, J., Mengel, M., Rocío Rivas López, M., Otto, C., Reyer, C.P., Karger, D.N., Malle, J.T., *et al.*: Scenario setup and forcing data for impact model evaluation and impact attribution within the third round of the inter-sectoral impact model intercomparison project (isimip3a). *Geoscientific Model Development* **17**(1), 1–51 (2024)
- [50] Müller, C., Robertson, R.D.: Projecting future crop productivity for global economic modeling. *Agricultural Economics* **45**(1), 37–50 (2014)
- [51] Müller, C., Elliott, J., Chryssanthacopoulos, J., Arneth, A., Balkovic, J., Ciais, P., Deryng, D., Folberth, C., Glotter, M., Hoek, S., *et al.*: Global gridded crop model evaluation: benchmarking, skills, deficiencies and implications. *Geoscientific Model Development* **10**(4), 1403–1422 (2017)
- [52] Jägermeyr, J., Pastor, A., Biemans, H., Gerten, D.: Reconciling irrigated food production with environmental flows for sustainable development goals implementation. *Nature communications* **8**(1), 15900 (2017)
- [53] Schaphoff, S., Forkel, M., Müller, C., Knauer, J., Von Bloh, W., Gerten,

- D., Jägermeyr, J., Lucht, W., Rammig, A., Thonicke, K., *et al.*: Lpjml4—a dynamic global vegetation model with managed land—part 2: Model evaluation. *Geoscientific Model Development* **11**(4), 1377–1403 (2018)
- [54] Ronchetti, G., Nisini Scacchiafichi, L., Seguini, L., Cerrani, I., Velde, M.: Harmonized european union subnational crop statistics can reveal climate impacts and crop cultivation shifts. *Earth System Science Data* **16**(3), 1623–1649 (2024)
- [55] Nóia-Júnior, R.d.S., Martre, P., Deswarte, J.-C., Cohan, J.-P., Velde, M., Webber, H., Ewert, F., Ruane, A.C., Ben-Ari, T., Asseng, S.: Past and future wheat yield losses in france’s breadbasket. *Field Crops Research* **322**, 109703 (2025)
- [56] Lobell, D.B., Deines, J.M., Tommaso, S.D.: Changes in the drought sensitivity of us maize yields. *Nature Food* **1**(11), 729–735 (2020)
- [57] Vicente-Serrano, S.M., Beguería, S., López-Moreno, J.I.: A multiscalar drought index sensitive to global warming: the standardized precipitation evapotranspiration index. *Journal of climate* **23**(7), 1696–1718 (2010)
- [58] Nóia Júnior, R.d.S., Deswarte, J.-C., Cohan, J.-P., Martre, P., Der Velde, M., Lecerf, R., Webber, H., Ewert, F., Ruane, A.C., Slafer, G.A., *et al.*: The extreme 2016 wheat yield failure in france. *Global Change Biology* **29**(11), 3130–3146 (2023)
- [59] Zipper, S.C., Qiu, J., Kucharik, C.J.: Drought effects on us maize and soybean production: spatiotemporal patterns and historical changes. *Environmental Research Letters* **11**(9), 094021 (2016)
- [60] Deines, J.M., Archontoulis, S.V., Huber, I., Lobell, D.B.: Observational evidence for groundwater influence on crop yields in the united states. *Proceedings of the National Academy of Sciences* **121**(36), 2400085121 (2024)
- [61] Proctor, J., Zeppetello, L.V., Chan, D., Huybers, P.: Climate change increases the interannual variance of summer crop yields globally through changes in temperature and water supply. *Science Advances* **11**(36), 3575 (2025)
- [62] Heinicke, S., Frieler, K., Jägermeyr, J., Mengel, M.: Global gridded crop models underestimate yield responses to droughts and heatwaves. *Environmental Research Letters* **17**(4), 044026 (2022)
- [63] Nóia Júnior, R.d.S., Asseng, S., Müller, C., Deswarte, J.-C., Cohan, J.-P., Martre, P.: Negative impacts of climate change on crop yields are underestimated. *Trends Plant Sci.* **30**(11), 1262–1273 (2025) <https://doi.org/10.1016/j.tplants.2025.05.002>
- [64] Garcia-Vila, M., Santos Vianna, M., Harrison, M.T., Liu, K., S. Nóia-Júnior, R., Weber, T.K., Zhao, J., Acutis, M., Archontoulis, S., Asseng, S., *et al.*: Gaps and

- strategies for accurate simulation of waterlogging impacts on crop productivity. *Nature Food*, 1–10 (2025)
- [65] Ben-Ari, T., Boé, J., Ciais, P., Lecerf, R., Velde, M., Makowski, D.: Causes and implications of the unforeseen 2016 extreme yield loss in the breadbasket of france. *Nature communications* **9**(1), 1627 (2018)
 - [66] Pastorello, G., Trotta, C., Canfora, E., Chu, H., Christianson, D., Cheah, Y.-W., Poindexter, C., Chen, J., Elbashandy, A., Humphrey, M., *et al.*: The fluxnet2015 dataset and the oneflux processing pipeline for eddy covariance data. *Scientific data* **7**(1), 225 (2020)
 - [67] Chu, H., Christianson, D.S., Cheah, Y.-W., Pastorello, G., O’Brien, F., Geden, J., Ngo, S.-T., Hollowgrass, R., Leibowitz, K., Beekwilder, N.F., *et al.*: Ameriflux base data pipeline to support network growth and data sharing. *Scientific Data* **10**(1), 614 (2023)
 - [68] Gelbrecht, M., Klöwer, M., Boers, N.: Pseudospectralnet: Toward hybrid atmospheric models for climate simulations. *Journal of Advances in Modeling Earth Systems* **17**(10), 2025–004969 (2025)
 - [69] Chen, R.T., Rubanova, Y., Bettencourt, J., Duvenaud, D.K.: Neural ordinary differential equations. *Advances in neural information processing systems* **31** (2018)
 - [70] Bezanson, J., Edelman, A., Karpinski, S., Shah, V.B.: Julia: A fresh approach to numerical computing. *SIAM review* **59**(1), 65–98 (2017)
 - [71] Innes, M.: Don’t unroll adjoint: Differentiating ssa-form programs. *CoRR abs/1810.07951* (2018) [arXiv:1810.07951](https://arxiv.org/abs/1810.07951)
 - [72] Beillouin, D., Schauburger, B., Bastos, A., Ciais, P., Makowski, D.: Impact of extreme weather conditions on european crop production in 2018. *Philosophical Transactions of the Royal Society B* **375**(1810), 20190510 (2020)
 - [73] National Agricultural Statistics Service (NASS): Crop production 2012 summary. Technical report, U.S. Department of Agriculture, Washington, DC (2013)
 - [74] Hurtt, G.C., Chini, L., Sahajpal, R., Frolking, S., Bodirsky, B.L., Calvin, K., Doelman, J.C., Fisk, J., Fujimori, S., Goldewijk, K.K., *et al.*: Harmonization of global land-use change and management for the period 850–2100 (luh2) for cmip6. *Geoscientific Model Development Discussions* **2020**, 1–65 (2020)
 - [75] Dietrich, J.P., Mishra, A., Weindl, I., Bodirsky, B.L., Wang, X., Baumstark, L., Kreidenweis, U., Klein, D., Steinmetz, N., Chen, D., Humpenoeder, F., von Jeetze, P., Wirth, S., Beier, F., Hoetten, D., Sauer, P., Tommeyer, J.: mrland: MadRaT land data package. Version: 0.65.11 (2025). <https://doi.org/10.5281/zenodo.3822083> .

<https://github.com/pik-piam/mrland>

- [76] Porwollik, V., Rolinski, S., Heinke, J., Müller, C.: Generating a rule-based global gridded tillage dataset. *Earth System Science Data* **11**(2), 823–843 (2019)

Extended Data Figures

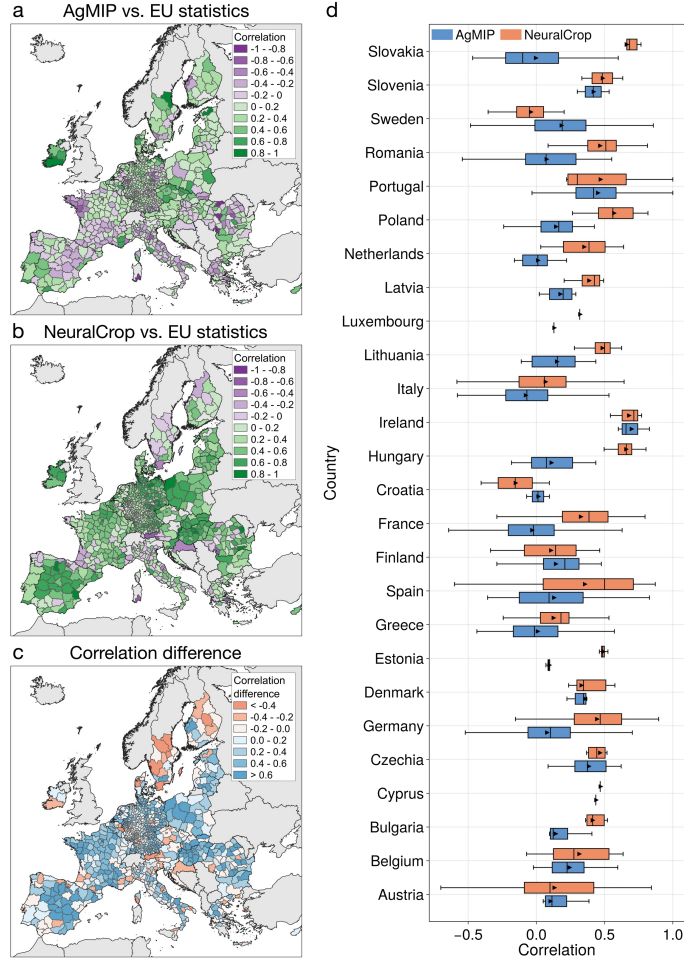


Fig. 6 Comparison of simulated European wheat yields from NeuralCrop and AgMIP crop models with EU statistics in European wheat regions. The AgMIP ensemble comprises five crop models: pDSSAT, EPIC-IIASA, LDNDC, ISAM, and PEPIC. statistics in European wheat regions. **a**, Time series correlation coefficient between AgMIP ensemble median wheat yield and EU statistics at the subnational level for the period 2000–2016 (range from -1 to 1 , darker green areas indicate stronger positive correlations, and darker purple areas indicate stronger negative correlations). **b**, Same as (a) but for NeuralCrop. **c**, The difference of correlation coefficient (i.e., panel b – panel a), where blue areas indicate regions where NeuralCrop outperforms AgMIP ensemble in simulating interannual yield variability, and red areas indicate regions where AgMIP ensemble performs better. NeuralCrop performs better (worse) than LPJmL in 78.7% (21.3%) of all subnational regions. **d**, Boxplots of time series correlation coefficient between simulated wheat yield and EU statistics at the subnational level, aggregated by country for the period 2000–2016, with countries ordered alphabetically by their country code (A–Z). Blue boxes denote AgMIP ensemble, and orange boxes denote NeuralCrop. The box boundaries represent the interquartile range (IQR), defined by the first quartile, the median, and the third quartile. The upper and lower whiskers represent the maximum and minimum that are within 1.5 times the interquartile range of the box. The black triangles are the mean values.

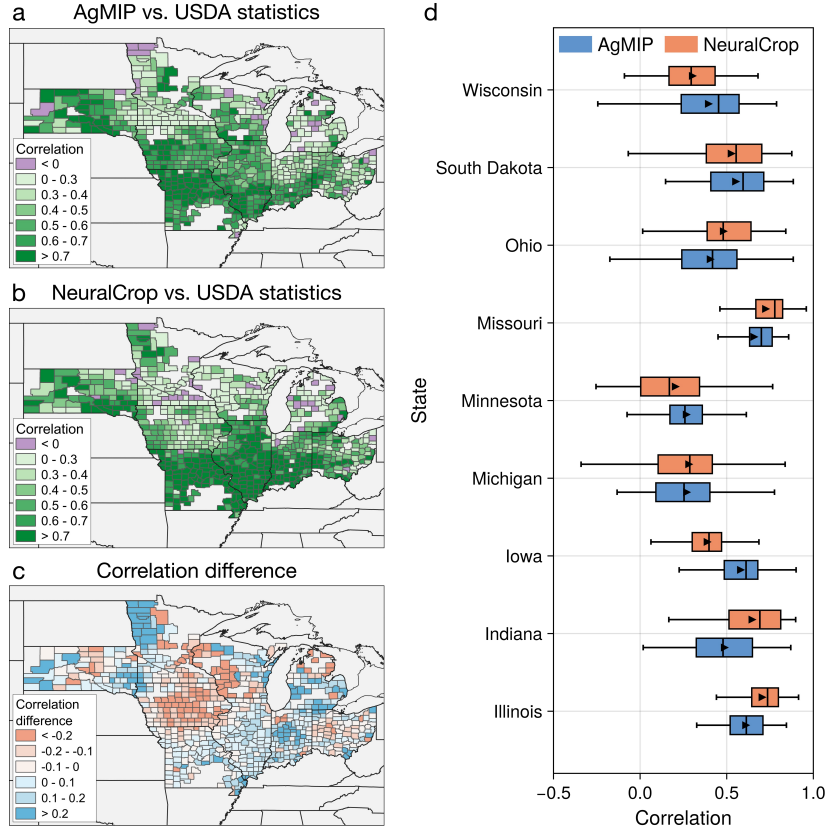


Fig. 7 Comparison of simulated corn yields from NeuralCrop and AgMIP crop models with USDA statistics in the US Corn Belt, including nine states (i.e., South Dakota, Minnesota, Iowa, Missouri, Wisconsin, Illinois, Michigan, Indiana, and Ohio). The AgMIP ensemble comprises five crop models: pDSSAT, EPIC-IIASA, LDNDC, ISAM, and PEPIC. **a**, Time series correlation coefficient between AgMIP ensemble median corn yield and USDA statistics at the country level for the period 2000–2016 (range from -1 to 1 , darker green areas indicate stronger positive correlations, and darker purple areas indicate stronger negative correlations). **b**, Same as (a) but for NeuralCrop. **c**, The difference of correlation coefficient (i.e., panel b – panel a), where blue areas indicate regions where NeuralCrop outperforms AgMIP ensemble in simulating interannual yield variability, and red areas indicate regions where AgMIP ensemble performs better. NeuralCrop performs better (worse) than LPJmL in 53.0% (47.0%) of all subnational regions. **d**, Boxplots of time series correlation coefficient between simulated corn yield and USDA statistics at the county level, aggregated by states for the period 2000–2016. Blue boxes denote AgMIP ensemble, and orange boxes denote NeuralCrop. The box boundaries represent the interquartile range (IQR), defined by the first quartile, the median, and the third quartile. The upper and lower whiskers represent the maximum and minimum that are within 1.5 times the interquartile range of the box. The black triangles are the mean values.

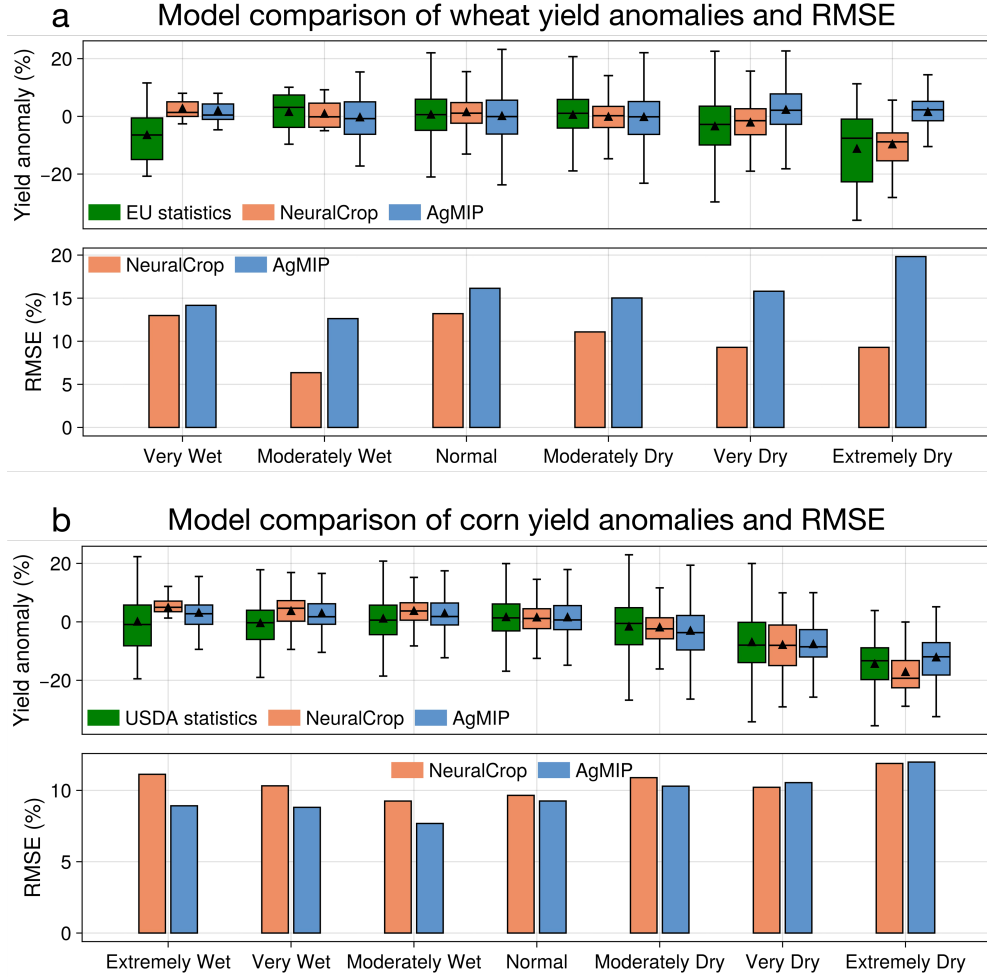


Fig. 8 Comparison of simulated yields from NeuralCrop and AgMIP crop models with statistics for European wheat and US Corn Belt across moisture conditions at the subnational level during 2000–2016. The AgMIP ensemble comprises five crop models: pDSSAT, EPIC-IIASA, LDNDC, ISAM, and PEPIC. **a**, The boxplots represent the wheat yield anomalies in EU over the period 2000–2016, grouped by the April–June Standardized Precipitation Evapotranspiration Index (SPEI) (Extremely Wet: $1.5 \leq \text{SPEI}$; Very Wet: $1.0 \leq \text{SPEI} < 1.5$; Moderately Wet: $0.5 \leq \text{SPEI} < 1.0$; Normal: $-0.5 \leq \text{SPEI} < 0.5$; Moderately Dry: $-1.0 \leq \text{SPEI} < -0.5$; Very Dry: $-1.5 \leq \text{SPEI} < -1.0$; Extremely Dry: $\text{SPEI} < -1.5$). Green boxes denote EU statistics, orange boxes denote NeuralCrop, and blue boxes denote AgMIP ensemble median. The box boundaries represent the interquartile range (IQR), defined by the first quartile, the median, and the third quartile. The upper and lower whiskers represent the maximum and minimum that are within 1.5 times the interquartile range of the box. The black triangles are the mean value. The bars below represent the root mean square error (RMSE) of yield anomalies for NeuralCrop and AgMIP ensemble within each SPEI class. Orange bars denote NeuralCrop, and blue bars denote AgMIP ensemble median. **b**, Same as panel a, but for corn yields evaluated against USDA statistics.

Supplementary information

A	Hybrid architecture	33
A.1	Dynamical Core of NeuralCrop	33
A.2	Neural network	33
A.3	Implementation	33
B	Trainable components of NeuralCrop	35
B.1	Photosynthesis	35
B.2	Crop carbon allocation	37
B.3	Soil and litter carbon cycle	38
B.4	Soil and litter nitrogen cycle	39
B.5	Soil water cycle	40
C	Data	42
C.1	Initial conditions	42
C.2	Pre-training data	42
C.3	Fine-tuning data	42
C.4	Data pre-processing	43
D	Training	45
D.1	Input data normalization	45
D.2	Optimizer settings	45
D.3	Loss function	45
D.4	Training sequence length	46
D.5	Training rollouts	46
D.6	Output rescaling	48
D.7	Training resources	48
E	Evaluation metrics	50
E.1	Pearson correlation coefficient	50
E.2	Spearman correlation coefficient	50
E.3	Root mean square error	50
F	In situ validation	52
F.1	In situ sites	52
F.2	Training	52
F.3	Results	53
G	Large-scale cropping regions	59
G.1	European wheat	59
G.1.1	Subnational crop statistics	59
G.1.2	Pre-training	59
G.1.3	Fine-tuning	60
G.2	US Corn Belt	61

G.2.1	County-level crop statistics	61
G.2.2	Pre-training	62
G.2.3	Fine-tuning	63
G.3	Yield aggregation	64
G.4	Yield detrending	64
G.5	Yield anomalies	65
G.6	Standardized Precipitation Evapotranspiration Index	65
G.7	Water use efficiency	66
H	Additional information	67
H.1	Long-term yield projection	67
H.1.1	European wheat	67
H.1.2	US Corn Belt	68
H.1.3	US wheat	69
H.2	Accuracy across moisture conditions	71
H.2.1	Yield anomalies over 2000–2019	71
H.2.2	European wheat anomalies in 2018	73
H.2.3	US Corn Belt anomalies in 2012	80
H.2.4	France wheat anomalies in 2016	86

A Hybrid architecture

A.1 Dynamical Core of NeuralCrop

NeuralCrop distinguishes between diagnostic and prognostic variables. Diagnostic variables, such as leaf area index (LAI) and gross primary productivity (GPP), represent instantaneous system states that are not explicitly dependent on the system’s temporal evolution. Prognostic variables, such as carbon pools, nitrogen pools and soil water pools, govern the dynamic evolution of the system states over time. They are represented by coupled ordinary differential equations (ODEs) that form the dynamical core of NeuralCrop in crop carbon, nitrogen, and water cycles, as described in detail in B. At each time step, diagnostic variables are updated based on the computed prognostic variables.

A.2 Neural network

In NeuralCrop, we combine fully-connected neural networks with process-based components, which are designed to learn key process representations from observational data, to reduce ‘hidden’ uncertainties inherent in process-based GGCMs. For diagnostic variables replaced or augmented by neural networks, we use a 5-layer MLP with ReLU activations and 384 hidden neurons. To capture temporal dependencies and continuous dynamics, we naturally use neural ordinary differential equations (NODEs) [1] to model prognostic variables, which are parameterized by a 3-layer MLP with ReLU activations and 384 hidden neurons. To solve the NODEs, we use a forward Euler solver with a fixed time step $\Delta t = 1$ day. At each time step t , the prognostic variable $\mathbf{X}(t)$ is updated according to:

$$\mathbf{X}(t + \Delta t) = \mathbf{X}(t) + \Delta t \cdot f_{\theta}(\mathbf{X}(t), t) \quad (1)$$

where f_{θ} denotes the MLP that outputs the learned tendencies.

A.3 Implementation

NeuralCrop adopts robust physical representations of ecosystem processes governing carbon, water, energy, and nitrogen fluxes from LPJmL, a state-of-the-art process-based model in simulating natural and agricultural ecosystems. To enable seamless integration with machine learning components, we translated the C-based crop module of LPJmL into Julia, a high-performance language designed for numerical and scientific computing [2]. The Julia ecosystem for scientific machine learning (SciML) provides native support for differential equations [3], which naturally fits well with our hybrid modeling approach using ODEs as the core of system dynamics.

We implement the ML components of NeuralCrop using Lux.jl [4, 5], a neural network framework built entirely with pure functions that are friendly to both compilers and automatic differentiation. We train the ML components of NeuralCrop using Zygote.jl [6], a high-performance automatic differentiation (AD) framework in Julia that enables efficient gradient-based optimization, accelerated by CUDA.jl [7, 8]. During training, the gradients of neural networks are computed via direct reverse-mode

differentiation, including the forward Euler solver used for the NODEs (i.e., gradients are obtained by backpropagating through the Euler solver rather than using adjoint methods). To support full graphics-processing-unit (GPU) compatibility and improve computational efficiency, we implement the process-based components using KernelAbstractions.jl [9], which allows both neural networks and process-based parts to be parallelized and executed within a unified GPU-accelerated framework.

B Trainable components of NeuralCrop

A detailed description of the model components of LPJmL can be found in Schaphoff et al. [10]. In this section, we focus on the components replaced or augmented by neural networks within NeuralCrop. The overall data flow in the learned components of NeuralCrop is shown in Fig. S1.

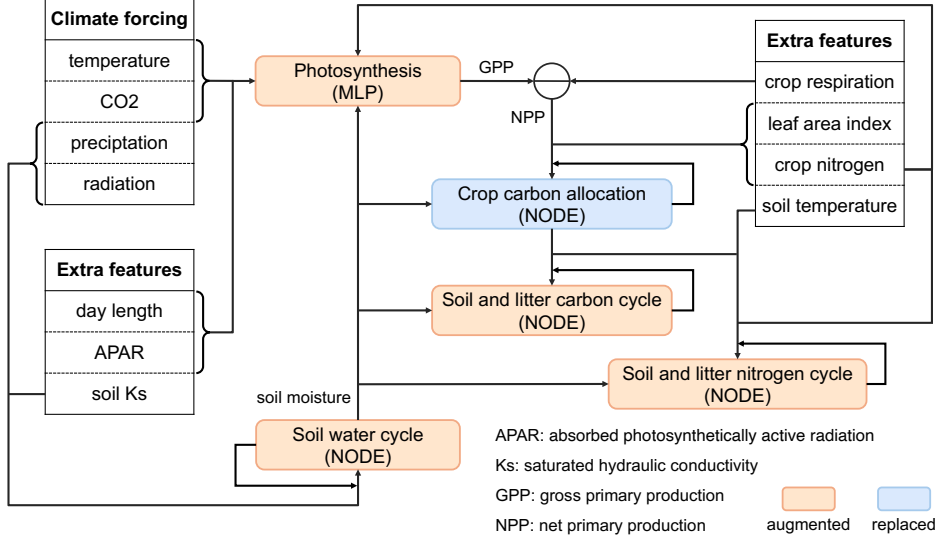


Fig. S1 Schematic of the data flow in the learned components of NeuralCrop.

B.1 Photosynthesis

The photosynthesis scheme follows a 'big leaf' model developed by Farquhar et al [11, 12], and improved by Collatz et al [13, 14] and Prentice et al [15, 16]. The daily gross photosynthesis rate A_{gd} ($\text{g C m}^{-2} \text{ day}^{-1}$) is calculated as the co-limited minimum of the light-limited photosynthesis rate J_E ($\text{mol C m}^{-2} \text{ h}^{-1}$) and the Rubisco-limited photosynthesis rate J_C ($\text{mol C m}^{-2} \text{ h}^{-1}$). The corresponding equations are:

$$J_E = C_1 \cdot \frac{\text{APAR}}{\text{daylength}}, \quad (2)$$

where C_1 is a temperature stress and stomatal conductance-related coefficient, APAR is the absorbed photosynthetically active radiation, and daylength is the length of day time.

$$J_C = C_2 \cdot V_{\max}, \quad (3)$$

where C_2 is the stomatal conductance-related coefficient, and V_{\max} is the maximum Rubisco capacity.

$$A_{\text{gd}} = \frac{\left(J_E + J_C - \sqrt{(J_E + J_C)^2 - 4 \cdot \theta \cdot J_E \cdot J_C} \right)}{2 \cdot \theta \cdot \text{daylength}}, \quad (4)$$

where θ is the co-limitation coefficient of light and Rubisco activity.

Here, we only present the final equation to obtain A_{gd} (Eq. 4) and omit the intermediate derivation steps, which are already described in detail in Schaphoff et al. [10]. In order to compute the optimal ratio of the inter-cellular to atmospheric CO_2 concentration, λ , the following equation must be solved (Eq. 5).

$$A_{\text{nd}} + (1 - \text{daylength}/24) \cdot R_{\text{leaf}} - p_a \cdot (g_c - g_{\min}) \cdot (1 - \lambda)/1.6 = 0, \quad (5)$$

where A_{nd} is daily net photosynthesis rate, R_{leaf} is leaf respiration, p_a is the atmospheric partial pressure of CO_2 , g_c is canopy conductance, g_{\min} is vegetation (crop) specific minimum canopy conductance. However, an analytical solution is not feasible because λ appears both directly in the equation and indirectly through A_{nd} . In LPJmL, a bisection algorithm is used to iteratively solve the equation and determine the value of λ , which introduces significant computational cost when conducting large-scale, high-resolution simulations.

To address this bottleneck, we replace the root-finding algorithm with a 5-layer MLP to emulate the solution for λ , which approximates the nonlinear relationship between environmental variables (i.e., day length, air temperature, and soil moisture) and the corresponding optimal value of λ . Compared to the bisection algorithm, the neural network-based emulator can significantly accelerate the photosynthesis computation, which is due to the fact that neural networks only need one forward pass for inference, while root-finding algorithms involve iterative evaluations.

Additionally, we use a second 5-layer MLP to simulate the maximum Rubisco capacity V_{\max} , originally computed using an empirical formulation (Eq. 6).

$$V_{\max} = (N_{\text{leaf}} - NC_{\text{leaf, low}} \cdot C_{\text{leaf}}) / (p \cdot \exp(k_{\text{temp}} \cdot (T - 25)) \cdot \text{LAI}) \cdot \text{daylength} \quad (6)$$

where N_{leaf} is the leaf nitrogen content, C_{leaf} is the leaf carbon content, $NC_{\text{leaf, low}}$ is the crop-specific lower ratio of leaf carbon and nitrogen, p is the static coefficient, k_{temp} is the factor of temperature dependence of nitrogen demand for Rubisco activity, T is the air temperature, LAI is the leaf area index. Instead of relying on a fixed empirical relationship, this neural network is trained using observational data to capture more complex and potentially nonlinear interactions between V_{\max} and its environmental and biochemical drivers (i.e., day length, APAR, leaf nitrogen, and air temperature).

Furthermore, we implement the photosynthesis module to be fully differentiable. By leveraging observational GPP, we are able to optimize λ and V_{\max} through gradient-based 'online training', which helps mitigate "hidden" biases introduced by the original empirical formulation of λ and V_{\max} .

B.2 Crop carbon allocation

In LPJmL, crop carbon allocation is governed by a set of heuristic rules driven by phenological development stage, organ priority, and stress factors. Daily NPP (net gross productivity) accumulates to total biomass, which is then allocated to crop organs in a hierarchical order: root, leaf, storage organ, mobile reserve, and stem [10]. The carbon allocation equations are:

$$C_{\text{root}} = f_{\text{root}} \cdot \text{biomass}, \quad (7)$$

$$C_{\text{leaf}} = \frac{\text{LAI}}{\text{sla}}, \quad (8)$$

$$C_{\text{so}} = \text{HI} \cdot (1 - f_{\text{root}}) \cdot \text{biomass}, \quad (9)$$

$$C_{\text{pool}} = \text{biomass} - C_{\text{root}} - C_{\text{leaf}} - C_{\text{so}}. \quad (10)$$

where f_{root} is the root carbon allocation coefficient (co-limited by water and nitrogen stress), sla is the specific leaf area, HI is the harvest index (limited by water stress). The daily carbon allocation is computed based solely on the current phenological and environmental conditions without tracking the dynamic evolution of carbon pools over time, which limits its ability to represent feedbacks and lagged responses.

The matrix-based carbon allocation framework proposed by Luo et al.[17] provides a promising approach to model carbon allocation dynamics. By representing carbon allocation as a system of ODEs(Eq. 11), it captures the temporal evolution of carbon pools in a continuous and prognostic manner.

$$\frac{dC(t)}{dt} = A(C, t)\mu(t) + B(C, t)\xi(t)K(C, t)C(t), \quad (11)$$

where $C(t)$ denotes the vector of carbon compartments, $A(C, t)$ is a vector of allocation coefficients, $\mu(t)$ is carbon input (e.g., NPP), $B(C, t)$ is a matrix of transfer coefficients, $\xi(t)$ is a matrix of environmental modifiers, $K(C, t)$ is a matrix of turnover coefficients. Despite its advantages, a key challenge of the matrix-based formulation is the parameterization of the matrices A , B , and K , which requires detailed mechanistic assumptions or extensive calibration. Such parameterizations are often poorly constrained and exhibit high spatial heterogeneity, making it difficult to apply the model robustly under diverse environmental and management conditions.

Here, we further extend the matrix approach using neural ordinary differential equations (NODEs), where the right-hand side of ODEs is replaced by neural networks [1]. Specifically, we use a 3-layer MLP to parameterize the carbon allocation dynamics (the right-hand side of Eq. 11) implicitly based on carbon pool states and external inputs (i.e., NPP, LAI, leaf nitrogen, and soil moisture). This NODE-based formulation avoids explicitly prescribing the allocation, transfer, and turnover coefficients while introducing data-driven flexibility to better capture the complexity and variability of crop-environment interactions. Our choice of matrix approach was also motivated by our desire for efficient running on machine learning accelerators, in particular GPUs, which are highly optimized for matrix operations.

B.3 Soil and litter carbon cycle

Agricultural soil and litter carbon play a crucial role in the global carbon balance under climate change. In LPJmL, the litter carbon consists of three litter pools, including two above-ground leaf and stem litter carbon pools and one below-ground root litter carbon pool. The soil carbon is simulated across five vertical soil layers (0.2, 0.3, 0.5, 1, and 1 meter thickness) with a fast and a slow organic carbon pool in each layer [18]. LPJmL uses discrete-time balance equations to update each soil and litter carbon pool. Based on the matrix approach, we reformulated the soil and litter carbon balance as explicit ODEs (Eqs. 12 - 14), which are well suited for parallel execution on GPUs.

$$\frac{dC_{\text{litter}}(t, l)}{dt} = A_{\text{litter}} \cdot C_{\text{residue}} - (1 - \exp(-k_{\text{litter}10} \cdot f_{\text{litter}}(t, l))) \cdot C_{\text{litter}}(t, l), \quad (12)$$

with $l = 1, 2, 3$,

where C_{residue} denotes the crop residues after crops are harvested, A_{litter} is the crop residue partitioning coefficients, $k_{\text{litter}10}$ is the static litter carbon decomposition rate at 10 °C, $f_{\text{litter}}(t, l)$ is the carbon decomposition response function. Above-ground litter carbon decomposition depends on air temperature and soil moisture, whereas below-ground litter carbon decomposition depends on soil temperature and soil moisture. The second term of Eq. 12 is the daily decomposed litter carbon, at which 70% of decomposed litter carbon directly enters the atmosphere as litter respiration, and the remaining goes into the soil carbon pools, with 98.5% to the fast soil carbon pools and 1.5% to the slow carbon pools [18].

$$\frac{dC_{\text{fast}}(t, l)}{dt} = A_{\text{fast}}\mu(t) - (1 - \exp(-k_{\text{fast}10} \cdot f_{\text{fast}}(t, l))) \cdot C_{\text{fast}}(t, l), \quad (13)$$

$$\frac{dC_{\text{slow}}(t, l)}{dt} = A_{\text{slow}}\mu(t) - (1 - \exp(-k_{\text{slow}10} \cdot f_{\text{slow}}(t, l))) \cdot C_{\text{slow}}(t, l), \quad (14)$$

with $l = 1, 2, 3, 4, 5$,

where $\mu(t)$ is the carbon input from decomposed litter carbon, A_{fast} and A_{slow} are the carbon input partitioning coefficients across five layers, $k_{\text{fast}10}$ and $k_{\text{slow}10}$ are the static soil carbon decomposition rate at 10 °C, $f_{\text{fast}}(t, l)$ and $f_{\text{slow}}(t, l)$ are the carbon decomposition response functions which depends on soil temperature and soil moisture. Both the second term of Eq. 13 and Eq. 14 are the daily decomposed soil carbon, which directly goes into the atmosphere as soil respiration.

The original formulation of the response function is a cubic polynomial equation:

$$f = \exp \left[308.56 \cdot \left(\frac{1}{56.02} - \frac{1}{T + 46.02} \right) \right] \cdot (0.0402 - 5.005 \cdot \theta^3 + 4.269 \cdot \theta^2 + 0.719 \cdot \theta), \quad (15)$$

where (T) denotes air or soil temperature, θ is soil moisture. We replace the decomposition response functions $f_{\text{litter}}(t, l)$, $f_{\text{fast}}(t, l)$, and $f_{\text{slow}}(t, l)$ in Eqs. 12 - 14 with a

3-layer MLP that takes both soil temperature and soil moisture as inputs, respectively. This allows the model to flexibly capture nonlinear environmental effects in a fully data-driven manner, rather than relying on fixed cubic polynomial response functions.

B.4 Soil and litter nitrogen cycle

In LPJmL, the soil and litter nitrogen cycle is tightly coupled to the soil and litter carbon cycle and follows a structurally similar formulation, including three litter nitrogen pools and a fast and a slow nitrogen pool in each soil layer [19]. We also reformulated the soil and litter nitrogen balance as explicit ODEs (Eqs. 16-18).

$$\frac{dN_{\text{litter}}(t, l)}{dt} = A_{\text{litter}} \cdot N_{\text{residue}} - (1 - \exp(-k_{\text{litter}10} \cdot f_{\text{litter}}(t, l))) \cdot N_{\text{litter}}(t, l), \quad (16)$$

with $l = 1, 2, 3$,

where N_{residue} denotes the crop residues after crops are harvested, A_{litter} is the crop residue partitioning coefficients, $k_{\text{litter}10}$ is the static litter nitrogen decomposition rate at 10 °C, $f_{\text{litter}}(t, l)$ is the nitrogen decomposition response function. Above-ground litter nitrogen decomposition depends on air temperature and soil moisture, whereas below-ground litter nitrogen decomposition depends on soil temperature and soil moisture. The second term of Eq. 16 is the daily decomposed litter nitrogen, at which 70% of decomposed litter nitrogen directly enters the atmosphere as litter respiration, and the remaining goes into the soil nitrogen pools, with 98.5% to the fast soil nitrogen pools and 1.5% to the slow nitrogen pools [18].

$$\frac{dN_{\text{fast}}(t, l)}{dt} = A_{\text{fast}}\mu(t) - (1 - \exp(-k_{\text{fast}10} \cdot f_{\text{fast}}(t, l))) \cdot N_{\text{fast}}(t, l), \quad (17)$$

$$\frac{dN_{\text{slow}}(t, l)}{dt} = A_{\text{slow}}\mu(t) - (1 - \exp(-k_{\text{slow}10} \cdot f_{\text{slow}}(t, l))) \cdot N_{\text{slow}}(t, l), \quad (18)$$

with $l = 1, 2, 3, 4, 5$,

where $\mu(t)$ is the nitrogen input from decomposed litter nitrogen, A_{fast} and A_{slow} are the nitrogen input partitioning coefficients across five layers, $k_{\text{fast}10}$ and $k_{\text{slow}10}$ are the static soil nitrogen decomposition rate at 10 °C, $f_{\text{fast}}(t, l)$ and $f_{\text{slow}}(t, l)$ are the nitrogen decomposition response functions which depends on soil temperature and soil moisture. Both the second term of Eq. 17 and Eq. 18 are the daily decomposed soil nitrogen, which directly goes into the atmosphere as soil respiration.

The original formulation of the response function follows Eq. 15. We replace the decomposition response functions $f_{\text{litter}}(t, l)$, $f_{\text{fast}}(t, l)$, and $f_{\text{slow}}(t, l)$ in Eqs. 16 - 18 with a 3-layer MLP that takes both soil temperature and soil moisture as inputs, respectively. This allows the model to flexibly capture nonlinear environmental effects in a fully data-driven manner, rather than relying on fixed cubic polynomial response functions.

B.5 Soil water cycle

Similar to soil carbon and nitrogen, soil water in LPJmL is represented by five hydrologically active layers. Rather than explicitly solving the governing partial differential equations [10, 20], LPJmL simulates daily soil-water dynamics with a computationally efficient bucket model as follows:

$$W_t = W_{t-1} + \Delta t [(P + M + Irr - E_I) - R - (E_S + E_T) - p], \quad (19)$$

where W is the absolute soil water content in a specific soil layer, P is the precipitation, M is the snowmelt, Irr is the irrigation water, E_I is the interception loss from leaves, R is the runoff, E_S is the soil evaporation, E_T is the plant transpiration, and p is the percolation. The Δt is the model time step, which is fixed to one day in LPJmL so that all flux terms are expressed as daily rates. LPJmL assumes that E_S occurs only in bare soil with vegetation cover less than 100% and that water required for evaporation is available from the top 0.3 meters of soil. The soil water accessible for E_T depends on the root depth of vegetation. The structure of Eq. 19 is inherently discrete but equivalent to an explicit first-order ODE for a fixed time step. We reformulated it as a first-order ODE (Eq. 20), which allows the use of differentiable ODE solvers, enabling efficient gradient-based optimization for ML models.

$$\frac{dW}{dt} = (P + M + Irr - E_I) - R - (E_S + E_T) - p. \quad (20)$$

Compared to the soil carbon cycle, the soil water cycle is inherently more complex, involving a broader range of interacting processes, which leads to significantly higher uncertainty in predictions. Although the ODE-based soil water representation (Eq. 20) is numerically tractable, it relies on empirical formulas and fixed parameters. Such simplifications limit its ability to capture the complex spatio-temporal nonlinear processes, especially under diverse land cover types, soil properties, and climatic conditions.

To address the above limitations of Eq. 20, we integrate neural networks with soil water processes to augment the traditional process-based formulation with data-driven flexibility. We could use neural networks to replace the entire right-hand side of Eq. 20 to get a fully data-driven soil water representation, or replace only specific sub-processes to get a hybrid model. To compare both approaches, we implement a 3-layer MLP to replace M and E_S leading to a hybrid model, and a 3-layer MLP to fully emulate the daily soil water dynamics, respectively. The reason to replace M and E_S was based purely on empirical evidence. Through extensive testing, we found that replacing these two sub-processes yielded the most stable long-term simulations, whereas replacing other or additional sub-processes often led to simulation instability due to weakened sub-process constraints. Moreover, M involves a complex heuristic snowmelt formulation, and using a neural network to emulate it can substantially reduce model complexity. These two models were trained using mean squared error as the training objective. Results indicate that the hybrid approach better captures the daily dynamics of soil water content both in-sample and out-of-sample scenarios than

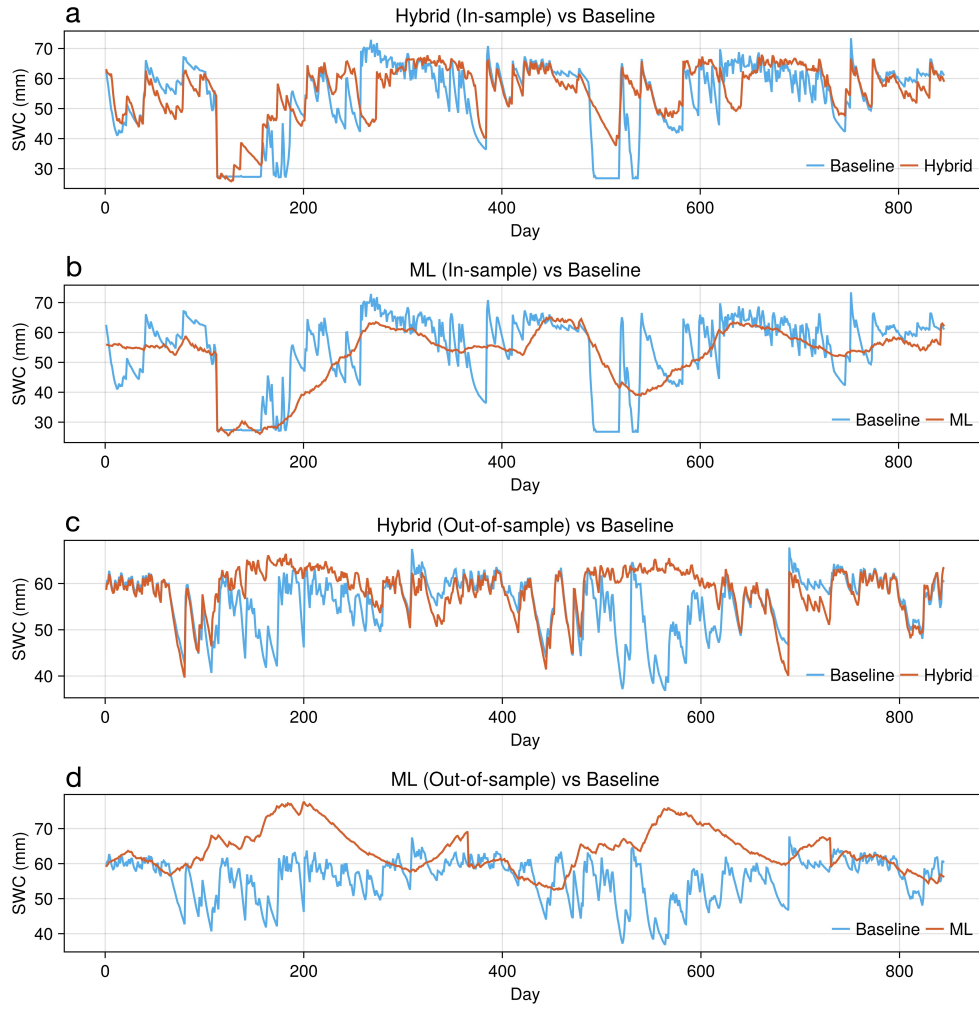


Fig. S2 Comparison of soil water content (SWC) simulated by hybrid and pure machine learning models under in-sample and out-of-sample scenarios, with LPJmL-simulated SWC used as baseline. Panels a and b show in-sample performance for the hybrid and pure machine learning models, respectively, while panels c and d present their out-of-sample performance.

the fully data-driven alternative, as shown in Fig. S2. Due to the physical constraints of process-based components, the hybrid model more accurately captures rapid fluctuations in SWC and maintains consistency with the baseline across both in-sample and out-of-sample scenarios (Fig. S2, panels a and c), whereas the pure machine learning model exhibits overly smoothed responses and shows pronounced deviations from the baseline (Fig. S2, panels b and d), especially under out-of-sample scenarios. This indicates that incorporating process-based components with ML methods provides a more accurate and generalizable representation of soil hydrological processes.

C Data

C.1 Initial conditions

Before simulating managed croplands, process-based vegetation models usually need spin-up simulations to develop equilibrium vegetation and soil states. LPJmL involves a two-stage spin-up process. The first spin-up simulation typically runs for 5000 years until all system states (i.e., soil carbon, nitrogen, and water pools) reach equilibrium. The second spin-up simulation typically spans 390 years to introduce the impacts of land-use change on these pools driven by historical human activities [21]. Since NeuralCrop does not simulate natural vegetation, it can not perform this spin-up procedure prior to crops simulations. We therefore perform the spin-up in LPJmL and initialize the soil carbon, nitrogen, and water pools in NeuralCrop from LPJmL simulations to ensure physically consistent initial conditions.

C.2 Pre-training data

Due to the limited availability of large-scale high-resolution observations for cropland carbon, water, and nitrogen dynamics, NeuralCrop is pre-trained on simulation data (Table S1) generated by LPJmL. This pre-training step allows NeuralCrop to learn prior knowledge from LPJmL and provides a strong initialization for subsequent training under data-scarce conditions. The LPJmL inputs are shown in Table S2.

Table S1 Training data generated by LPJmL.

Variable	Symbol	Dimension	Units	Time
Inter-cellular to atmospheric CO ₂ ratio	λ	1	-	daily
Maximum Rubisco capacity	V_{\max}	1	g C m^{-2}	daily
Gross primary productivity	GPP	1	g C m^{-2}	daily
Crop carbon pools	C_i	4	g C m^{-2}	daily
Litter carbon pools	$C_{\text{litter}(1)}$	3	g C m^{-2}	daily
Soil fast carbon pools	$C_{\text{fast}(1)}$	5	g C m^{-2}	daily
Soil slow carbon pools	$C_{\text{slow}(1)}$	5	g C m^{-2}	daily
Litter nitrogen pools	$N_{\text{litter}(1)}$	3	g N m^{-2}	daily
Soil fast nitrogen pools	$N_{\text{fast}(1)}$	5	g N m^{-2}	daily
Soil slow nitrogen pools	$N_{\text{slow}(1)}$	5	g N m^{-2}	daily
Soil water pools	$W_{(1)}$	5	mm	daily

C.3 Fine-tuning data

During the fine-tuning stage, the training of NeuralCrop is focused on optimizing the ML components with real-world observations. The fine-tuning data were obtained from the global flux network FLUXNET, the American flux network AmeriFlux, and the European Integrated Carbon Observation System (ICOS), which provide site-level daily crop and soil eddy covariance flux as well as meteorological forcing measurements. Table S3 shows the observational data used during the fine-tuning stage. After the

Table S2 LPJmL inputs.

Type	Variable	Units	Time
Climate	Temperature	$^{\circ}\text{C}$	daily
Climate	Maximum temperature	$^{\circ}\text{C}$	daily
Climate	Minimum temperature	$^{\circ}\text{C}$	daily
Climate	Precipitation	mm	daily
Climate	Net longwave radiation	W/m^2	daily
Climate	Downward shortwave radiation	W/m^2	daily
Climate	Wind speed	m min^{-1}	daily
Climate	CO_2	ppmv	annual
Soil	Soil texture	-	static
Soil	Soil PH	-	static
Management	Land use	-	annual
Management	Nitrogen fertilizer	g N m^{-2}	annual
Management	Tillage	-	annual
Management	Residue on field	-	annual
Management	Sowing date	-	static
Management	Heat unit requirements	-	static
Coordinate	Land sea mask	$^{\circ}\text{C}$	static

pre-training stage, NeuralCrop is able to reproduce the dynamics of LPJmL, but also inherits its structural and knowledge biases. To address that, we optimize the parameters of the relevant ML components of NeuralCrop using data from flux networks, while freezing the remaining ML components.

Table S3 Flux network observational data.

Type	Variable	Symbol	Units	Time
Feature	Air temperature	TA_{F}	$^{\circ}\text{C}$	daily
Feature	Precipitation	P_{F}	mm	daily
Feature	Downward shortwave radiation	$\text{SW}_{\text{IN}_\text{F}}$	W/m^2	daily
Feature	Downward longwave radiation	$\text{LW}_{\text{IN}_\text{F}}$	W/m^2	daily
Feature	Upward longwave radiation	LW_{OUT}	W/m^2	daily
Feature	CO_2	$\text{CO2}_{\text{F_MDS}}$	$\mu\text{mol mol}^{-1}$	daily
Label	Gross primary productivity	$\text{GPP}_{\text{NT_VUT_REF}}$	g C m^{-2}	daily
Label	Ecosystem Respiration	$\text{RECO}_{\text{NT_VUT_REF}}$	g C m^{-2}	daily
Label	Soil water content,	$\text{SWC}_{\text{F_MDS-}\#}$	%	daily

denotes soil depth index, higher values represent deeper layers (1 is the shallowest).

C.4 Data pre-processing

The flux networks provide both daytime and nighttime partitioned GPP and RECO [22, 23]. The nighttime method estimates RECO by fitting a respiration-temperature function using nighttime data and derives GPP as the difference between modeled RECO and daytime net ecosystem exchange (NEE). Because photosynthesis is negligible at night, RECO is approximately equal to NEE. The daytime method

fits a light-response function to estimate GPP and a respiration-temperature function for RECO using daytime and nighttime data. As a result, both GPP and RECO are estimated by NEE, which introduces coupled uncertainties. Therefore, we use nighttime partitioned GPP and RECO for fine-tuning. The nighttime partitioned GPP and RECO may contain negative values. We replace negative GPP and RECO with their daytime counterparts to avoid introducing an additional bias during fine-tuning.

The soil water content across flux tower sites is not standardized in the number of soil layers and their depth, which poses a challenge for consistent model training. To address this, we converted the soil water distribution into the five-layer structure used in NeuralCrop by aggregating or interpolating soil water data based on depth-weighted proportions aligned with the relative thicknesses of the NeuralCrop soil layers.

D Training

D.1 Input data normalization

All input features are standardized before being joined together and passed to the neural networks. We normalize climate forcings distributed with zero mean and unit variance to improve training stability. Specifically, for each climate forcing variable x , we compute the standardized value \tilde{x} as:

$$\tilde{x} = \frac{x - \mu}{\sigma}, \quad (21)$$

where μ is the mean and σ is the standard deviation computed from the 20-year historical climatology. For input features generated by NeuralCrop itself, we rescale them to the $[0, 1]$ range using their physical upper and lower bounds. Here, for each state variable x , the normalized value \tilde{x} is computed as:

$$\tilde{x} = \frac{x - x_{\text{lower}}}{x_{\text{upper}} - x_{\text{lower}}}, \quad (22)$$

where x_{lower} and x_{upper} denote the physical lower and upper limits of the variable, respectively.

D.2 Optimizer settings

All NeuralCrop models were pre-trained using the AdamW optimizer [24]. We used values $\beta_1 = 0.9$, $\beta_2 = 0.999$, and $\epsilon = 10^{-6}$ based on empirical evidence from prior experiments. The initial learning rate was set to 1×10^{-3} . A sinusoidal exponential decay scheme (SinExp) was employed to dynamically adjust the learning rate throughout training, oscillating between 1×10^{-3} and 1×10^{-5} with a decay factor of 0.975 and a cycle period of 20 epochs. The only exception to these hyperparameters in fine-tuning was that the initial learning rate was set to 1×10^{-4} . All models were trained for 100 epochs using batch sizes 32, 64, 128, 256. We empirically selected the configuration that produced the most stable decrease in validation loss over time.

D.3 Loss function

All NeuralCrop models are trained in two stages (pre-training and fine-tuning) with different loss functions, where all loss terms are defined in the general form of mean squared error (MSE):

$$\text{MSE} = \frac{1}{T} \sum_{t=1}^T (\hat{y}_t - y_t)^2, \quad (23)$$

where \hat{y}_t is the model simulation at time t , y_t is the corresponding observation, and T is the total number of time steps.

During the pre-training stage, we employed a combination of two loss types (i.e., accuracy and mass balance) to minimize two kinds of discrepancies between NeuralCrop and LPJmL outputs. The loss term of accuracy accounts for the distance between predictions and reference data, and the loss term of mass balance constrains the carbon conservation during crop carbon allocation. The pre-training loss function with two kinds of loss types:

$$\mathcal{L}_{\text{Pre-training}} = \sum_{i \in \mathcal{T}} \beta_{\text{accuracy},i} \mathcal{M}_{\text{Accuracy},i} + \beta_{\text{mass}} \mathcal{M}_{\text{MassBalance}}, \quad (24)$$

where \mathcal{T} denotes the set of loss terms of accuracy (i.e., λ , V_{max} , GPP, carbon and nitrogen pools, soil water pools), $\mathcal{M}_{\text{Accuracy},i}$ is the MSE between NeuralCrop prediction and reference data of variable i with corresponding loss scales $\beta_{\text{accuracy},i}$, $\mathcal{M}_{\text{MassBalance}}$ is the MSE between the sum of crop carbon and accumulated above-ground biomass with a loss scale β_{mass} .

After the pre-training stage, NeuralCrop was further fine-tuned with real-world observational data (i.e., the eddy-covariance flux data) to reduce the gap between model outputs and ground truth. During this stage, we only updated the ML components that correspond to variables with available observations (C.3). Here is the loss function:

$$\mathcal{L}_{\text{Fine-tuning}} = \beta_{\text{gpp}} \mathcal{M}_{\text{GPP}} + \beta_{\text{reco}} \mathcal{M}_{\text{RECO}} + \beta_{\text{swc}} \mathcal{M}_{\text{SWC}}, \quad (25)$$

where \mathcal{M}_{GPP} , $\mathcal{M}_{\text{RECO}}$, and \mathcal{M}_{SWC} denote the MSE on GPP, RECO, and SWC, scaled by β_{gpp} , β_{reco} , and β_{swc} , respectively.

D.4 Training sequence length

To investigate the required length of time series data for effective training, we trained several NeuralCrop models with identical parameters using time series data ranging from 1 to 20 years in length. We find that two years of data were sufficient to train NeuralCrop effectively. We further investigated two training strategies. The first strategy used 80% of the time series samples from two years for training and the remaining 20% for validation. The second strategy used the time series samples from the first two years for training, with the third year for validation. We found that both strategies yielded comparable performance.

D.5 Training rollouts

To explore the benefits of training with different rollouts (i.e., how many simulation days to update ML parameters), we trained the NeuralCrop models with identical model parameters on rollouts of 1, 30, 60, 180, 365, and 720 days (Fig. S3). We find that NeuralCrop trained on longer rollouts leads to significantly more stable convergence during training. In contrast, NeuralCrop trained on shorter rollouts, especially 1 day, exhibits large oscillations in both training and validation loss during the entire training period. The rollout of 365 days leads to the most stable and smooth convergence.

We attribute this to the fact that a 365-day rollout covers the complete crop growth cycle, which enables ML components to learn complete seasonal dynamics in a single rollout. Although the rollout of 720 days also exhibits similarly stable convergence, the longer sequence length results in deeper computational graphs, increasing both memory usage and time costs of backpropagation. Therefore, we set a 365-day rollout as the default to train all NeuralCrop models.

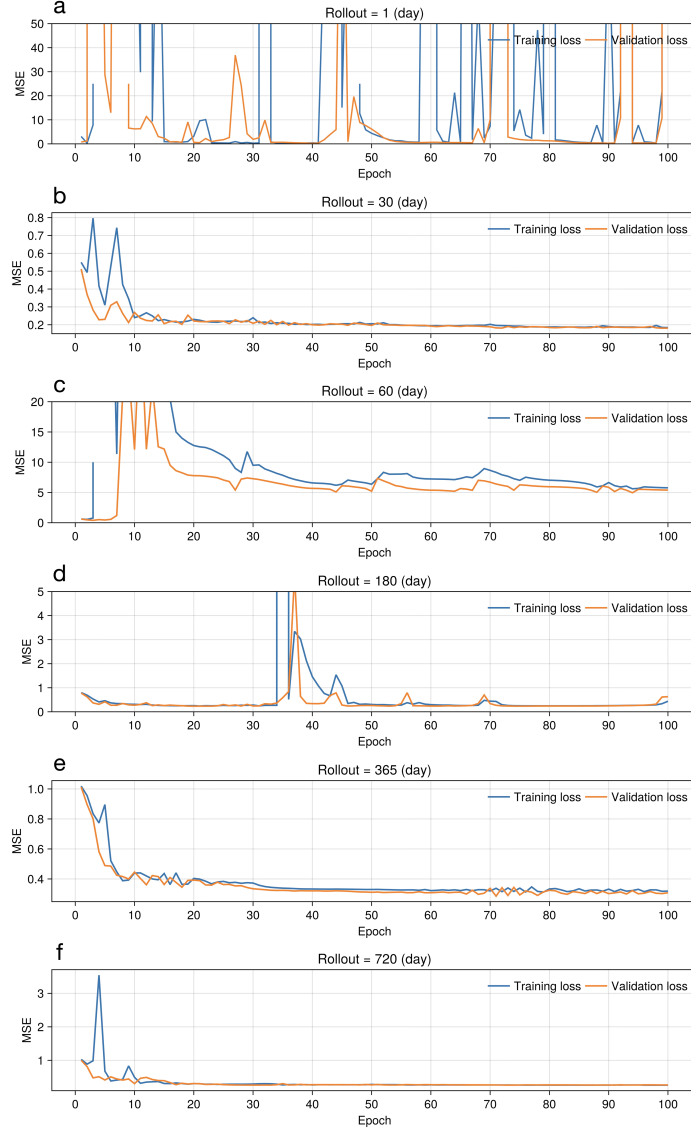


Fig. S3 NeuralCrop models with identical model parameters trained on rollouts of 1, 30, 60, 180, 365, and 720 days (a-f).

D.6 Output rescaling

All variables predicted by neural networks during training are rescaled using their historical minimum and maximum values over the training years, which prevents variables with large magnitudes from dominating the training. Specifically, for each predicted variable x , the normalized value \tilde{x} is computed as:

$$\tilde{x} = \frac{x - x_{\min}}{x_{\max} - x_{\min}}, \quad (26)$$

where x_{\min} and x_{\max} denote the minimum and maximum values of the variable, respectively.

D.7 Training resources

All training and inference of NeuralCrop were conducted using a single NVIDIA H100 GPU with 80GB of memory.

We compared the efficiency of inference time between GPU-accelerated NeuralCrop and CPU-based LPJmL by running them on a $0.5^\circ \times 0.5^\circ$ spatial resolution with daily time steps over a 20-year simulation period (7300 days) at different grid cells (Table S4). The LPJmL was running on one single AMD EPYC 9554 CPU with 128 cores and 768GB of memory. The results show that LPJmL takes over 7,500 seconds (about 2 hours) to simulate 14,157 grid cells, whereas NeuralCrop completes the exact simulation in 91 seconds, over 82 times faster. Similar gains appear at smaller grid cells, with 60 times faster for 7,865 grid cells and 16 times faster for 1,573 grid cells. Although GPU overhead makes the one-cell simulation slower, the efficiency increases rapidly with scale, reflecting the powerful parallel capacity of the GPU. This allows NeuralCrop to achieve competitive speed compared to traditional GGCM running on multiple CPU cores when doing global and daily simulations.

It is not entirely fair to directly compare the inference time between GPU-accelerated NeuralCrop and CPU-based LPJmL. CPUs can also do parallel computing with more cores through MPI (Message Passing Interface). Moreover, other factors such as power consumption and hardware cost, need to be considered when evaluating the overall efficiency. However, we can already see the substantial advantage of developing next-generation, GPU-based crop models by comparing the performance of a single GPU to multiple CPU cores.

Table S4 Inference time of GPU-accelerated NeuralCrop and CPU-based LPJmL simulating for a $0.5^\circ \times 0.5^\circ$ spatial resolution with daily time steps over a 20-year simulation period (7300 days) at different grid cells. NeuralCrop was running on one single NVIDIA H100 GPU with 80GB of memory, and LPJmL was running on one single AMD EPYC 9554 CPU with 128 cores and 768GB of memory.

Grid cells	LPJmL	NeuralCrop	Times (speed up)
1	0.50 s	46.01 s	0.011x
1573	833.99 s	51.24 s	16.27x
7865	4169.94 s	70.02 s	59.55x
14157	7505.89 s	91.16 s	82.33x

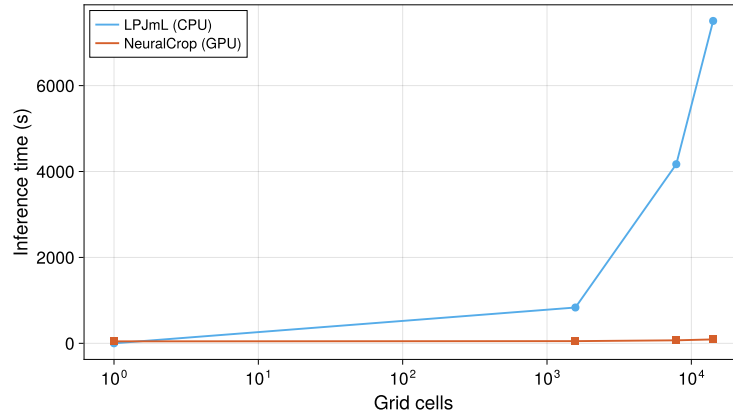


Fig. S4 Inference time of GPU-accelerated NeuralCrop and CPU-based LPJmL simulating for a $0.5^\circ \times 0.5^\circ$ spatial resolution with daily time steps over a 20-year simulation period (7300 days) at different grid cells. NeuralCrop was running on one single NVIDIA H100 GPU with 80GB of memory, and LPJmL was running on one single AMD EPYC 9554 CPU with 128 cores and 768GB of memory.

E Evaluation metrics

Evaluation metrics compare model simulations with ground truth. In this study, our preferred evaluation metrics include root mean square error (RMSE) and Pearson correlation coefficient (r).

E.1 Pearson correlation coefficient

Pearson correlation coefficient (r) calculates the linear relationship between model simulations and observations. It is defined as:

$$r = \frac{\sum_{t=1}^T (y_t - \bar{y})(\hat{y}_t - \bar{\hat{y}})}{\sqrt{\sum_{t=1}^T (y_t - \bar{y})^2} \sqrt{\sum_{t=1}^T (\hat{y}_t - \bar{\hat{y}})^2}}, \quad (27)$$

where \hat{y}_t and y_t represent the simulated and observed values at time t , respectively, while $\bar{\hat{y}}$ and \bar{y} denote their mean values. It ranges from -1 to $+1$, with higher values indicating stronger agreement in the temporal variability. In particular, r is used to assess the ability of models to reproduce seasonal and interannual variations.

E.2 Spearman correlation coefficient

Spearman correlation coefficient (ρ) calculates the monotonic relationship between model simulations and observations, based on the ranked values of the data. It is defined as:

$$\rho = 1 - \frac{6 \sum_{t=1}^T d_t^2}{T(T^2 - 1)}, \quad (28)$$

where d_t is the difference between the ranks of the observed value y_t and the simulated value \hat{y}_t at time t , and T is the total number of samples. Alternatively, ρ can be expressed as the Pearson correlation between the ranked variables:

$$\rho = \frac{\text{cov}(\text{rank}(Y), \text{rank}(\hat{Y}))}{\sigma_{\text{rank}(Y)} \sigma_{\text{rank}(\hat{Y})}}. \quad (29)$$

It ranges from -1 to $+1$, with higher values indicating stronger agreement in the relative ordering of the two time series. In particular, ρ is used to assess the ability of models to reproduce the temporal variability or spatial distribution of observed data, independent of absolute magnitudes.

E.3 Root mean square error

Root mean square error (RMSE) is a widely used metric to evaluate the accuracy of model predictions against observations. It is defined as the square root of the average

of the squared differences between predicted values and observed values:

$$RMSE = \sqrt{\frac{1}{T} \sum_{t=1}^T (\hat{y}_t - y_t)^2}, \quad (30)$$

where \hat{y}_t is the model simulation at time t , y_t is the corresponding observation, and T is the total number of time steps. A lower RMSE value indicates better agreement between model simulations and observations.

F In situ validation

F.1 In situ sites

To evaluate the performance of NeuralCrop across different crop types and environments, we conducted in situ validation using observational data from four crop flux tower sites (Table S5 and Fig. S5), selected to represent wheat, rice, corn, and soybean cropping regions. These are four global staple crops, spanning diverse climate zones, management practices, and phenological patterns, making them suitable cases for evaluating the performance of NeuralCrop. Each site provides high-quality daily eddy covariance measurements of carbon (i.e., GPP, RECO, and NEE) and soil water fluxes (SWC), as well as measurements of meteorological variables (Table S3).

Table S5 Overview of crop flux tower sites used for NeuralCrop validation.

Site	Crop	Country	(latitude, longitude)	Year	Source
CH-Oe2 [25]	Wheat	Swiss	(47.2864, 7.7337)	2004-2023	ICOS
KR-CRK [26]	Rice	South Korea	(38.2013, 127.2506)	2005-2018	FLUXNET
US-Mo3 [27]	Soybean	USA	(39.2322, -92.1493)	2016-2021	AmeriFlux
US-Ne1 [28]	Corn	USA	(39.2322, -92.1493)	2001-2020	AmeriFlux

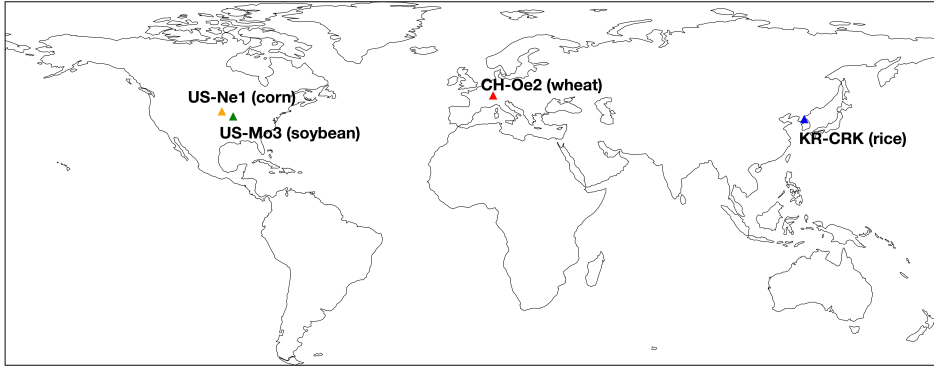


Fig. S5 Geographical locations of the four FLUXNET sites used for in situ validation of NeuralCrop. Each site corresponds to a different crop: wheat (CH-Oe2), rice (KR-CRK), corn (US-Ne1), and soybean (US-Mo3).

F.2 Training

We first train four NeuralCrop models for the above four crop sites separately using LPJmL outputs spanning from 2004 to 2017. Each NeuralCrop model is then fine-tuned with corresponding observational data (i.e., GPP, RECO, NEE, and SWC). The training setup can be found in Section C and Section D. Since crop rotation is practiced at these sites, we excluded flux data from non-target crop years and retained

only the data of periods during which the target crop was growing. We use the last year of data for validation and the remaining years for training (or fine-tuning). To evaluate the model performance, we use the root mean square error (RMSE, Eq. 30) and the Pearson correlation coefficient (r , Eq. 27) to assess both the accuracy and the ability of models to reproduce seasonal and interannual variations.

F.3 Results

We compare the daily predictions of GPP, RECO, NEE, and SWC from NeuralCrop and LPJmL against FLUXNET observations across all four crop sites. Results indicate that NeuralCrop models outperform LPJmL models (see Figs. S6-S8 and Table S6). For GPP, NeuralCrop consistently achieves lower RMSE values (1.38–1.62) compared to LPJmL (2.06–2.85), with correlations up to 0.98, indicating a more accurate reproduction of seasonal cycles and peak flux magnitudes. Similarly, for RECO, NeuralCrop significantly reduces RMSE (0.89–1.74) relative to LPJmL (1.36–2.57), and achieves higher correlations (0.79–0.97 vs. 0.68–0.95), demonstrating its improved capability to capture respiration dynamics. For NEE, NeuralCrop not only yields smaller errors (1.15–1.66 vs. 1.66–2.73 for LPJmL) but also stronger correlations (0.90–0.95 vs. 0.83–0.94), highlighting its ability to better capture the timing and magnitude of transitions between carbon sink and source. For SWC, NeuralCrop reduces RMSE (14.51–37.30) relative to LPJmL (14.90–37.68) at all sites, while correlations are site-dependent with NeuralCrop outperforming LPJmL at KR-CRK but showing slightly lower correlations at the other sites.

Overall, these results suggest that NeuralCrop performs well across diverse crop types and climatic zones, with consistently better performance in carbon flux simulations and comparable performance in soil water simulations compared to the traditional process-based crop model LPJmL. The improved performance of NeuralCrop highlights its potential as a reliable tool for assessing the impacts of climate change on crop productivity.

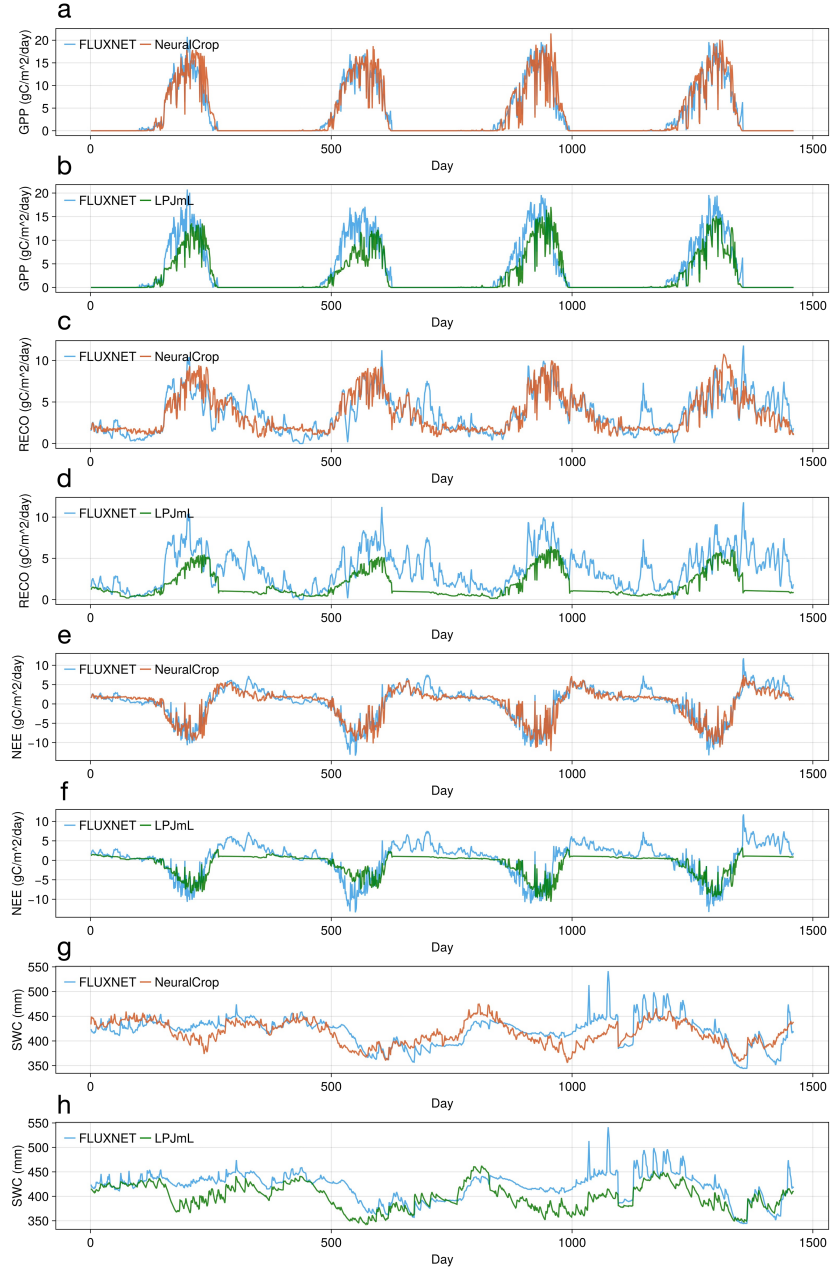


Fig. S6 Comparison between FLUXNET observations and model simulations (NeuralCrop and LPJmL) for the wheat site (CH-Oe2) over four years. Time series are shown for (a–b) gross primary productivity (GPP, $\text{gC m}^{-2} \text{day}^{-1}$), (c–d) ecosystem respiration (RECO, $\text{gC m}^{-2} \text{day}^{-1}$), (e–f) net ecosystem exchange (NEE, $\text{gC m}^{-2} \text{day}^{-1}$), and (g–h) soil water content (SWC, mm). Panels (a, c, e, g) compare FLUXNET with NeuralCrop, while panels (b, d, f, h) compare FLUXNET with LPJmL. Blue lines represent FLUXNET data, red lines represent NeuralCrop simulations, and green lines represent LPJmL simulations.

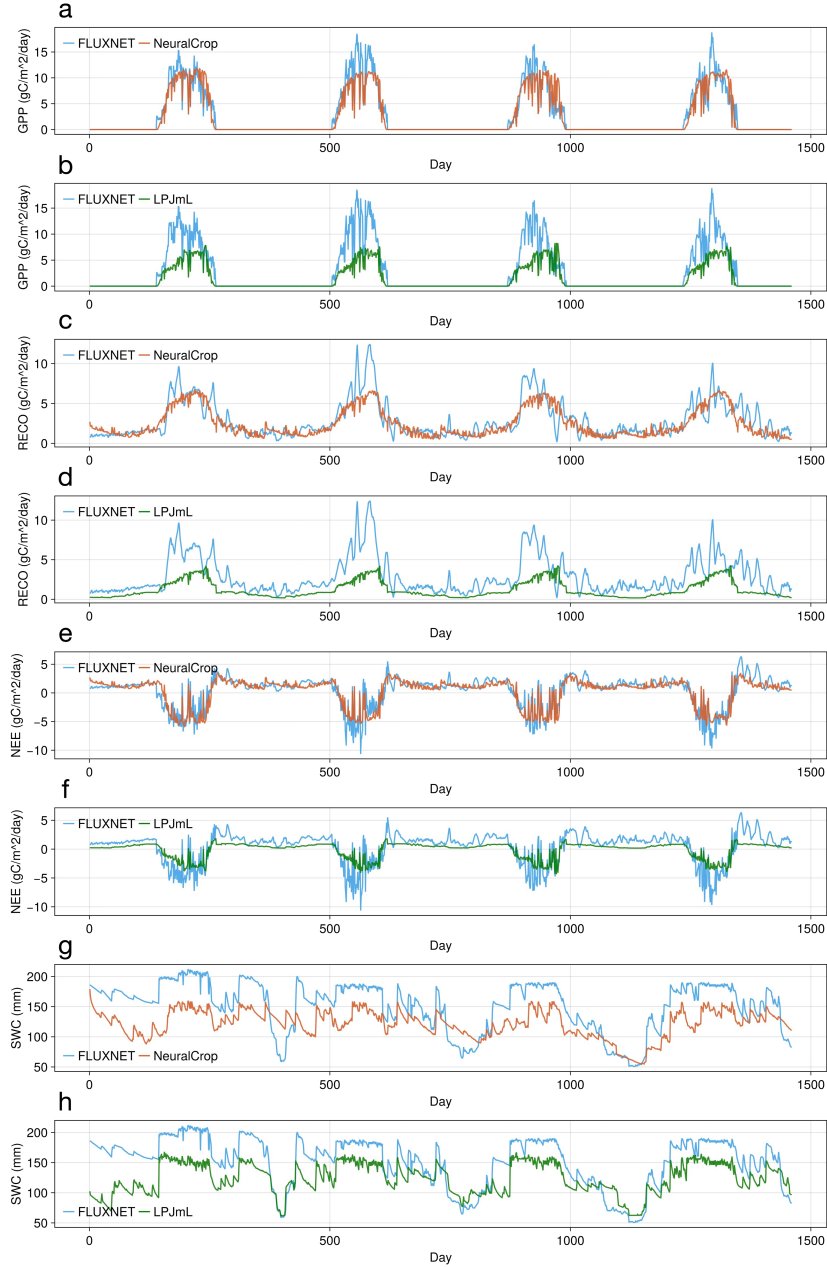


Fig. S7 Comparison between FLUXNET observations and model simulations (NeuralCrop and LPJmL) for the rice site (KR-CRK) over four years. Time series are shown for (a–b) gross primary productivity (GPP, gC m⁻² day⁻¹), (c–d) ecosystem respiration (RECO, gC m⁻² day⁻¹), (e–f) net ecosystem exchange (NEE, gC m⁻² day⁻¹), and (g–h) soil water content (SWC, mm). Panels (a, c, e, g) compare FLUXNET with NeuralCrop, while panels (b, d, f, h) compare FLUXNET with LPJmL. Blue lines represent FLUXNET data, red lines represent NeuralCrop simulations, and green lines represent LPJmL simulations.

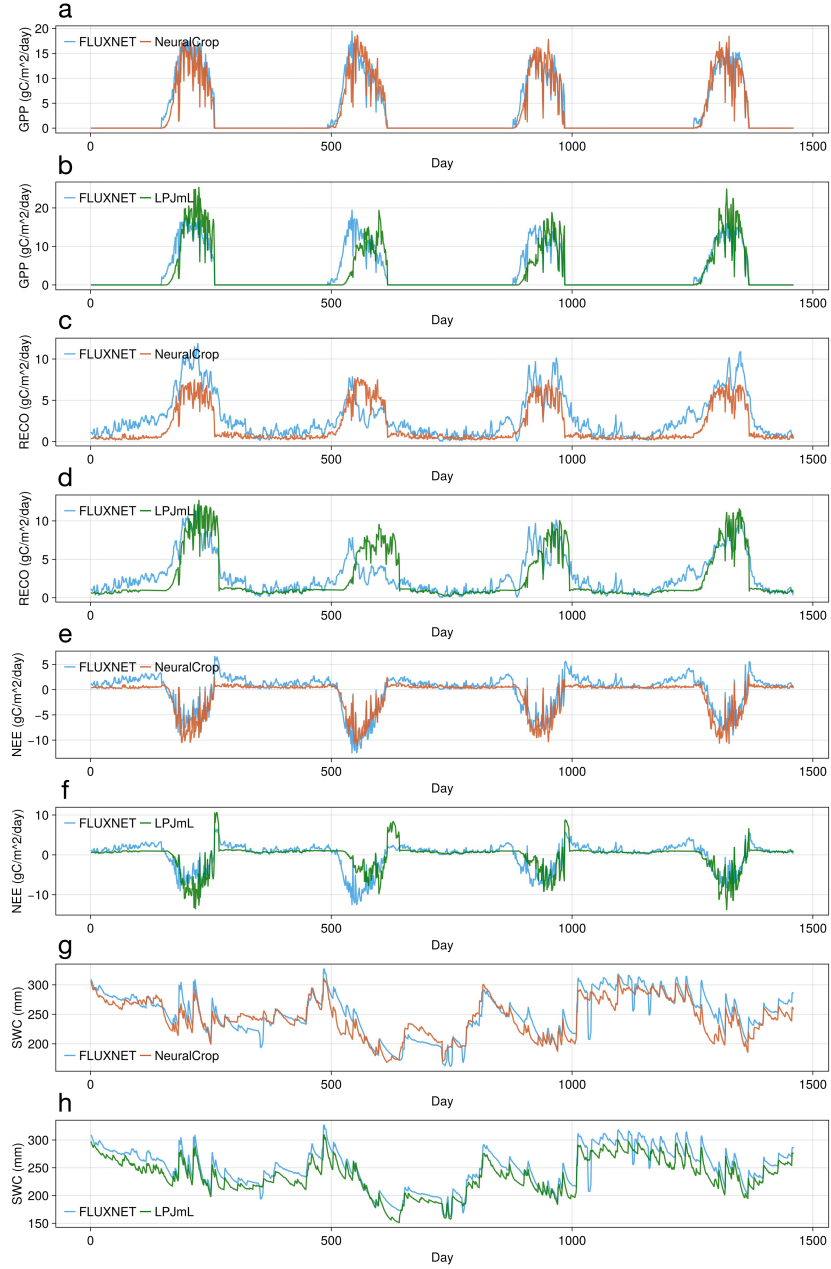


Fig. S8 Comparison between FLUXNET observations and model simulations (NeuralCrop and LPJmL) for the soybean site (US-Mo3) over four years. Time series are shown for (a–b) gross primary productivity (GPP, $\text{gC m}^{-2} \text{day}^{-1}$), (c–d) ecosystem respiration (RECO, $\text{gC m}^{-2} \text{day}^{-1}$), (e–f) net ecosystem exchange (NEE, $\text{gC m}^{-2} \text{day}^{-1}$), and (g–h) soil water content (SWC, mm). Panels (a, c, e, g) compare FLUXNET with NeuralCrop, while panels (b, d, f, h) compare FLUXNET with LPJmL. Blue lines represent FLUXNET data, red lines represent NeuralCrop simulations, and green lines represent LPJmL simulations.

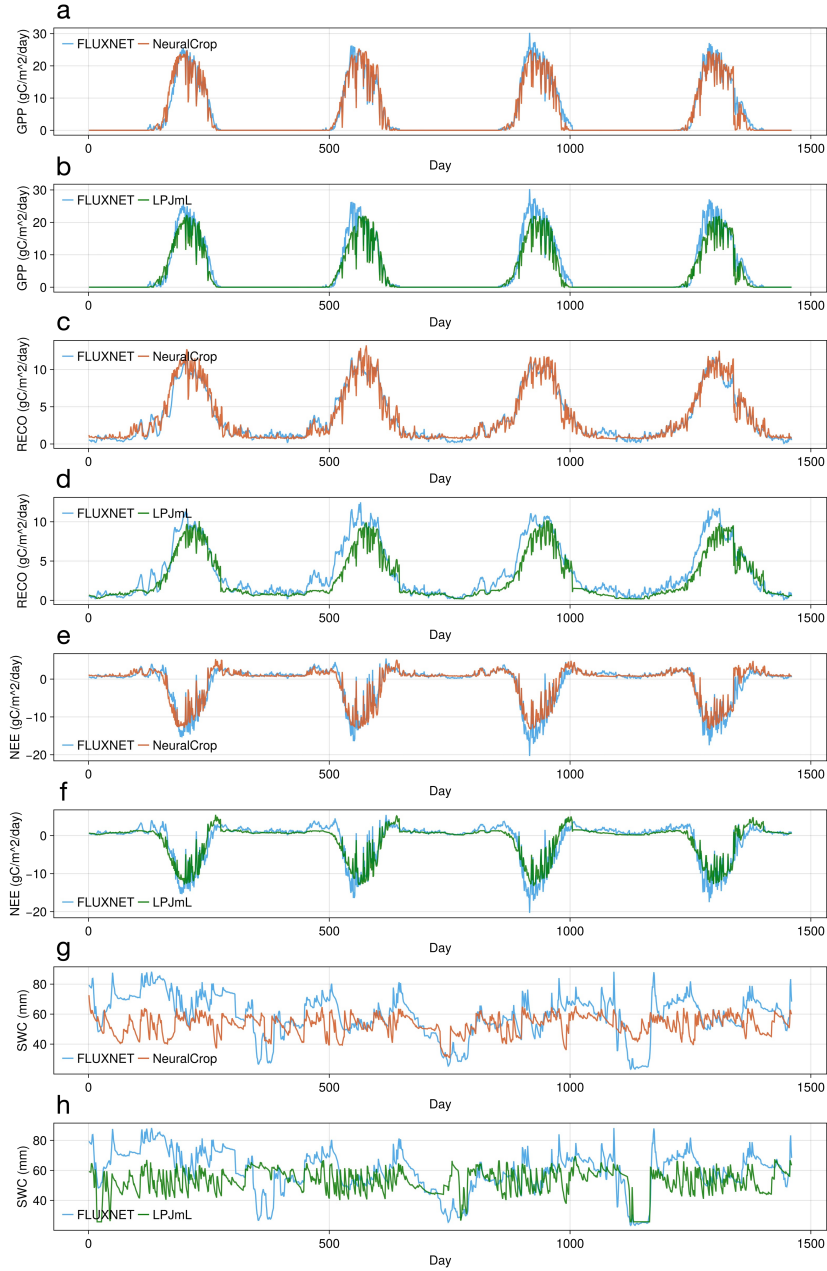


Fig. S9 Comparison between FLUXNET observations and model simulations (NeuralCrop and LPJmL) for the corn site (US-Ne1) over four years. Time series are shown for (a–b) gross primary productivity (GPP, $\text{gC m}^{-2} \text{day}^{-1}$), (c–d) ecosystem respiration (RECO, $\text{gC m}^{-2} \text{day}^{-1}$), (e–f) net ecosystem exchange (NEE, $\text{gC m}^{-2} \text{day}^{-1}$), and (g–h) soil water content (SWC, mm). Panels (a, c, e, g) compare FLUXNET with NeuralCrop, while panels (b, d, f, h) compare FLUXNET with LPJmL. Blue lines represent FLUXNET data, red lines represent NeuralCrop simulations, and green lines represent LPJmL simulations.

Table S6 Model performance against FLUXNET observations at four crop sites: CH-Oe2 (wheat), KR-CRK (rice), US-Mo3 (soybean), and US-Ne1 (corn). Performance metrics include Root Mean Square Error (RMSE) and Pearson correlation coefficient (r), calculated for gross primary productivity (GPP), ecosystem respiration (RECO), net ecosystem exchange (NEE), and soil water content (SWC). Bold numbers indicate the better performance between NeuralCrop and LPJmL.

Variable	Metric	Wheat (CH-Oe2)		Rice (KR-CRK)		Soybean (US-Mo3)		Corn (US-Ne1)	
		NeuralCrop	LPJmL	NeuralCrop	LPJmL	NeuralCrop	LPJmL	NeuralCrop	LPJmL
GPP	RMSE	1.53	2.51	1.42	2.83	1.38	2.85	1.62	2.06
	r	0.96	0.91	0.95	0.90	0.96	0.86	0.98	0.97
RECO	RMSE	1.51	2.57	1.37	2.37	1.74	1.82	0.89	1.36
	r	0.79	0.68	0.83	0.77	0.82	0.80	0.97	0.95
NEE	RMSE	1.66	2.73	1.15	1.68	1.57	2.28	1.53	1.66
	r	0.92	0.83	0.90	0.87	0.90	0.74	0.95	0.94
SWC	RMSE	22.21	30.58	37.30	37.68	17.55	17.88	14.51	14.90
	r	0.67	0.68	0.62	0.53	0.87	0.89	0.32	0.34

G Large-scale cropping regions

G.1 European wheat

G.1.1 Subnational crop statistics

We use the harmonized EU subnational crop statistics dataset [29] as ground truth, which was collected from National Statistical Institutes (NSIs) in EU countries and the EUROSTAT dataset. This dataset provides primarily county-level, and state-level in some EU countries, records of production, area, and yield in wheat, including soft, durum, and total wheat, across 27 EU countries over the period 1975–2020. We used the total wheat statistics from 2000 to 2019 for model evaluation, which includes 14,910 records for yield, covering a total of 883 regions (specifically, 3 NUTS-1, 69 NUTS-2, and 811 NUTS-3 statistical regions). In official statistics, wheat yields are reported at the standard EU humidity (14%). To ensure consistency with model simulations, all reported wheat yields are converted to dry matter (0% humidity) prior to analysis, as follows:

$$Y_{\text{DM}} = Y_{\text{HM}} \times (1 - h), \quad (31)$$

where Y_{DM} is the yield at 0% humidity, Y_{HM} is the yield at the standard humidity, and h is the standard humidity fraction.

G.1.2 Pre-training

In the European wheat cropping regions, we pre-trained NeuralCrop models using LPJmL outputs from 2016-1-1 to 2017-12-31 to simulate winter wheat varieties under rain-fed and irrigated management conditions, and outputs from 2016-1-1 to 2016-12-31 to simulate spring wheat varieties under rain-fed and irrigated management conditions, respectively. The initial states of the NeuralCrop models were derived from the LPJmL simulations on the last day of 2015, ensuring consistent soil water, carbon, and nitrogen conditions at the beginning of the training period. The training setup can be found in Section C and Section D.

To ensure the pre-trained NeuralCrop is adequately prepared for the subsequent fine-tuning phase, we compared simulated wheat yields from NeuralCrop and LPJmL for the period 2000-2019 at the subnational level. The simulated yields are aggregated to subnational units using an area-weighted average method, described in Section G.3. Fig. S10 shows that pre-trained NeuralCrop and LPJmL exhibit a strong agreement in their simulated wheat yields at the subnational level. The correlation coefficients are consistently high (mean values predominantly above 0.8) across all EU countries. This robust correlation confirms that the pre-trained NeuralCrop effectively learned and reproduced the wheat yield behavior of LPJmL.

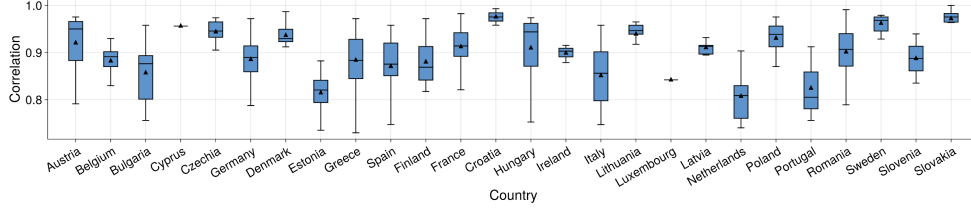


Fig. S10 Boxplots of time series correlation coefficient of simulated wheat yields between pre-trained NeuralCrop and LPJmL at the subnational level, aggregated by country for the period 2000–2019, with countries ordered alphabetically by their country code (A–Z). The box boundaries represent the interquartile range (IQR), defined by the first quartile, the median, and the third quartile. The upper and lower whiskers represent the maximum and minimum that are within 1.5 times the interquartile range of the box. The black triangles are the mean value.

G.1.3 Fine-tuning

NeuralCrop models were further fine-tuned using site-level eddy-covariance flux tower data across major European wheat cropping regions. The wheat flux data comprised 12 flux tower sites distributed in Belgium, Switzerland, Germany, France, and Italy (see Table S7 and Fig. S11), covering a broad range of climatic and management conditions. These observations provide daily GPP, RECO, NEE, and, for most sites, SWC, as well as auxiliary meteorological variables, spanning from 2001 to 2023. Since crop rotation is practiced at most sites, we excluded flux data from non-target crop years and retained only the data of periods during which the wheat was growing. The final dataset included a total of 76 site-years of wheat flux observations for fine-tuning.

Table S7 Overview of European wheat flux tower sites used for fine-tuning of NeuralCrop.

Site	Country	(latitude, longitude)	Year	Source
BE-Lon [30]	Belgium	(50.5516, 4.7462)	2004-2020	ICOS
CH-Oe2 [25]	Switzerland	(47.2864, 7.7337)	2004-2023	ICOS
DE-Geb [31]	Germany	(51.0997, 10.9146)	2001-2020	ICOS
DE-Kli [32]	Germany	(50.8930, 13.5223)	2004-2023	ICOS
DE-RuS [33]	Germany	(50.8659, 6.4471)	2011-2014	ICOS
DE-Seh [34]	Germany	(50.8706, 6.4497)	2001-2010	FLUXNET
DK-Vng [35]	Germany	(56.0374, 9.1607)	2009-2018	ICOS
FR-Gri [36]	France	(48.8442, 1.9519)	2004-2014	FLUXNET
FR-Aur [37]	France	(43.5496, 1.1061)	2005-2023	ICOS
FR-EM2 [38]	France	(49.8721, 3.0206)	2017-2023	ICOS
FR-Lam [39]	France	(43.4964, 1.2378)	2005-2020	ICOS
IT-CA2 [40]	Italy	(42.3772, 12.0260)	2011-2014	ICOS



Fig. S11 Geographical locations of the EU wheat flux tower sites used for fine-tuning of NeuralCrop.

G.2 US Corn Belt

G.2.1 County-level crop statistics

In this study, the US Corn Belt includes the states of South Dakota, Minnesota, Iowa, Missouri, Illinois, Indiana, Ohio, Michigan, and Wisconsin (shown in Fig. S12) [41]. County-level corn statistics from National Agricultural Statistics Service of USDA are used as ground truth, which provides records of production, area, and yield in corn, starting from 1910. We used the corn statistics from 2000 to 2019 for model evaluation, which includes 13,665 records for yield, covering a total of 764 counties. We also use the Eq. G.1.1, with $h = 0.155$, to convert the reported corn yields to dry matter (0% humidity) before analysis.

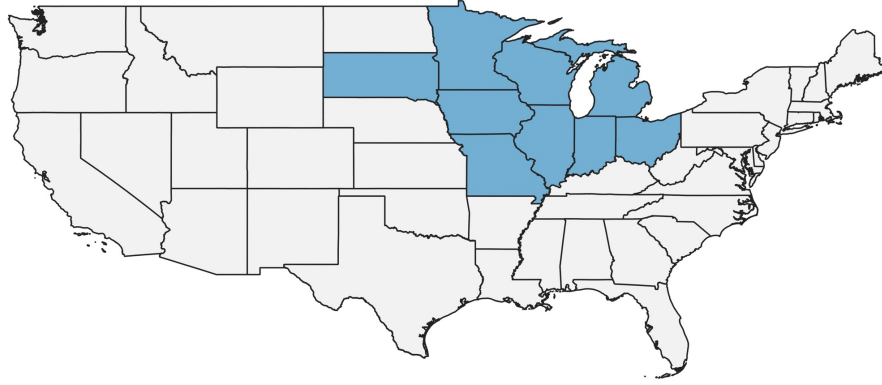


Fig. S12 States shaded in blue represent the US Corn Belt, including the states of South Dakota, Minnesota, Iowa, Missouri, Wisconsin, Illinois, Michigan, Indiana, and Ohio.

G.2.2 Pre-training

In the US Corn Belt cropping regions, we pre-trained NeuralCrop models using LPJmL outputs from 2016-1-1 to 2016-12-31 to simulate corn under rain-fed and irrigated management conditions, respectively. The initial states of the NeuralCrop models were derived from the LPJmL simulations on the last day of 2015, ensuring consistent soil water, carbon, and nitrogen conditions at the beginning of the training period. The training setup can be found in Section C and Section D.

Same to EU wheat pre-training, we compared simulated corn yields from NeuralCrop and LPJmL for the period 2000-2019 at the county level. The simulated yields are aggregated to counties using an area-weighted average method, described in G.3. Fig. S13 shows that pre-trained NeuralCrop and LPJmL exhibit a strong agreement in their simulated corn yields at the county level. The correlation coefficients are consistently high (mean values predominantly above 0.8) across all states of US Corn Belt. This robust correlation confirms that the pre-trained NeuralCrop effectively learned and reproduced the corn yield behavior of LPJmL.

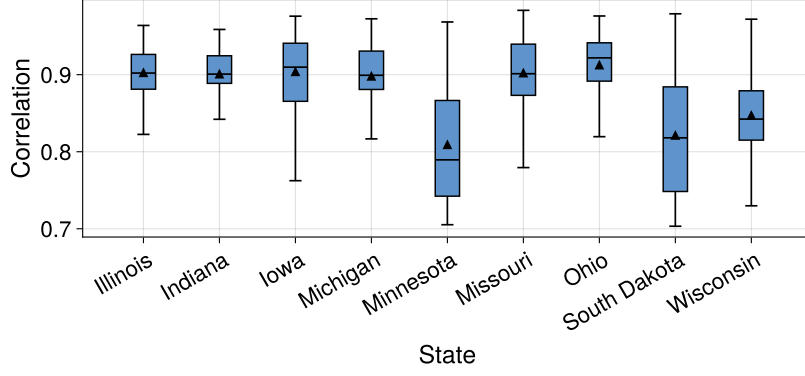


Fig. S13 Boxplots of time series correlation coefficient of simulated corn yields between pre-trained NeuralCrop and LPJmL at the county level, aggregated by state for the period 2000–2019. The box boundaries represent the interquartile range (IQR), defined by the first quartile, the median, and the third quartile. The upper and lower whiskers represent the maximum and minimum that are within 1.5 times the interquartile range of the box. The black triangles are the mean value.

G.2.3 Fine-tuning

NeuralCrop models were further fine-tuned using site-level eddy-covariance flux tower data across major US corn cropping regions. The corn flux data comprised 10 flux tower sites distributed in the states of Missouri, Nebraska, Minnesota, and California (Table S8 and Fig. S14), covering a broad range of climatic and management conditions. These observations provide daily GPP, RECO, NEE, and, for most sites, SWC, as well as auxiliary meteorological variables, spanning from 2001 to 2023. Since crop rotation is practiced at most sites, we excluded flux data from non-target crop years and retained only the data of periods during which the corn was growing. Finally, the dataset included 26 site-years of corn flux observations for fine-tuning.

Table S8 Overview of US corn flux tower sites used for fine-tuning of NeuralCrop.

Site	(latitude, longitude)	Year	Source
US-Bi2 [42]	(38.1091, -121.5351)	2017-2021	AmeriFlux
US-Mo1 [43]	(39.2298, -92.1167)	2015-2023	AmeriFlux
US-Mo3 [44]	(39.2322, -92.1493)	2016-2021	AmeriFlux
US-Ne1 [28]	(41.1651, -96.4766)	2001-2020	AmeriFlux
US-Ne2 [45]	(41.1649, -96.4701)	2001-2013	AmeriFlux
US-Ne3 [46]	(41.1797, -96.4397)	2001-2013	AmeriFlux
US-Ro1 [47]	(44.7143, -93.0898)	2004-2016	AmeriFlux
US-Ro3 [48]	(44.7217, -93.0893)	2004-2007	AmeriFlux
US-Ro5 [49]	(44.6910, -93.0576)	2017-2023	AmeriFlux
US-Ro6 [50]	(44.6946, -93.0578)	2017-2023	AmeriFlux

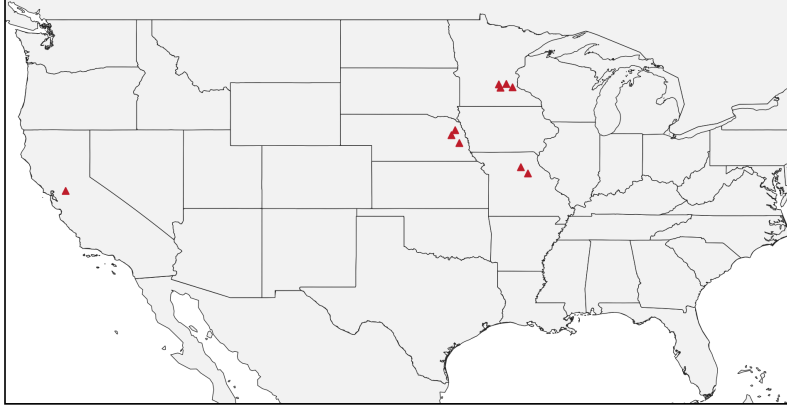


Fig. S14 Geographical locations of the US corn flux tower sites used for fine-tuning NeuralCrop.

G.3 Yield aggregation

NeuralCrop and LPJmL simulate yields on a global grid at $0.5^\circ \times 0.5^\circ$ (latitude \times longitude) spatial resolution, whereas reported yields are usually available at the county level or for even larger administrative units. To make the simulated yields comparable with these observations, we first linearly downscale the 0.5° outputs to a finer 0.05° grid by uniformly assigning the original cell value to all sub-cells, and then aggregate the 0.05° yields to target regions using the harvested-area weighted method, see below.

Let $H_{j,t}$ denote the harvested area of the target crop in 0.05° grid j and year t . For a region r (e.g., county, state, or country), the harvested-area weighted mean yield $\bar{y}_{r,t}$ is computed as

$$\bar{y}_{r,t} = \sum_{j \in r} \alpha_{j,t} y_{j,t}^{0.05}, \quad \alpha_{j,t} = \frac{H_{j,t}}{\sum_{j \in r} H_{j,t}}, \quad (32)$$

where $\alpha_{j,t}$ is the fraction of the regional harvested area located in grid cell j .

G.4 Yield detrending

In order to remove the effects of long-term improvements associated with crop breeding and management while retaining interannual variability primarily driven by climate fluctuations, we use smoothing splines to detrend the simulated and observed yield time series. Given time series (t, y_t) , $t = 1, 2, \dots, T$, where t denotes the year and y_t represents the corresponding crop yield (either simulated or observed), the smoothing spline estimate $\hat{f}(x)$ of the function $f(t)$ is obtained by minimizing the following objective function:

$$\sum_{i=1}^T (y_t - f(t))^2 + \lambda \int [f''(t)]^2 dt, \quad (33)$$

where the first term, $\sum_{i=1}^T (y_t - f(t))^2$, measures the lack of fit to the data, the second term, $\int [f''(t)]^2 dt$, penalizes curvature of the function, thereby enforcing smoothness, and $\lambda (\geq 0)$ is the smoothing parameter, which controls the trade-off between goodness of fit and smoothness. The optimal solution $f(x)$ is a cubic spline function. As $\lambda \rightarrow 0$, the solution approaches an interpolating spline, exactly passing through all data points. As $\lambda \rightarrow \infty$, the solution converges to a linear function, representing complete smoothing. In this study, the smoothing parameter λ is selected empirically based on the characteristics of the yield time series. The detrended yield time series is then obtained as:

$$y_t^{\text{detrended}} = y_t - \hat{f}(t). \quad (34)$$

G.5 Yield anomalies

Yield anomalies are calculated to measure the relative deviation of annual yields from their long-term trends. Specifically, given the simulated or observed yield y_t in year t and the corresponding expected yield $\hat{f}(t)$ estimated by a smoothing spline function (Section G.4), the normalized yield anomaly is defined as:

$$\hat{a}_t = \frac{y_t - \hat{f}(t)}{\hat{f}(t)}. \quad (35)$$

G.6 Standardized Precipitation Evapotranspiration Index

The Standardized Precipitation Evapotranspiration Index (SPEI) is a drought index that combines precipitation (P) and potential evapotranspiration (PET) [51]. It can be used to characterize drought intensity, duration, and frequency across different timescales, thereby providing a consistent framework to assess water availability impacts on agriculture. SPEI is defined as the difference between P_t and PET_t at time t :

$$D_t = P_t - PET_t, \quad (36)$$

where PET_t is calculated using Priestley-Taylor equation, following LPJmL scheme [10]. The accumulated water balance over a timescale of k months is then given by:

$$D_{t,k} = \sum_{i=0}^{k-1} (P_{t-i} - PET_{t-i}), \quad (37)$$

where $D_{t,k}$ represents the climatic water balance integrated over k months. The series $D_{t,k}$ is fitted to a probability distribution (typically Logistic) and transformed into a standardized normal variable with mean zero and unit variance. The standardized index is expressed as:

$$\text{SPEI}_{t,k} = \frac{D_{t,k} - \mu}{\sigma}, \quad (38)$$

where μ and σ are the mean and standard deviation of the fitted distribution, respectively. Negative values of $\text{SPEI}_{t,k}$ indicate drier conditions than normal, while positive values indicate wetter conditions than normal.

In this study, SPEI is calculated using an accumulation period of $k = 3$ months. We select SPEI during key crop growth stages to assess water availability relevant to crop production. Based on calculated SPEI values, drought severity is categorized into four classes:

Table S9 Dryness classification based on SPEI.

Value	Classification
$1.5 \leq \text{SPEI} \leq \infty$	Extremely Wet
$1.0 \leq \text{SPEI} \leq 1.5$	Very Wet
$0.5 \leq \text{SPEI} \leq 1.0$	Moderately Wet
$-0.5 \leq \text{SPEI} \leq 0.5$	Normal
$-1.0 \leq \text{SPEI} < -0.5$	Moderately Dry
$-1.5 \leq \text{SPEI} < -1.0$	Very Dry
$-\infty \leq \text{SPEI} < -1.5$	Extremely Dry

G.7 Water use efficiency

Water use efficiency (WUE) is an indicator that links photosynthetic carbon gain to water loss through evapotranspiration (ET), providing insights into plant responses to water availability and drought stress. At time t , WUE is defined as the ratio between GPP and ET:

$$\text{WUE}_t = \frac{\text{GPP}_t}{\text{ET}_t}, \quad (39)$$

where GPP_t represents the total carbon fixed through photosynthesis, and ET_t denotes water loss through transpiration. Higher values of WUE indicate greater carbon assimilation per unit of water consumed, reflecting improved water-use performance and drought resilience of vegetation.

H Additional information

H.1 Long-term yield projection

H.1.1 European wheat

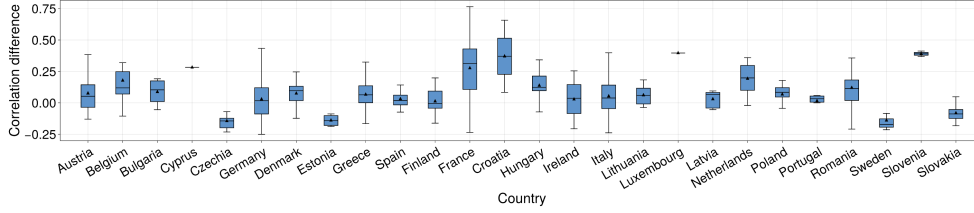


Fig. S15 Boxplots difference of time series correlation coefficient of simulated wheat yields between NeuralCrop and LPJmL at the subnational level, aggregated by country for the period 2000–2019, with countries ordered alphabetically by their country code (A–Z). The box boundaries represent the interquartile range (IQR), defined by the first quartile, the median, and the third quartile. The upper and lower whiskers represent the maximum and minimum that are within 1.5 times the interquartile range of the box. The black triangles are the mean value.

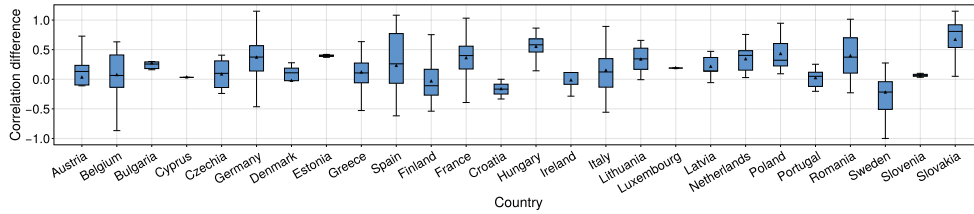


Fig. S16 Boxplots difference of time series correlation coefficient of simulated wheat yields between NeuralCrop and AgMIP crop models at the subnational level, aggregated by country for the period 2000–2016, with countries ordered alphabetically by their country code (A–Z). The AgMIP ensemble comprises five crop models: pDSSAT, EPIC-IIASA, LDNDC, ISAM, and PEPIC. The box boundaries represent the interquartile range (IQR), defined by the first quartile, the median, and the third quartile. The upper and lower whiskers represent the maximum and minimum that are within 1.5 times the interquartile range of the box. The black triangles are the mean value.

H.1.2 US Corn Belt

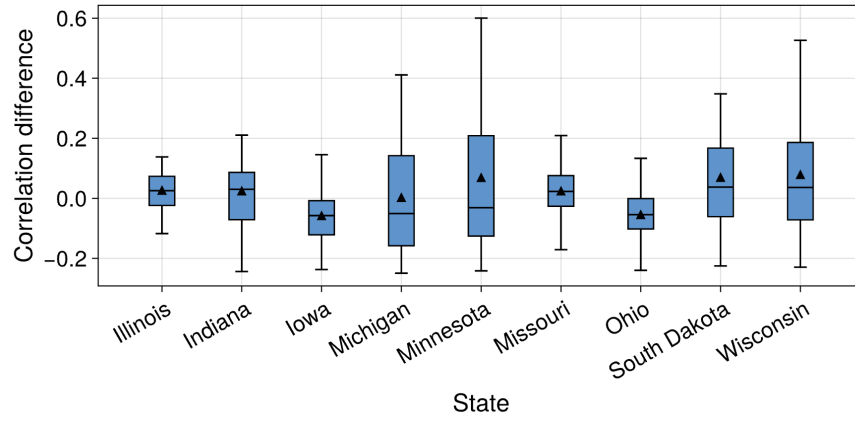


Fig. S17 Boxplots difference of time series correlation coefficient of simulated wheat yields between NeuralCrop and LPJm at the county level, aggregated by state for the period 2000–2019. The box boundaries represent the interquartile range (IQR), defined by the first quartile, the median, and the third quartile. The upper and lower whiskers represent the maximum and minimum that are within 1.5 times the interquartile range of the box. The black triangles are the mean value.

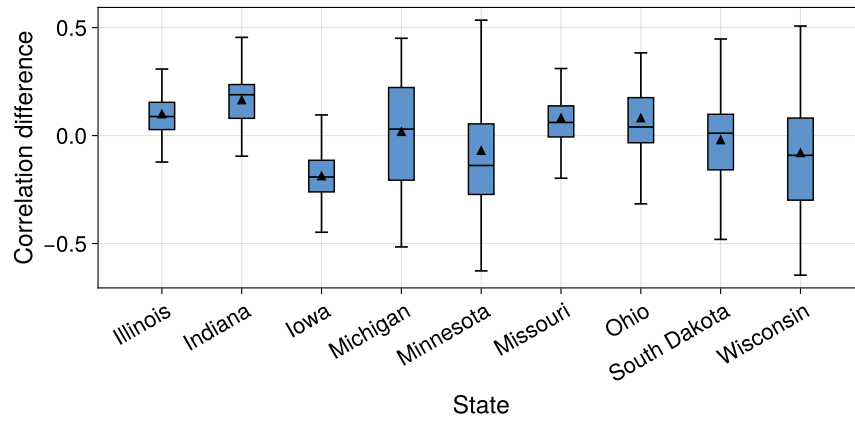


Fig. S18 Boxplots difference of time series correlation coefficient of simulated wheat yields between NeuralCrop and AgMIP crop models at the county level, aggregated by state for the period 2000–2016. The AgMIP ensemble comprises five crop models: pDSSAT, EPIC-IIASA, LDNDC, ISAM, and PEPIC. The box boundaries represent the interquartile range (IQR), defined by the first quartile, the median, and the third quartile. The upper and lower whiskers represent the maximum and minimum that are within 1.5 times the interquartile range of the box. The black triangles are the mean value.

H.1.3 US wheat

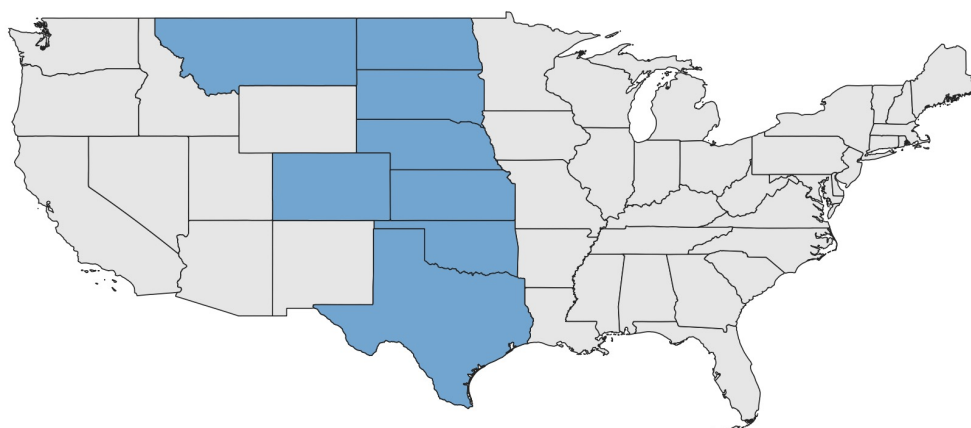


Fig. S19 States shaded in blue represent the US main wheat regions, including the states of Montana, North Dakota, South Dakota, Nebraska, Colorado, Kansas, Oklahoma, and Texas.

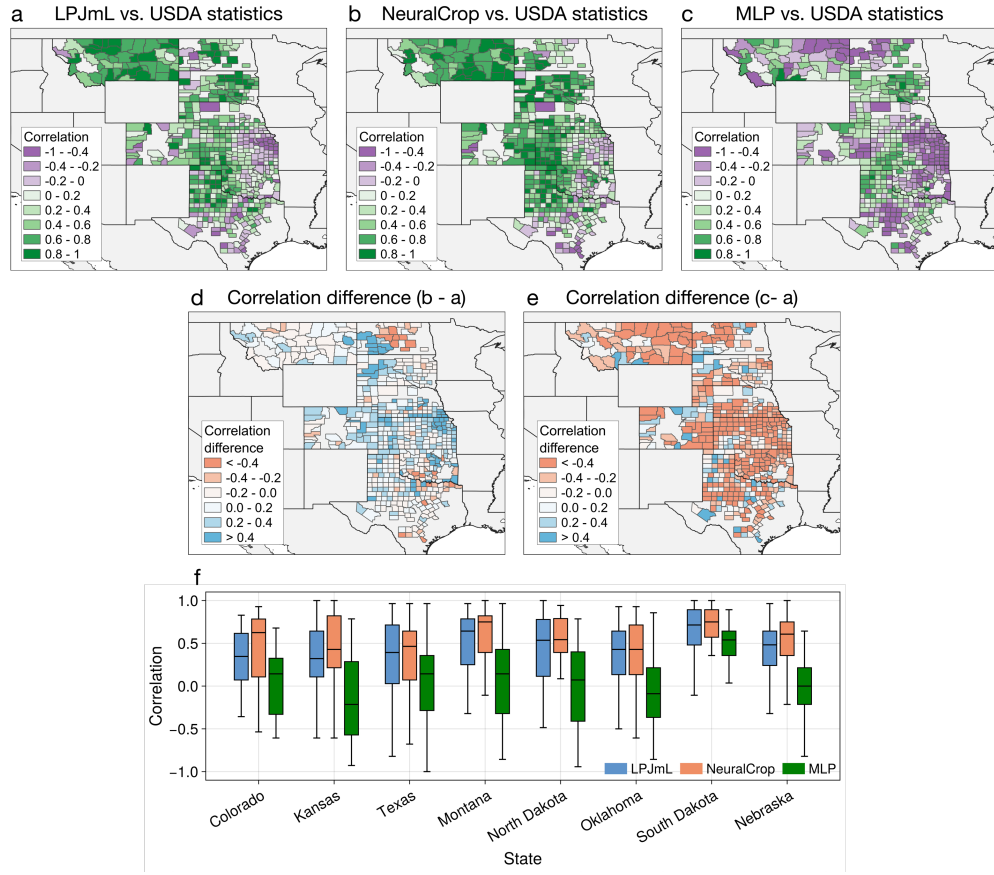


Fig. S20 Comparison of simulated wheat yields from NeuralCrop, LPJmL, and MLP with USDA statistics in US main wheat regions, including eight states (i.e., Montana, North Dakota, South Dakota, Nebraska, Colorado, Kansas, Oklahoma, and Texas). **a-c**, Time series correlation coefficient between simulated wheat yield (NeuralCrop, LPJmL, and MLP) and USDA statistics at the country level for the period 2000-2007 (range from -1 to 1, darker green areas indicate stronger positive correlations, and darker purple areas indicate stronger negative correlations). **d**, The difference of correlation coefficient (panel b - panel a), where blue areas indicate regions where NeuralCrop outperforms LPJmL in simulating interannual yield variability, and yellow areas indicate regions where LPJmL performs better. **e**, The difference of correlation coefficient (panel c - panel a), where blue areas indicate regions where MLP outperforms LPJmL in simulating interannual yield variability, and yellow areas indicate regions where LPJmL performs better. **f**, Boxplots of time series correlation coefficient between simulated wheat yield and USDA statistics at the country level, aggregated by states for the period 2000-2007. Blue boxes represent LPJmL simulations vs. USDA statistics, orange boxes represent NeuralCrop simulations vs. USDA statistics, and green boxes represent MLP simulations vs. USDA statistics. The box boundaries represent the interquartile range (IQR), defined by the first quartile, the median, and the third quartile. The upper and lower whiskers represent the maximum and minimum that are within 1.5 times the interquartile range of the box. The black triangles are the mean value.

H.2 Accuracy across moisture conditions

H.2.1 Yield anomalies over 2000–2019

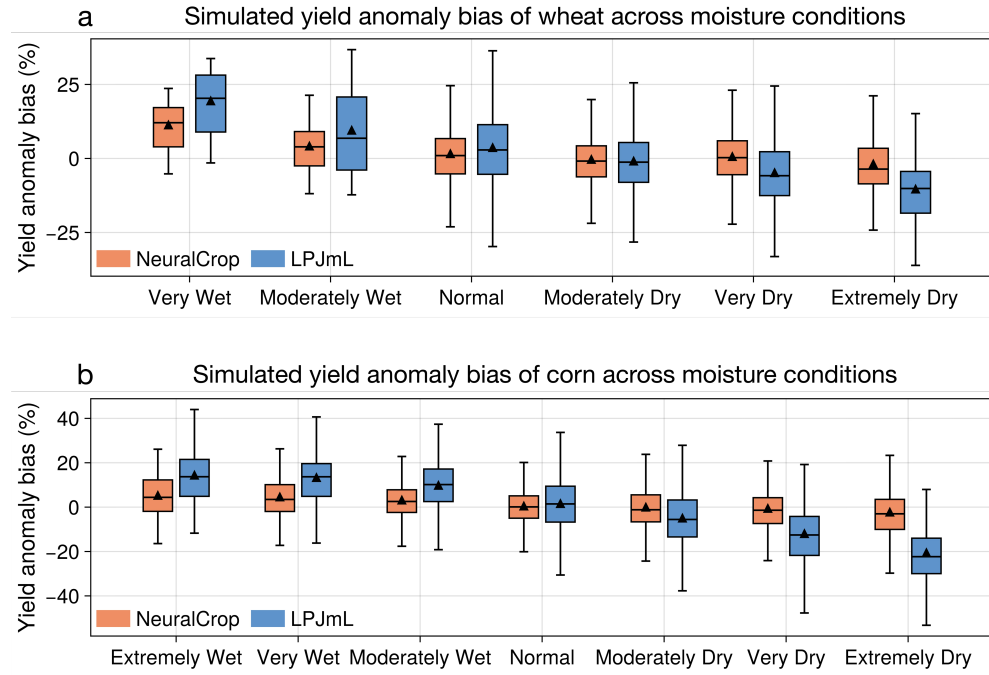


Fig. S21 Comparison of simulated yield anomaly bias from NeuralCrop and LPJmL for European wheat and US Corn Belt across moisture conditions at the subnational level during 2000–2019. **a**, The boxplots represent the yield anomaly bias of wheat in EU over the period 2000–2019, grouped by the April-June Standardized Precipitation Evapotranspiration Index (SPEI) (Extremely Wet: $1.5 < \text{SPEI}$; Very Wet: $1.0 \leq \text{SPEI} < 1.5$; Moderately Wet: $0.5 \leq \text{SPEI} < 1.0$; Normal: $-0.5 \leq \text{SPEI} < 0.5$; Moderately Dry: $-1.0 \leq \text{SPEI} < -0.5$; Very Dry: $-1.5 \leq \text{SPEI} < -1.0$; Extremely Dry: $\text{SPEI} < -1.5$). Orange boxes denote NeuralCrop, and blue boxes denote LPJmL. The box boundaries represent the interquartile range (IQR), defined by the first quartile, the median, and the third quartile. The upper and lower whiskers represent the maximum and minimum that are within 1.5 times the interquartile range of the box. The black triangles are the mean value. The bars below represent the root mean square error (RMSE) for NeuralCrop and LPJmL within each SPEI class. Orange bars denote NeuralCrop, and blue bars denote LPJmL. **b**, Same as panel (a), but for corn yield anomaly bias.

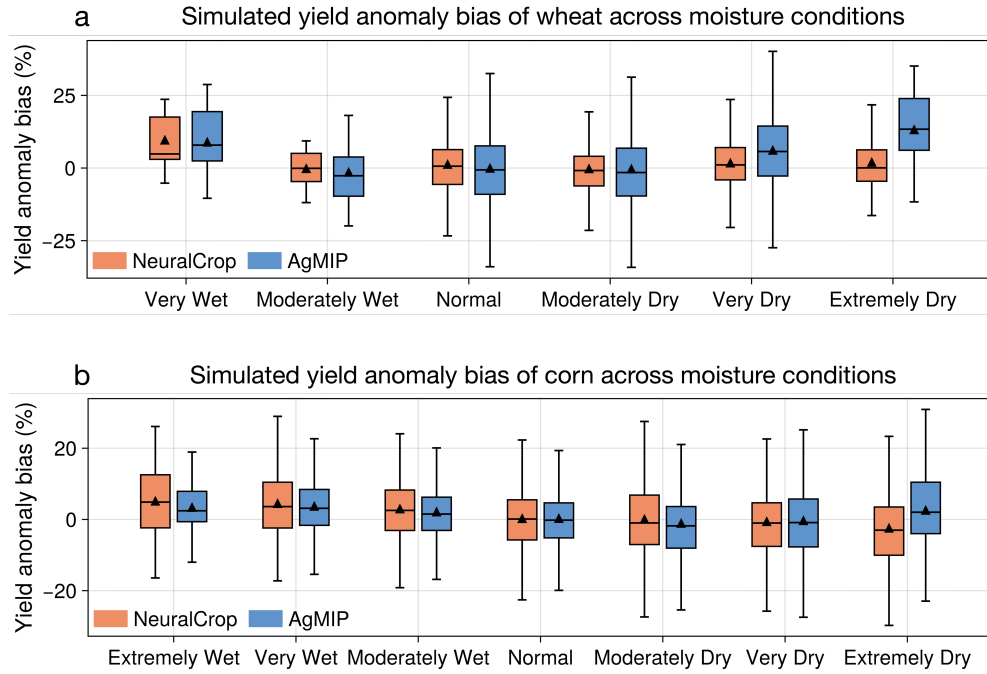


Fig. S22 Comparison of simulated yield anomaly bias from NeuralCrop and AgMIP crop models for European wheat and US Corn Belt across moisture conditions at the subnational level during 2000–2016. The AgMIP ensemble comprises five crop models: pDSSAT, EPIC-IIASA, LDNDC, ISAM, and PEPIC. **a**, The boxplots represent the yield anomaly bias of wheat in EU over the period 2000–2016, grouped by the April–June Standardized Precipitation Evapotranspiration Index (SPEI) (Extremely Wet: $1.5 \leq \text{SPEI}$; Very Wet: $1.0 \leq \text{SPEI} < 1.5$; Moderately Wet: $0.5 \leq \text{SPEI} < 1.0$; Normal: $-0.5 \leq \text{SPEI} < 0.5$; Moderately Dry: $-1.0 \leq \text{SPEI} < -0.5$; Very Dry: $-1.5 \leq \text{SPEI} < -1.0$; Extremely Dry: $\text{SPEI} < -1.5$). Orange boxes denote NeuralCrop, and blue boxes denote AgMIP ensemble median. The box boundaries represent the interquartile range (IQR), defined by the first quartile, the median, and the third quartile. The upper and lower whiskers represent the maximum and minimum that are within 1.5 times the interquartile range of the box. The black triangles are the mean value. The bars below represent the root mean square error (RMSE) of yield anomalies for NeuralCrop and AgMIP ensemble within each SPEI class. Orange bars denote NeuralCrop, and blue bars denote AgMIP ensemble median. **b**, Same as panel (a), but for corn yield anomaly bias.

H.2.2 European wheat anomalies in 2018

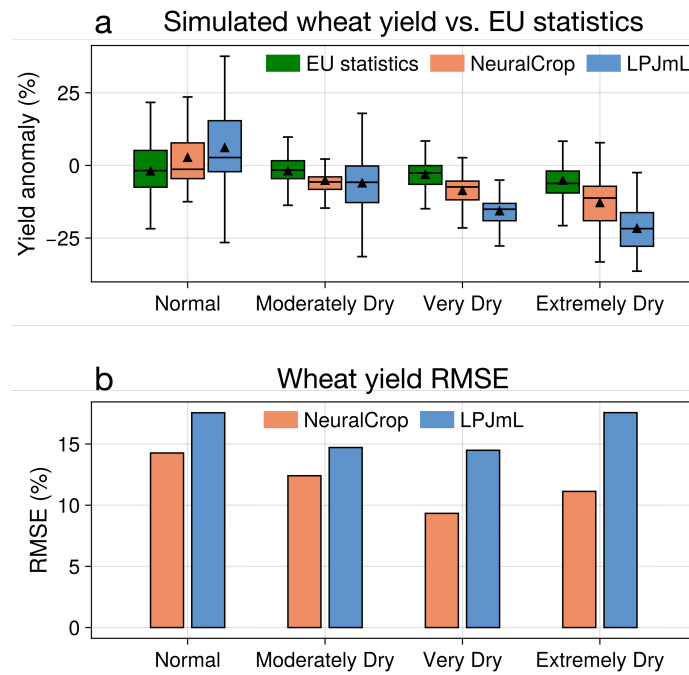


Fig. S23 Comparison of simulated wheat yields from NeuralCrop and LPJmL with EU statistics at the subnational level under the 2018 European drought. **a**, The boxplots represent the wheat yield anomalies, grouped by the April-June Standardized Precipitation Evapotranspiration Index (SPEI) (Normal: $-0.5 \leq \text{SPEI} < 0.5$; Moderately Dry: $-1.0 \leq \text{SPEI} < -0.5$; Very Dry: $-1.5 \leq \text{SPEI} < -1.0$; Extremely Dry: $\text{SPEI} < -1.5$). Green boxes denote EU statistics, orange boxes denote NeuralCrop, and blue boxes denote LPJmL. The box boundaries represent the interquartile range (IQR), defined by the first quartile, the median, and the third quartile. The upper and lower whiskers represent the maximum and minimum that are within 1.5 times the interquartile range of the box. The black triangles are the mean value. **b**, The bars represent the root mean square error (RMSE) of yield anomalies for NeuralCrop and LPJmL within each SPEI class. Orange bars denote NeuralCrop, and blue bars denote LPJmL..

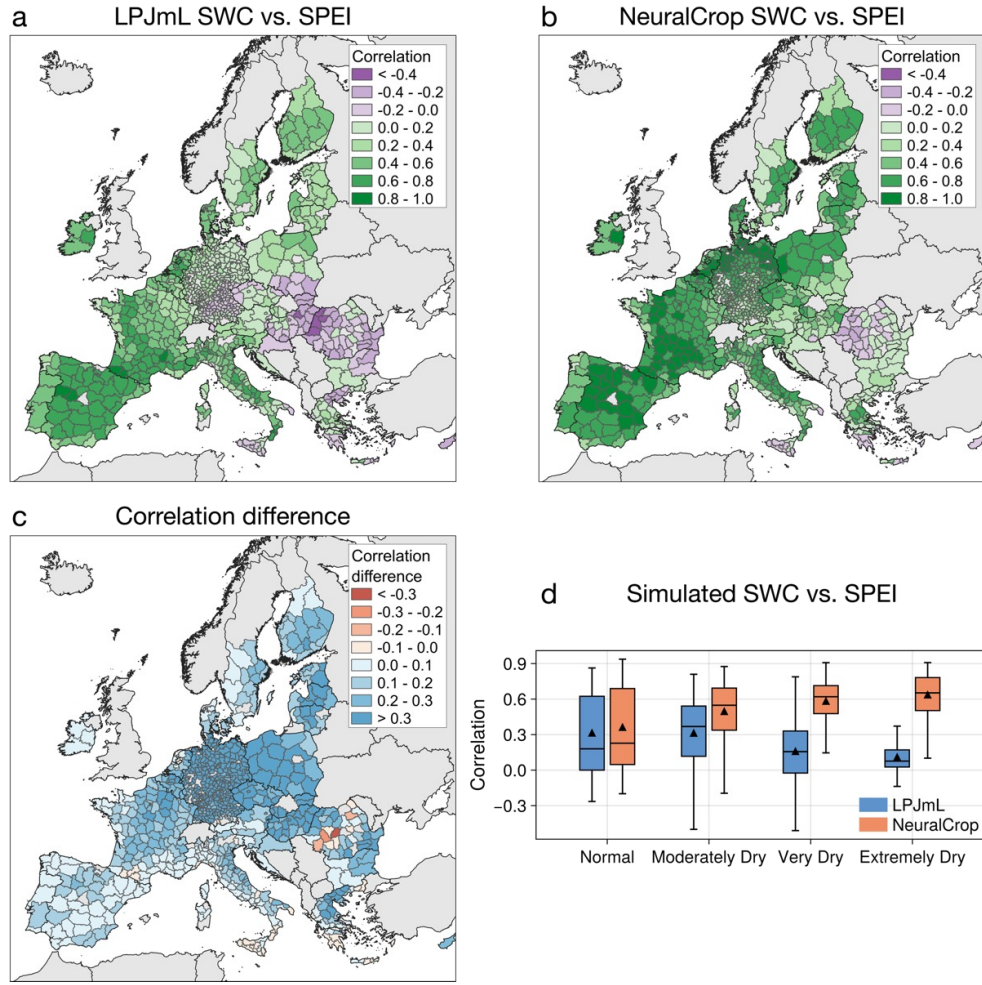


Fig. S24 Correlation between simulated soil water content (SWC) from NeuralCrop and LPJmL with the Standardized Precipitation Evapotranspiration Index (SPEI) in European wheat regions under the 2018 drought. **a-b**, Time series correlation coefficient (range from -1 to 1) between simulated SWC (LPJmL and NeuralCrop) and SPEI at the subnational level in 2018 (darker green areas indicate stronger positive correlations, and darker purple areas indicate stronger negative correlations). **c**, The difference of correlation coefficient (panel b - panel a), where blue areas indicate the correlation between SWC and SPEI simulated by NeuralCrop is higher than that simulated by LPJmL, and yellow areas indicate the correlation between SWC and SPEI simulated by NeuralCrop is lower than that simulated by LPJmL. **d**, Boxplots of time series correlation coefficient between simulated SWC and SPEI at the subnational level in 2018, grouped by the dryness classes. Blue boxes denote LPJmL, and orange boxes denote NeuralCrop. The upper and lower whiskers represent the maximum and minimum that are within 1.5 times the interquartile range of the box. The black triangles are the mean value.

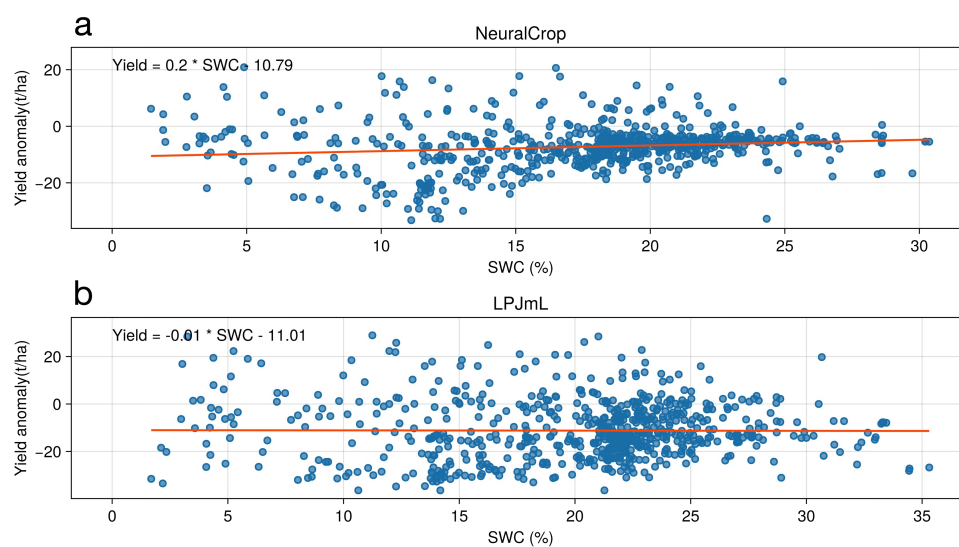


Fig. S25 Relationship between yield anomaly and simulated soil water content (SWC) in European wheat regions during the 2018 drought. **a-b**, Scatter plots of yield anomaly versus mean growing-season daily SWC for (a) EU statistics, (b) NeuralCrop simulations, and (c) LPJmL simulations at the subnational level. The red lines indicate linear regressions, with the regression equations shown in each panel. Weak correlations suggest that simulated SWC alone explains limited yield variability.

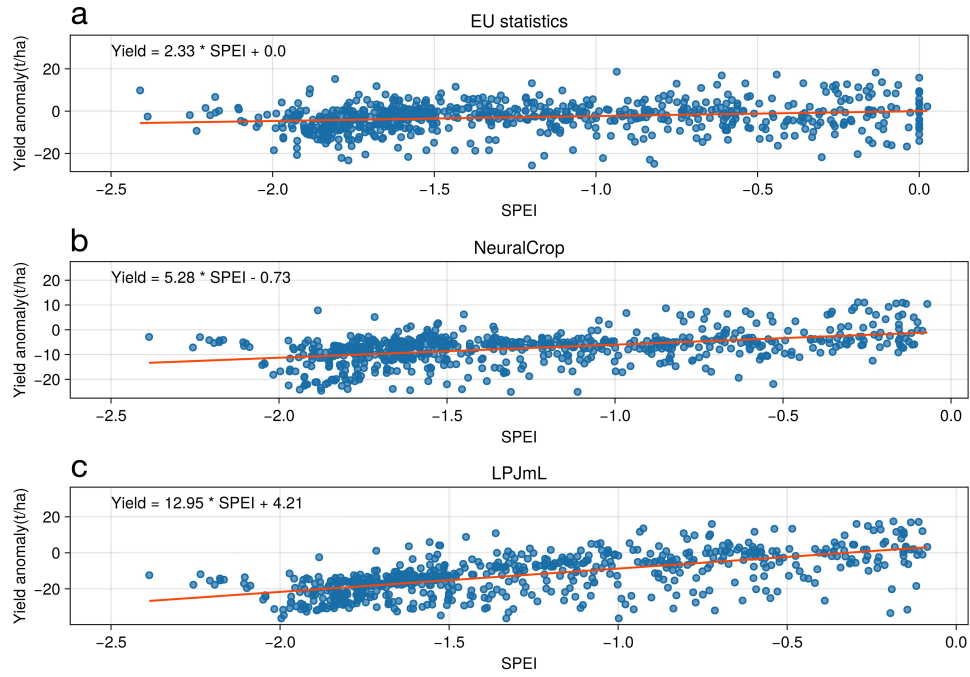


Fig. S26 Relationship between yield anomaly and the Standardized Precipitation Evapotranspiration Index (SPEI) in European wheat regions during the 2018 drought. **a-c**, Scatter plots of yield anomaly versus SPEI for (a) EU statistics, (b) NeuralCrop simulations, and (c) LPJmL simulations at the subnational level. The red lines indicate linear regressions, with the regression equations shown in each panel. Positive slopes indicate higher yields under wetter conditions (higher SPEI), whereas negative slopes indicate yield losses under drier conditions.

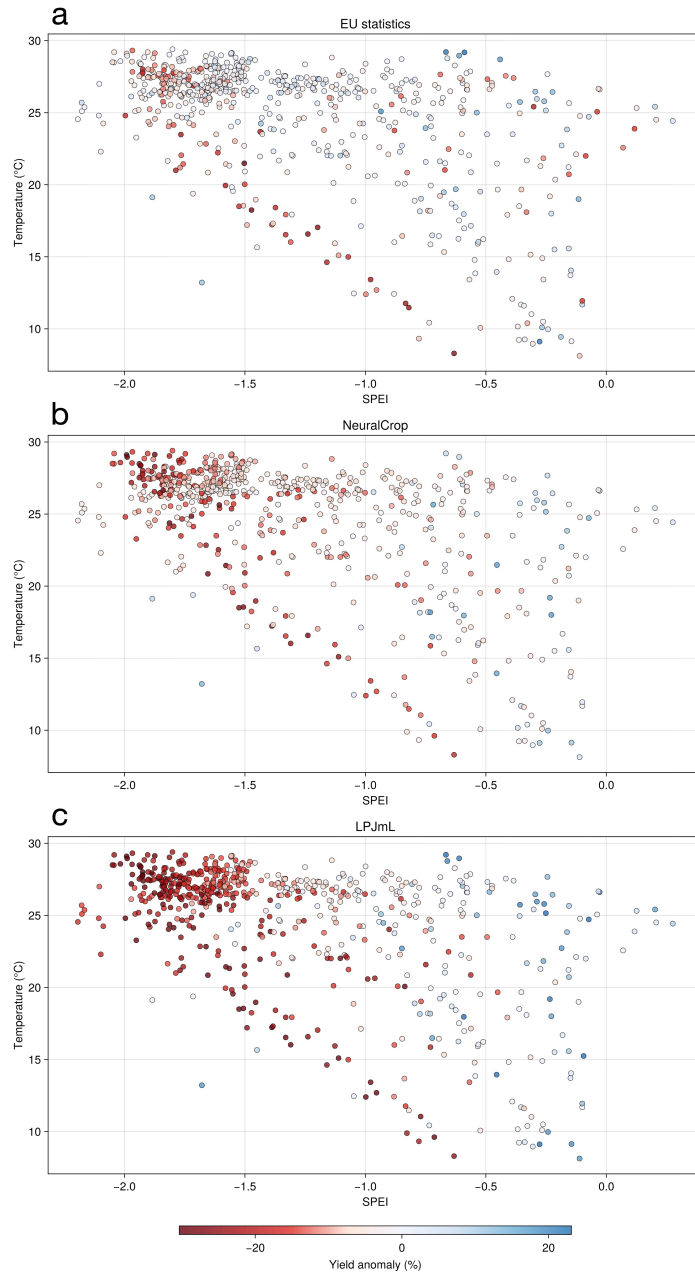


Fig. S27 Wheat yield anomaly patterns of NeuralCrop and LPJmL across compound drought-heat conditions in European wheat regions during the 2018 drought. **a-c**, Scatter plots of wheat yield anomaly (%) versus Standardized Precipitation Evapotranspiration Index (SPEI) and growing-season maximum temperature for (a) EU statistics, (b) NeuralCrop simulations, and (c) LPJmL simulations at the subnational level. Point colors represent yield anomalies, with red indicating negative anomalies (yield losses) and blue indicating positive anomalies (yield gains).

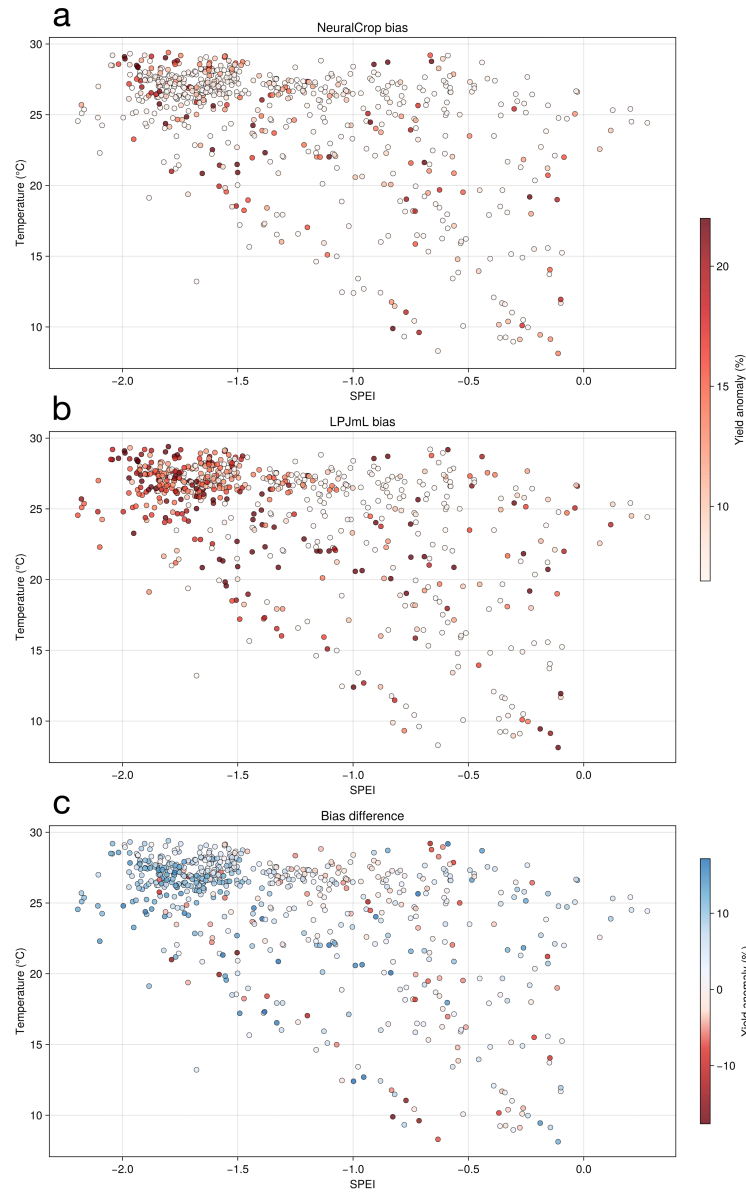


Fig. S28 Bias patterns of NeuralCrop and LPJmL across compound drought–heat conditions in European wheat regions during the 2018 drought. **a–b**, Scatter plots showing simulated yield anomaly biases (%) relative to EU statistics versus SPEI and growing-season maximum temperature for (a) NeuralCrop and (b) LPJmL simulations at the subnational level. Point colors indicate the magnitude of model bias, with red representing overestimation of yield losses and blue representing underestimation. **c**, The bias difference between NeuralCrop and LPJmL (panel b – panel a), with blue representing regions where NeuralCrop has smaller biases than LPJmL and red representing regions where NeuralCrop has larger biases than LPJmL.

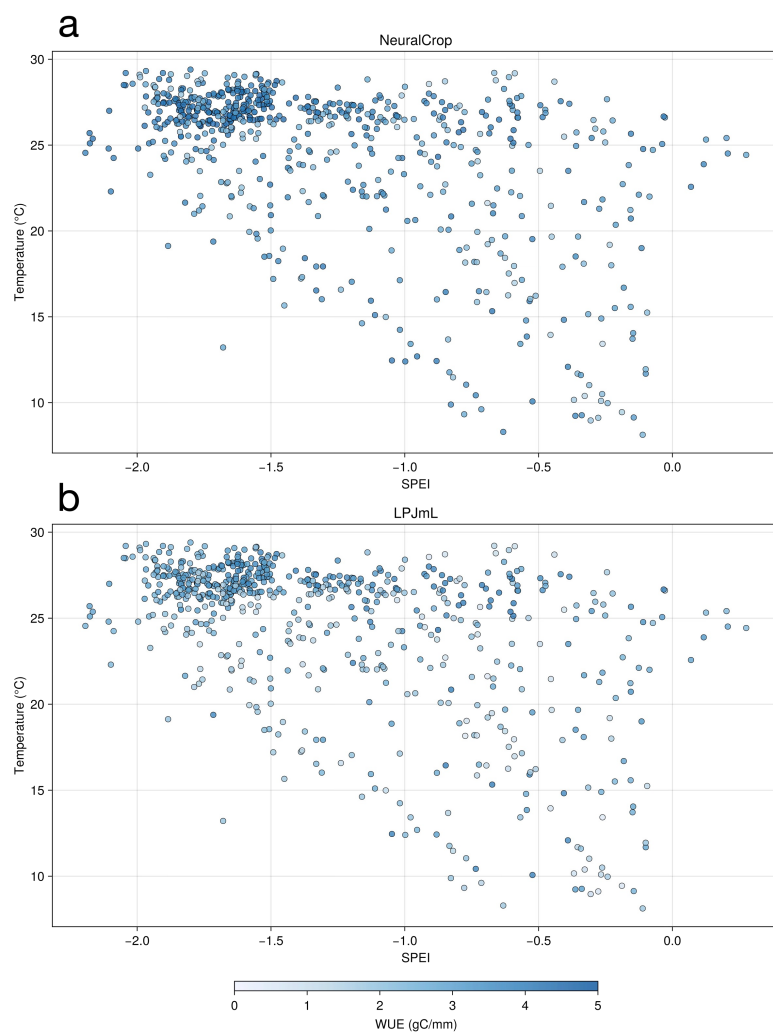


Fig. S29 Relationships between the Standardized Precipitation Evapotranspiration Index (SPEI), growing season maximum temperature, and water use efficiency (WUE) in European wheat regions during the 2018 drought. **a-b**, Scatter plots of WUE versus SPEI and growing-season maximum temperature for (a) NeuralCrop and (b) LPJmL simulations at the subnational level. Point colors represent WUE.

H.2.3 US Corn Belt anomalies in 2012

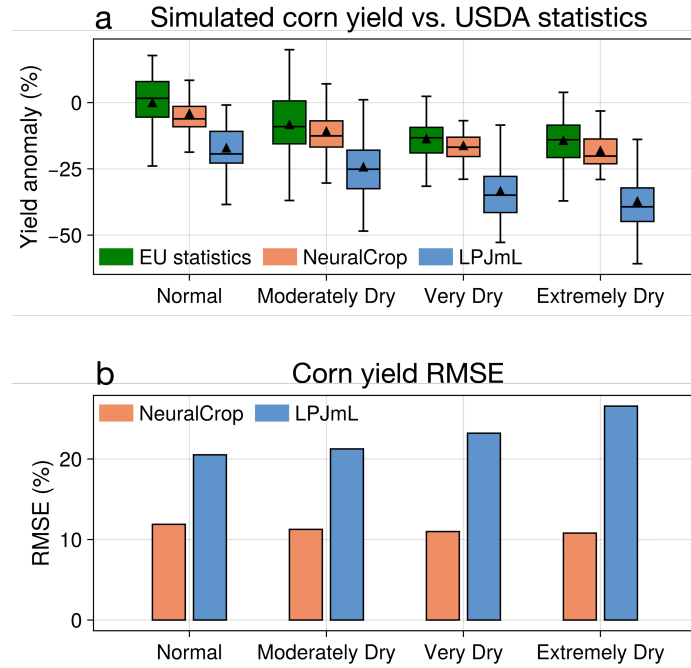


Fig. S30 Comparison of simulated corn yields from NeuralCrop and LPJmL with USDA statistics at the subnational level under the 2012 US drought. **a**, The boxplots represent the corn yield anomalies, grouped by the May-July Standardized Precipitation Evapotranspiration Index (SPEI) (Normal: $-0.5 \leq \text{SPEI} < 0.5$; Moderately Dry: $-1.0 \leq \text{SPEI} < -0.5$; Very Dry: $-1.5 \leq \text{SPEI} < -1.0$; Extremely Dry: $\text{SPEI} < -1.5$). Green boxes denote EU statistics, orange boxes denote NeuralCrop, and blue boxes denote LPJmL. The box boundaries represent the interquartile range (IQR), defined by the first quartile, the median, and the third quartile. The upper and lower whiskers represent the maximum and minimum that are within 1.5 times the interquartile range of the box. The black triangles are the mean value. **b**, The bars represent the root mean square error (RMSE) of yield anomalies for NeuralCrop and LPJmL within each SPEI class. Orange bars denote NeuralCrop, and blue bars denote LPJmL.

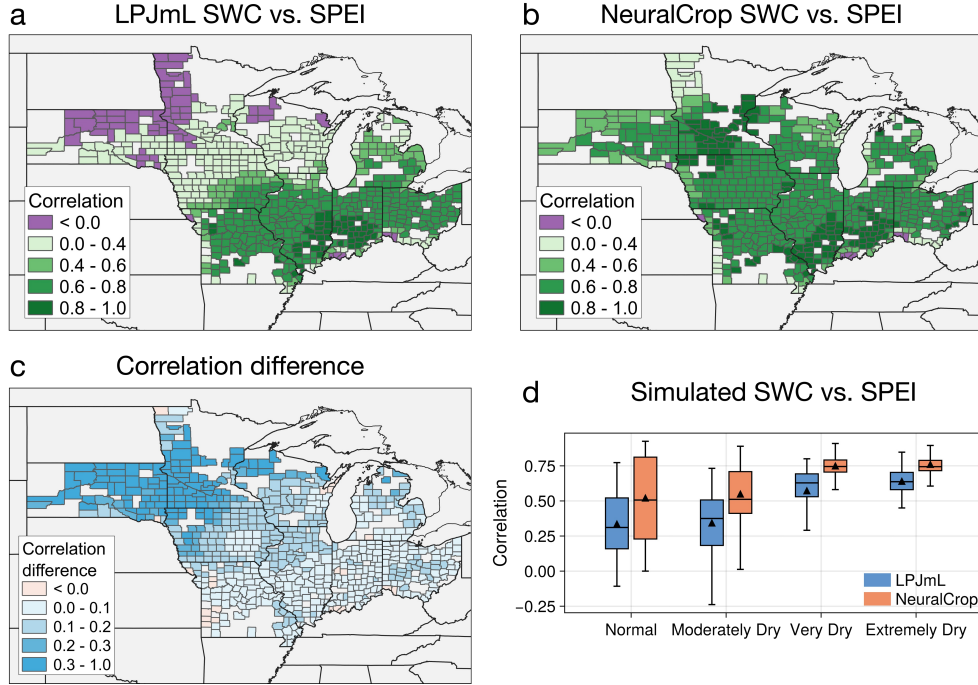


Fig. S31 Correlation between simulated soil water content (SWC) from NeuralCrop and LPJmL with the Standardized Precipitation Evapotranspiration Index (SPEI) in US Corn Belt, including nine states (i.e., South Dakota, Minnesota, Iowa, Missouri, Wisconsin, Illinois, Michigan, Indiana, and Ohio, under the 2012 drought. **a-b**, Time series correlation coefficient (range from -1 to 1) between simulated SWC (LPJmL and NeuralCrop) and SPEI at the county level in 2012 (darker green areas indicate stronger positive correlations, and purple areas indicate negative correlations). **c**, The difference of correlation coefficient (panel b – panel a), where blue areas indicate the correlation between SWC and SPEI simulated by NeuralCrop is higher than that simulated by LPJmL, and yellow areas indicate the correlation between SWC and SPEI simulated by NeuralCrop is lower than that simulated by LPJmL. **d**, Boxplots of time series correlation coefficient between simulated SWC and SPEI at the county level in 2012, grouped by the dryness classes. Blue boxes denote LPJmL, and orange boxes denote NeuralCrop. The upper and lower whiskers represent the maximum and minimum that are within 1.5 times the interquartile range of the box. The black triangles are the mean value.

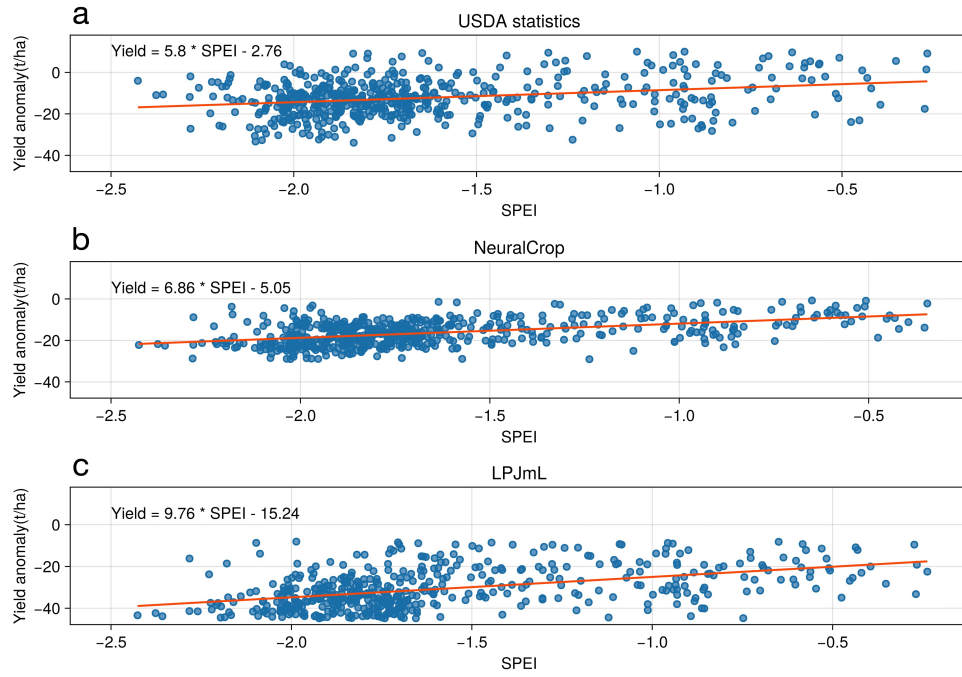


Fig. S32 Relationship between yield anomaly and the Standardized Precipitation Evapotranspiration Index (SPEI) in the US Corn Belt during the 2012 drought. **a-c**, Scatter plots of yield anomaly versus SPEI for (a) USDA statistics, (b) NeuralCrop simulations, and (c) LPJmL simulations at the county level. The red lines indicate linear regressions, with the regression equations shown in each panel. Positive slopes indicate higher yields under wetter conditions (higher SPEI), whereas negative slopes indicate yield losses under drier conditions.

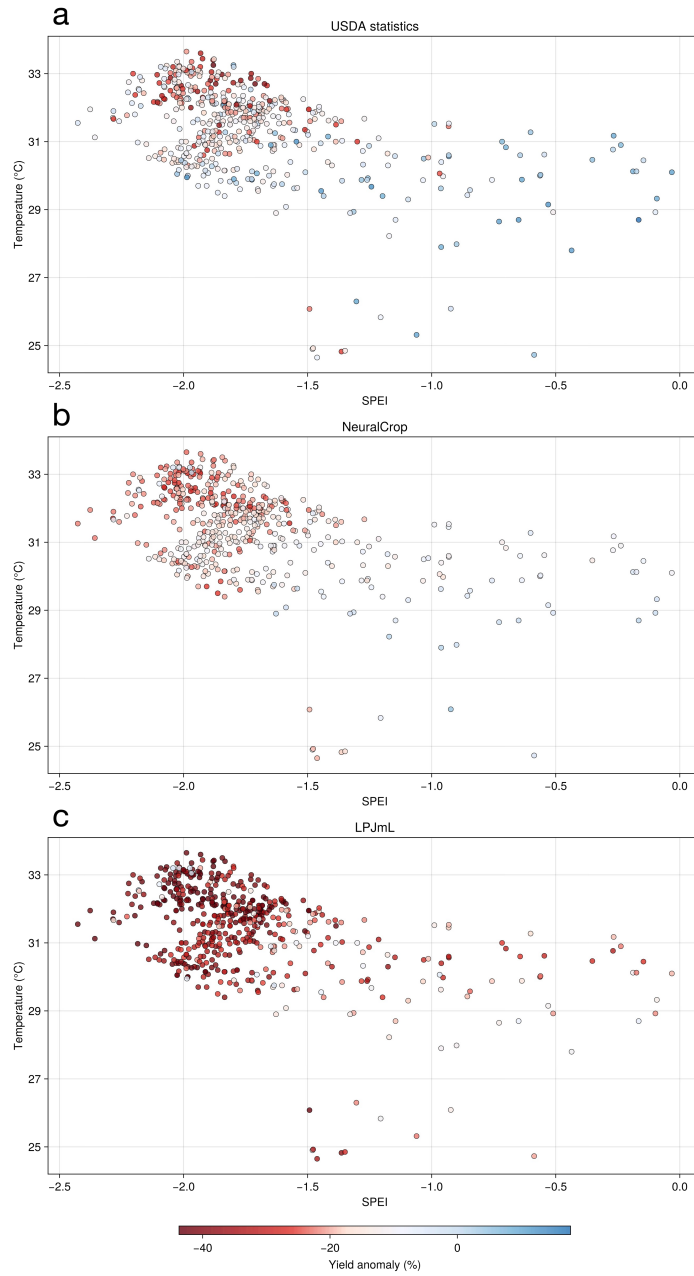


Fig. S33 Wheat yield anomaly patterns of NeuralCrop and LPJmL across compound drought–heat conditions in the US Corn Belt during the 2012 drought. **a–c**, Scatter plots of wheat yield anomaly (%) versus SPEI and growing-season maximum temperature for (a) USDA statistics, (b) NeuralCrop simulations, and (c) LPJmL simulations at the county level. Point colors represent yield anomalies, with red indicating negative anomalies (yield losses) and blue indicating positive anomalies (yield gains).

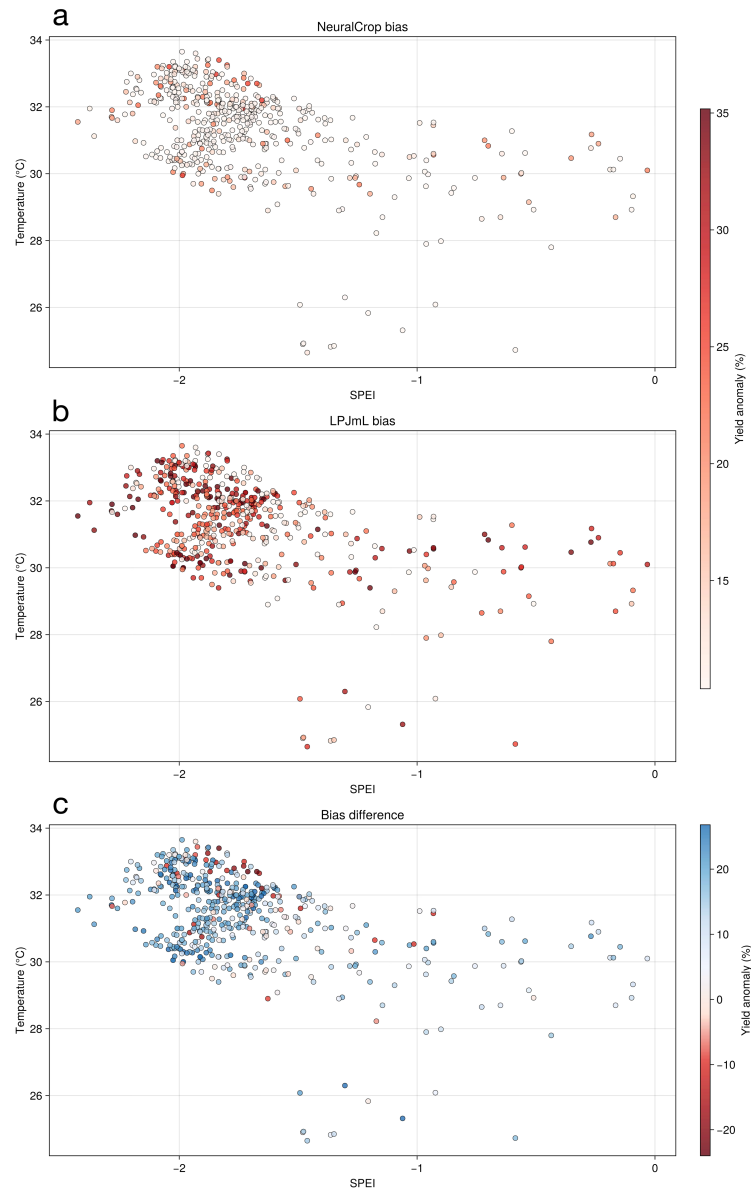


Fig. S34 Bias patterns of NeuralCrop and LPJmL across compound drought–heat conditions in the US Corn Belt during the 2012 drought. **a–b**, Scatter plots showing simulated yield anomaly biases (%) relative to USDA statistics versus SPEI and growing-season maximum temperature for (a) NeuralCrop and (b) LPJmL simulations at the subnational level. Point colors indicate the magnitude of model bias, with red representing overestimation of yield losses and blue representing underestimation. **c**, The bias difference between NeuralCrop and LPJmL (panel b – panel a), with blue representing regions where NeuralCrop has smaller biases than LPJmL and red representing regions where NeuralCrop has larger biases than LPJmL.

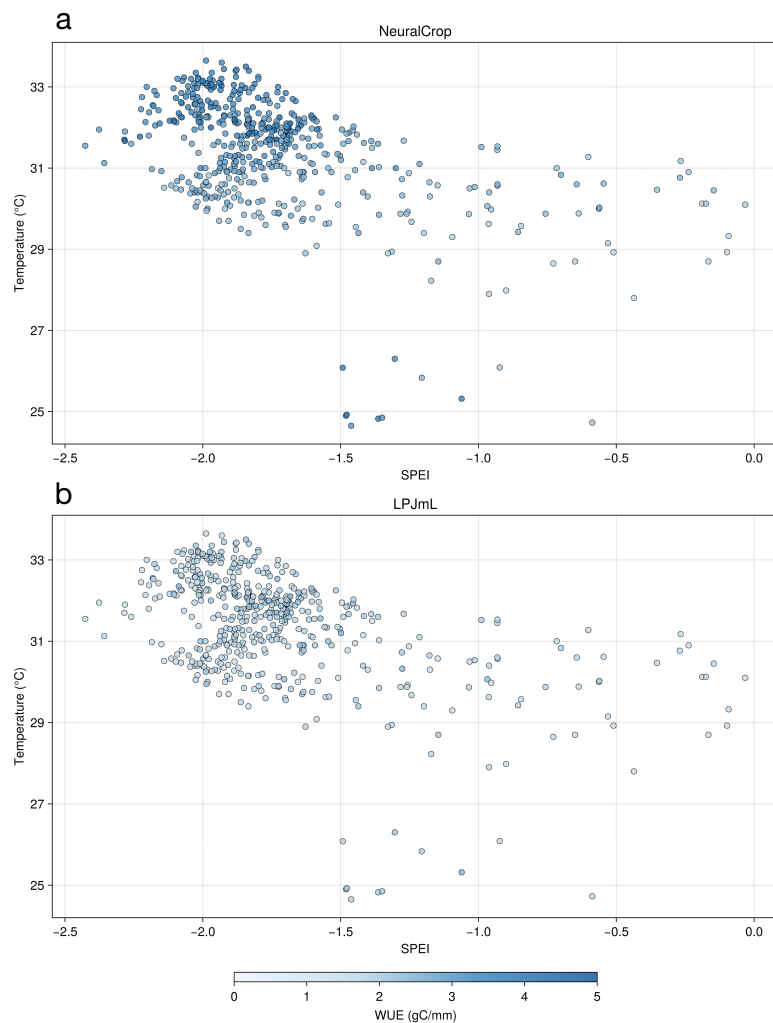


Fig. S35 Relationships between the Standardized Precipitation Evapotranspiration Index (SPEI), growing season maximum temperature, and water use efficiency (WUE) in the US Corn Belt during the 2012 drought. **a-b**, Scatter plots of WUE versus SPEI and growing-season maximum temperature for (a) NeuralCrop and (b) LPJmL simulations at the county level. Point colors represent WUE.

H.2.4 France wheat anomalies in 2016

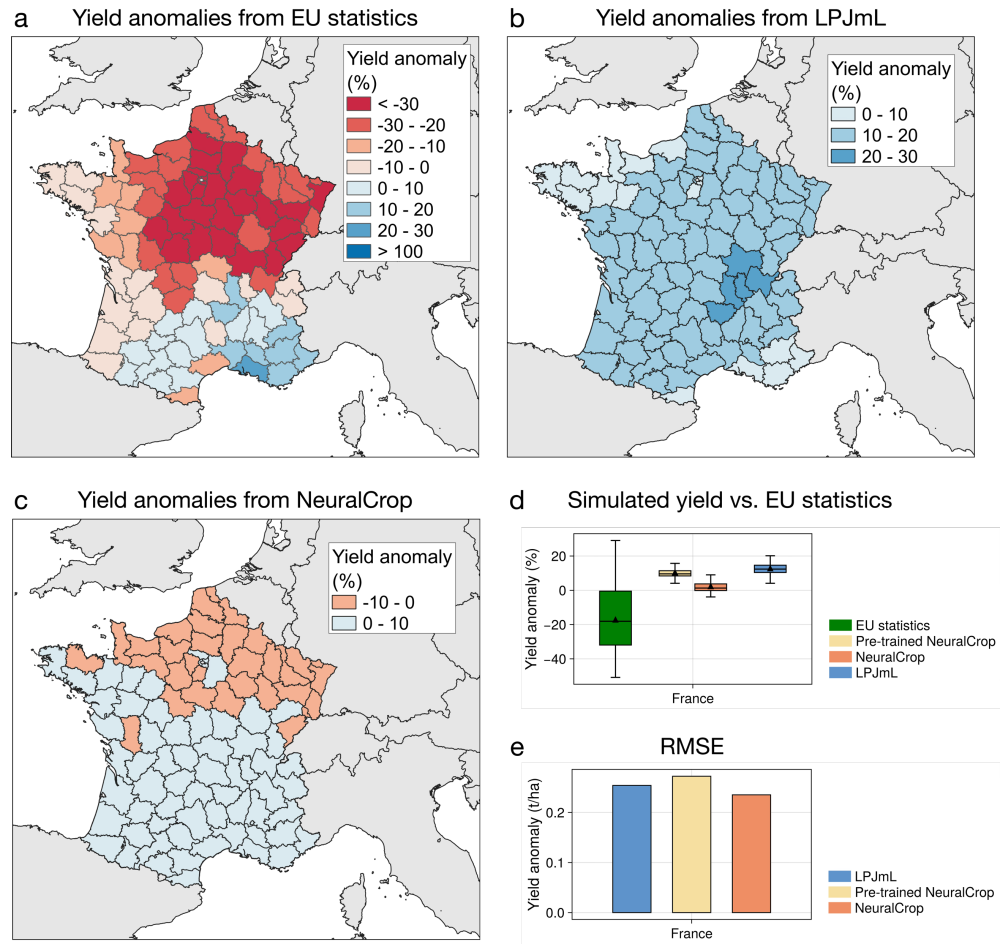


Fig. S36 Wheat yield anomalies and model performance for NeuralCrop and LPJmL under the 2016 heavy rainfall in France. **a**, Wheat yield anomalies in 2012 at the subnational level from EU statistics. **b**, Wheat yield anomalies in 2012 at the subnational level from LPJmL. **c**, Wheat yield anomalies in 2012 at the subnational level from NeuralCrop. **d**, Boxplots of 2012 wheat yield anomalies (%). Green box denotes EU statistics, yellow box denotes pre-trained NeuralCrop, orange box denotes NeuralCrop, and blue box denotes LPJmL. The upper and lower whiskers represent the maximum and minimum that are within 1.5 times the interquartile range of the box. The black triangles are the mean value. **e**, Root mean square error (RMSE) between simulated 2012 yield anomalies and EU statistics. Yellow box denotes pre-trained NeuralCrop, orange box denotes NeuralCrop, and blue box denotes LPJmL.

References

- [1] Ricky TQ Chen, Yulia Rubanova, Jesse Bettencourt, and David K Duvenaud. Neural ordinary differential equations. *Advances in neural information processing systems*, 31, 2018.
- [2] Jeff Bezanson, Alan Edelman, Stefan Karpinski, and Viral B Shah. Julia: A fresh approach to numerical computing. *SIAM review*, 59(1):65–98, 2017.
- [3] Christopher Rackauckas, Yingbo Ma, Julius Martensen, Collin Warner, Kirill Zubov, Rohit Supekar, Dominic Skinner, Ali Ramadhan, and Alan Edelman. Universal differential equations for scientific machine learning. *arXiv preprint arXiv:2001.04385*, 2020.
- [4] Avik Pal. Lux: Explicit Parameterization of Deep Neural Networks in Julia, April 2023. If you use this software, please cite it as below.
- [5] Avik Pal. On Efficient Training & Inference of Neural Differential Equations, 2023.
- [6] Michael Innes. Don’t unroll adjoint: Differentiating ssa-form programs. *CoRR*, abs/1810.07951, 2018.
- [7] Tim Besard, Christophe Foket, and Bjorn De Sutter. Effective extensible programming: Unleashing Julia on GPUs. *IEEE Transactions on Parallel and Distributed Systems*, 2018.
- [8] Tim Besard, Valentin Churavy, Alan Edelman, and Bjorn De Sutter. Rapid software prototyping for heterogeneous and distributed platforms. *Advances in Engineering Software*, 132:29–46, 2019.
- [9] Valentin Churavy. KernelAbstractions.jl.
- [10] Sibyll Schaphoff, Werner von Bloh, Anja Rammig, Kirsten Thonicke, Hester Biemans, Matthias Forkel, Dieter Gerten, Jens Heinke, Jonas Jägermeyr, Jürgen Knauer, et al. Lpjml4—a dynamic global vegetation model with managed land—part 1: Model description. *Geoscientific Model Development*, 11(4):1343–1375, 2018.
- [11] Graham D Farquhar, S von von Caemmerer, and Joseph A Berry. A biochemical model of photosynthetic co2 assimilation in leaves of c3 species. *planta*, 149(1):78–90, 1980.
- [12] Graham D Farquhar and S Von Caemmerer. Modelling of photosynthetic response to environmental conditions. In *Physiological plant ecology II: Water relations and carbon assimilation*, pages 549–587. Springer, 1982.

- [13] G James Collatz, J Timothy Ball, Cyril Grivet, and Joseph A Berry. Physiological and environmental regulation of stomatal conductance, photosynthesis and transpiration: a model that includes a laminar boundary layer. *Agricultural and Forest meteorology*, 54(2-4):107–136, 1991.
- [14] G James Collatz, Miquel Ribas-Carbo, and Joseph A Berry. Coupled photosynthesis-stomatal conductance model for leaves of c4 plants. *Functional Plant Biology*, 19(5):519–538, 1992.
- [15] Alex Haxeltine and IC Prentice. A general model for the light-use efficiency of primary production. *Functional Ecology*, pages 551–561, 1996.
- [16] I Colin Prentice, Martin Heimann, and Stephen Sitch. The carbon balance of the terrestrial biosphere: Ecosystem models and atmospheric observations. *Ecological Applications*, 10(6):1553–1573, 2000.
- [17] Yiqi Luo, Yuanyuan Huang, Carlos A Sierra, Jianyang Xia, Anders Ahlström, Yizhao Chen, Oleksandra Hararuk, Enqing Hou, Lifen Jiang, Cuijuan Liao, et al. Matrix approach to land carbon cycle modeling. *Journal of Advances in Modeling Earth Systems*, 14(7):e2022MS003008, 2022.
- [18] Stephen Sitch, Benjamin Smith, I Colin Prentice, Almut Arneth, Alberte Bondeau, Wolfgang Cramer, Jed O Kaplan, Samuel Levis, Wolfgang Lucht, M Thonicke Sykes, et al. Evaluation of ecosystem dynamics, plant geography and terrestrial carbon cycling in the lpj dynamic global vegetation model. *Global change biology*, 9(2):161–185, 2003.
- [19] Werner von Bloh, Sibyll Schaphoff, Christoph Müller, Susanne Rolinski, Katharina Waha, and Sönke Zaehle. Implementing the nitrogen cycle into the dynamic global vegetation, hydrology, and crop growth model lpjml (version 5.0). *Geoscientific Model Development*, 11(7):2789–2812, 2018.
- [20] Stefanie Rost, Dieter Gerten, Alberte Bondeau, Wolfgang Lucht, Janine Rohwer, and Sibyll Schaphoff. Agricultural green and blue water consumption and its influence on the global water system. *Water Resources Research*, 44(9), 2008.
- [21] Sara Minoli, Jonas Jägermeyr, Senthold Asseng, Anton Urfels, and Christoph Müller. Global crop yields can be lifted by timely adaptation of growing periods to climate change. *Nature Communications*, 13(1):7079, 2022.
- [22] Markus Reichstein, Eva Falge, Dennis Baldocchi, Dario Papale, Marc Aubinet, Paul Berbigier, Christian Bernhofer, Nina Buchmann, Tagir Gilmanov, Andre Granier, et al. On the separation of net ecosystem exchange into assimilation and ecosystem respiration: review and improved algorithm. *Global change biology*, 11(9):1424–1439, 2005.

- [23] Gilberto Pastorello, Carlo Trotta, Eleonora Canfora, Housen Chu, Danielle Christianson, You-Wei Cheah, Cristina Poindexter, Jiquan Chen, Abdelrahman Elbashandy, Marty Humphrey, et al. The fluxnet2015 dataset and the oneflux processing pipeline for eddy covariance data. *Scientific data*, 7(1):225, 2020.
- [24] Ilya Loshchilov and Frank Hutter. Decoupled weight decay regularization. *arXiv preprint arXiv:1711.05101*, 2017.
- [25] Nina Buchmann, Lukas Hortnagl, Sabina Keller, and Fabio Turco. Fluxnet Product from Oensingen crop, 2003–2023. <https://hdl.handle.net/11676/IWly2Cb3xiVw8QB-Z1SXWqKx>, 2024. Accessed 2025-07-30.
- [26] Youngryel Ryu, Minseok Kang, and Jongho Kim. FLUXNET-CH4 KR-CRK Cheorwon Rice paddy, Dataset. <https://doi.org/10.18140/FLX/1669649>, 2020. Data collected from 2015–2018. Accessed 2025-07-30.
- [27] Adam Schreiner-McGraw. AmeriFlux FLUXNET-1F US-Mo3 LTAR CMRB Field 3 (CMRB BAU), Ver. 3-5, AmeriFlux AMP, Dataset. <https://doi.org/10.17190/AMF/2229384>, 2023. Accessed 2025-07-30.
- [28] Andy Suyker. AmeriFlux FLUXNET-1F US-Ne1 Mead - irrigated continuous maize site, Ver. 4-7, AmeriFlux AMP, (Dataset). <https://doi.org/10.17190/AMF/1871140>, 2025. Accessed 2025-07-30.
- [29] Giulia Ronchetti, Luigi Nisini Scacchiafichi, Lorenzo Seguini, Iacopo Cerrani, and Marijn van der Velde. Harmonized european union subnational crop statistics can reveal climate impacts and crop cultivation shifts. *Earth System Science Data*, 16(3):1623–1649, 2024.
- [30] Fluxnet Product from Lonze crop, 2004–2020. https://hdl.handle.net/11676/eo.cBxOeMONH2G8z4g0G_60J, 2021. Accessed 2025-07-30.
- [31] Fluxnet Product from Gebesee crop, 2001–2020. <https://hdl.handle.net/11676/ICpbHZew62rMezJ0DdGd1QZz>, 2021. Accessed 2025-07-30.
- [32] Fluxnet Product from Klingenberg crop, 2004–2023. <https://hdl.handle.net/11676/b8wQzTvW2nkN-mFPaSIO6lad>, 2021. Accessed 2025-07-30.
- [33] Fluxnet Product from Selhausen Juelich crop, 2011–2014. https://hdl.handle.net/11676/HE7Nj8_yV0xTr1zYLvOchSR1, 2021. Accessed 2025-07-30.
- [34] Marius Schmidt Karl Schneider. FLUXNET2015 DE-Seh Selhausen, Dataset. <https://doi.org/10.18140/FLX/1669649>, 2020. Data collected from 2015–2018. Accessed 2025-07-30.
- [35] Fluxnet Product from Voulundgaard crop, 2009–2018. <https://hdl.handle.net/11676/Msw4MfzUvAI4JRy4PEXnxRdg>, 2024. Accessed 2025-07-30.

- [36] Pauline Buysse, Brigitte Durand, Jean-Christophe Gueudet, Nicolas Mascher, Eric Larmanou, Pierre Cellier, and Benjamin Loubet. FLUXNET2015 FR-Gri Grignon, Dataset. <https://doi.org/10.18140/FLX/1669649>, 2020. Data collected from 2004-2014. Accessed 2025-07-30.
- [37] Fluxnet Product from Aurade crop, 2005-2023. <https://hdl.handle.net/11676/8VEnzKK7Clppzc7jrXIMFAIc>, 2021. Accessed 2025-07-30.
- [38] Fluxnet Product from Estrees-Mons A28 crop, 2017-2023. https://hdl.handle.net/11676/iFrHZC8K_-lgFIKzoAQOXoc9, 2021. Accessed 2025-07-30.
- [39] Fluxnet Product from Lamasquere crop, 2005-2020. <https://hdl.handle.net/11676/7WGNecqpODsIXmZfRvQxboSm>, 2021. Accessed 2025-07-30.
- [40] Simone Sabbatini, Nicola Arriga, Beniamino Gioli, Dario Papale, Michele Tomasucci, and Alessio Boschi. FLUXNET2015 IT-CA2 Castel d’Asso2, Dataset. <https://doi.org/10.18140/FLX/1440231>, 2020. Data collected from 2011–2014. Accessed 2025-07-30.
- [41] Jillian M Deines, Sotirios V Archontoulis, Isaiah Huber, and David B Lobell. Observational evidence for groundwater influence on crop yields in the united states. *Proceedings of the National Academy of Sciences*, 121(36):e2400085121, 2024.
- [42] Camilo Rey-Sanchez, Carlos Tianxin Wang, Daphne Szutu, Kyle Hemes, Joseph Verfaillie, and Dennis Baldocchi. AmeriFlux FLUXNET-1F US-Bi2 Bouldin Island corn, Ver. 3-5, AmeriFlux AMP, (Dataset). <https://doi.org/10.17190/AMF/1871135>, 2022. Accessed 2025-07-30.
- [43] Adam Schreiner-McGraw. AmeriFlux FLUXNET-1F US-Mo1 LTAR CMRB Field 1 (CMRB ASP), Ver. 5-7, AmeriFlux AMP, (Dataset). <https://doi.org/10.17190/AMF/2229382>, 2025. Accessed 2025-07-30.
- [44] Adam Schreiner-McGraw. AmeriFlux FLUXNET-1F US-Mo3 LTAR CMRB Field 3 (CMRB BAU), Ver. 3-5, AmeriFlux AMP, (Dataset). <https://doi.org/10.17190/AMF/2229384>, 2023. Accessed 2025-07-30.
- [45] Andy Suyker. AmeriFlux FLUXNET-1F US-Ne2 Mead - irrigated maize-soybean rotation site, Ver. 3-7, AmeriFlux AMP, (Dataset). <https://doi.org/10.17190/AMF/2574638>, 2025. Accessed 2025-07-30.
- [46] Andy Suyker. AmeriFlux BASE US-Ne3 Mead - rainfed maize-soybean rotation site, Ver. 19-5, AmeriFlux AMP, (Dataset). <https://doi.org/10.17190/AMF/1246086>, 2025. Accessed 2025-07-30.
- [47] John Baker and Tim Griffis. AmeriFlux FLUXNET-1F US-Ro1 Rosemount- G21, Ver. 5-7, AmeriFlux AMP, (Dataset). <https://doi.org/10.17190/AMF/1881588>,

2025. Accessed 2025-07-30.
- [48] John Baker and Tim Griffis. AmeriFlux FLUXNET-1F US-Ro3 Rosemount- G19, Ver. 4-7, AmeriFlux AMP, (Dataset). <https://doi.org/10.17190/AMF/2469468>, 2025. Accessed 2025-07-30.
- [49] John Baker and Tim Griffis. AmeriFlux FLUXNET-1F US-Ro5 Rosemount I18_South, Ver. 5-7, AmeriFlux AMP, (Dataset). <https://doi.org/10.17190/AMF/1818371>, 2025. Accessed 2025-07-30.
- [50] John Baker and Tim Griffis. AmeriFlux FLUXNET-1F US-Ro6 Rosemount I18_North, Ver. 5-7, AmeriFlux AMP, (Dataset). <https://doi.org/10.17190/AMF/1881590>, 2025. Accessed 2025-07-30.
- [51] Sergio M Vicente-Serrano, Santiago Beguería, and Juan I López-Moreno. A multiscalar drought index sensitive to global warming: the standardized precipitation evapotranspiration index. *Journal of climate*, 23(7):1696–1718, 2010.